

Summer 2019

3D Topology Optimization of Spatially Reinforced Composites

Luis G. Bahamonde Jácome

Follow this and additional works at: <https://scholarcommons.sc.edu/etd>



Part of the [Mechanical Engineering Commons](#)

Recommended Citation

Bahamonde Jácome, L. G.(2019). *3D Topology Optimization of Spatially Reinforced Composites*. (Doctoral dissertation). Retrieved from <https://scholarcommons.sc.edu/etd/5457>

This Open Access Dissertation is brought to you by Scholar Commons. It has been accepted for inclusion in Theses and Dissertations by an authorized administrator of Scholar Commons. For more information, please contact dillarda@mailbox.sc.edu.

3D TOPOLOGY OPTIMIZATION OF SPATIALLY REINFORCED COMPOSITES

by

Luis G. Bahamonde Jácome

Bachelor of Science
Universidad Politécnica de Madrid, 2015

Master of Science
Universidad Politécnica de Madrid, 2015

Submitted in Partial Fulfillment of the Requirements

for the Degree of Doctor of Philosophy in

Mechanical Engineering

College of Engineering and Computing

University of South Carolina

2019

Accepted by:

Zafer Gürdal, Major Professor

Ramy Harik, Major Professor

David Rocheleau, Committee Member

Steven Wanthal, Committee Member

Cheryl L. Addy, Vice Provost and Dean of the Graduate School

© Copyright by Luis G. Bahamonde Jácome, 2019
All Rights Reserved.

ACKNOWLEDGMENTS

As I write these acknowledgements, I cannot help but feel humbled by all the people I owe thanks to. It takes a village to raise a child, and the brainchild that is this work was certainly raised by many thoughtful and kind people.

This work would not have been possible without the financial support of The Boeing Company since most of it was performed under contract SSOW-BRT-W0915-0002 through the University of South Carolina. Beyond financial support, the insightful technical discussions with Dr. Agnes Blohm-Schrieber, Dr. Mostafa Rassaian and Dr. Steven Wanthal from The Boeing Company are gratefully acknowledged.

I would also like to show my appreciation to my advisors, Prof. Zafer Gürdal and Ramy Harik. It is only after collecting my thoughts in this thesis, that I see all the patience Prof. Gürdal had to muster when hearing my presumptuous claims on how optimal design works. (Any such claims that have stubbornly persisted into this manuscript are my fault alone.) It humbles me to realize all the effort that is required to wise up a person into understanding the many nuances of engineering optimization, yet I have been fortunate enough to cross paths with someone as learned in them as Prof. Gürdal. Complementing this education, Prof. Harik always opened my eyes into how research and scholarship works. I have walked into quite a few classrooms and offices, but none had a door as widely open upon which I left with my eyes opened just as much as Prof. Harik's. To the extent that despite my shortcomings as an instructor of Castellano, Prof. Harik was still able to fluently communicate this know-how to me in my own mother tongue. The help of Dr. Steven Wanthal and Prof. David Rocheleau as committee members is also gratefully acknowledged.

A special shout-out to all the people at the McNair Center for Aerospace Innovation and Research (McNAIR) is in order. Although everyone I met there made a contribution to this work and thus should consider themselves included in this shout-out, I feel compelled to single out two people in particular. I want to thank Dr. Brian Tatting for expanding my mind to think like a shell. And then further stretching it to think in a powerful object-oriented manner. I humbly thank Dr. Tatting for these and other learning-how-to-learn skills. I would also like to thank Prof. Michel van Tooren for the many insightful discussions on a (777X wingspan-like) wide range of technical subjects. If Prof. Harik opened my eyes and Dr. Tatting expanded my mind, then Prof. van Tooren honed my smell of BS. Particularly, the BS of my own assumptions. At the least, it is a very humbling experience.

I would also like to dedicate some words to the many graduate students that worked with Prof. Gürdal before me. When I started this work and Prof. Gürdal would explain to me the way of thinking about optimal design of composite structures, he would always point out the decades of hard work that took to arrive to such understanding. Most of the ideas that underpin this understanding are counter-intuitive or, even worse, simple enough to hide in plain sight. Yet they have been systematically discovered by these students. Standing on their shoulders further humbles me.

I am also very grateful of the family I have. It is humbling to reflect on the endless source of motivation that is required to finish a PhD. Yet my mother, father and sister always made sure I had plenty of it to keep walking strong. It is to my little sister, María José, that I dedicate this work.

Finally, I want to thank you, the reader. Since it is very likely that you are a technical reader well instructed in the art of skimming through texts, I appreciate you going out of your way to read these acknowledgements. These praises only find voice when you take the time to read them. And knowing that you have, humbles me the most.

ABSTRACT

Topology optimization is a numerical design tool used to generate structural concepts that present optimal load paths for a given set of functional requirements. This functional generative design capability has been used to lightweight high performance structures with 1D, 2D and 3D stress states. On the other hand, fiber-reinforced composites are the perfect candidate material to use in high performance structures due to the tailorability of their stiffness and strength properties. Although numerical tools that simultaneously tailor the composite material properties while optimizing the structural topology exist, these tools are inherently limited to 1D and 2D stress states.

This work aims to address this limitation by presenting a new topology optimization framework for 3D design of fiber-reinforced composites. Such computational design framework is composed of three key elements: (i) a macromechanical model, called multi-thread theory, that estimates the stiffness properties of 3D fiber reinforced composites; (ii) a stable coupling algorithm between macro-mechanics and structural analysis codes; and (iii) a scalable optimization algorithm.

To evaluate the feasibility of this framework, 2D and 3D topology optimization results are presented. The 2D numerical results are used to investigate the benefits of the new continuation scheme formulated within the optimization algorithm. Moreover, by optimizing 3D topologies with geometric conditions such that the stress state is approximately plane stress, the 2D results are used to show consistency between this computational design framework and other 2D approaches based on classical laminate theory. Finally, to demonstrate the capability of this framework a 3D MBB-beam is simultaneously optimized for both topology and fiber reinforcement orientation. This

problem optimized 249,452 design variables to yield an optimized MBB 3D-beam that is 75% lighter, yet only 16.5% more flexible. Such step-change improvement in performance was due to the complex geometry of the optimized MBB 3D-beam (and its aligned reinforcement) involving structural elements such as curvilinear arches, variable-thickness sidewalls and uni-axial struts connecting these walls.

TABLE OF CONTENTS

ACKNOWLEDGMENTS	iii
ABSTRACT	v
LIST OF TABLES	x
LIST OF FIGURES	xi
CHAPTER 1 INTRODUCTION	1
1.1 Motivation	1
1.2 Dissertation outline	3
CHAPTER 2 COMPUTATIONAL DESIGN OF FIBER-REINFORCED COMPOSITES	6
2.1 Structural and multidisciplinary optimization	6
2.2 Topology optimization	13
2.3 Variable stiffness design	20
2.4 Topology optimization of composites	23
CHAPTER 3 A 3D FRAMEWORK FOR DESIGN OF FIBER-REINFORCED COMPOSITES	25
3.1 Multi-thread theory	26
3.2 Variable stiffness analysis coupling	34
3.3 Optimal design problem	40

3.4	Numerical solution algorithm	43
3.5	Test plan	47
CHAPTER 4 SPECIFICATIONS FOR A TOPOLOGY OPTIMIZATION TOOLKIT . . .		49
4.1	MARIA composites	50
4.2	MARIA analysis	53
4.3	MARIA design	58
CHAPTER 5 2D TOPOLOGY OPTIMIZATION OF FIBER-REINFORCED COMPOSITES		61
5.1	MBB 2D problem	62
5.2	Isotropic MBB	63
5.3	Transversely isotropic MBB	67
5.4	Curvilinear fiber format MBB	70
5.5	Post-processing of 2D node-centered topologies	73
CHAPTER 6 3D TOPOLOGY OPTIMIZATION OF FIBER-REINFORCED COMPOSITES		76
6.1	MBB 3D problem	76
6.2	Isotropic MBB	80
6.3	Orthotropic MBB	83
6.4	Curvilinear fiber format MBB	85
CHAPTER 7 CONCLUDING REMARKS		91
7.1	Significant contributions	91
7.2	Compromises and limitations	93

7.3 Recommendations	95
BIBLIOGRAPHY	97
APPENDIX A MATERIAL PROPERTIES	105
APPENDIX B NON-DIMENSIONAL TRANSVERSELY ISOTROPIC STIFFNESSES	107
APPENDIX C LAGRANGE MULTIPLIER COMPUTATION	109
APPENDIX D IN-PLANE INVARIANT MATRICES	111

LIST OF TABLES

Table 3.1	Thread model assumptions, idealizations, and deviations from idealization.	28
Table 3.2	Plan of numerical experiments to study the proposed 3D framework. . . .	48
Table 5.1	Optimized MBB topologies for varying mesh sizes obtained by linear interpolation, reciprocal interpolation and continuation scheme techniques for an isotropic material	64
Table 5.2	Optimized MBB topologies for varying fiber orientation angles obtained by unpenalized linear interpolation, reciprocal interpolation and continuation scheme techniques for a transversely isotropic material .	68
Table 5.3	Performance metrics of the curvilinear fiber format MBB, straight fiber format 0° and a 0° ground structure	73
Table 6.1	Volume fraction, η , evolution to understand convergence into a boxed beam in $\eta = 0.5$	82
Table 6.2	material stiffness and optimized compliance for different degrees of orthotropy due to a layer-by-layer manufacturing process	84
Table 6.3	Side and top views of the optimal topology wireframes showing different internal cavities for different degrees of orthotropy	85
Table 6.4	Side and top views of the optimal topology wireframes showing different internal cavities for different degrees of orthotropy	87
Table A.1	Material properties using engineering constants	106

LIST OF FIGURES

Figure 2.1	Elements of an optimization model	9
Figure 2.2	Nested analysis and design	12
Figure 2.3	Simultaneous analysis and design	13
Figure 2.4	Optimal truss layout using Sokol's algorithm for Michell type structures	14
Figure 3.1	ϕ and ψ rotation angles from XYZ global axes to 123 material axes of a perpendicular reinforced thread plane	29
Figure 3.2	Geometry and loading of a cantilever beam	32
Figure 3.3	Non-dimensional bending stiffness as a function of the number of elements along the height for a quasi-isotropic material using single thread and thread plane models	34
Figure 3.4	Dependency tree of a node-centered spatially varying material with constant anisotropy as it is approximated to an element-centered discretization	38
Figure 3.5	2D cantilever obtained from an element-centered topology optimization without filters to show checkerboarding instabilities.	39
Figure 3.6	XDSM diagram of the numerical solution algorithm	47
Figure 4.1	Class hierarchy of a <code>DesignCycle</code>	60
Figure 5.1	Symmetric part of a 2D MBB meshed with rectangular S4 finite elements	62
Figure 5.2	XDSM diagram of solution algorithm used for the MBB 2D problem . .	63
Figure 5.3	Normalized compliance for varying mesh sizes obtained by linear interpolation, reciprocal interpolation and continuation scheme techniques for an isotropic material	65

Figure 5.4	Number of iterations required to optimize MBB topologies for varying mesh sizes obtained by linear interpolation, reciprocal interpolation and continuation scheme techniques for an isotropic material	67
Figure 5.5	Normalized compliance for varying fiber orientation angles obtained by unpenalized linear interpolation, reciprocal interpolation and continuation scheme techniques for a transversely isotropic material. These compliance curves are bounded by a ground structure compliance curve, and twice the ground structure compliance	69
Figure 5.6	Number of iterations required to optimize MBB topologies for varying fiber orientation angles obtained by unpenalized linear interpolation, reciprocal interpolation and continuation scheme techniques for a transversely isotropic material	71
Figure 5.7	Criss-cross topology pattern shown by an optimized MBB topology obtained with the reciprocal interpolation technique, 300-by-100 mesh, $\beta = 0.25$, $\zeta = 10^9$ for a 90 degree transversely isotropic material	71
Figure 5.8	Fiber orientation distribution plot of the curvilinear fiber format MBB	72
Figure 5.9	Convergence history of the curvilinear fiber format MBB	73
Figure 5.10	Node-centered 2D topology with jagged edges.	74
Figure 5.11	Smooth boundary obtained from a node-centered 2D topology with jagged edges.	74
Figure 5.12	3D printed beam from an STL file generated by processing a smooth boundary image.	75
Figure 6.1	Global coordinate system for the MBB 3D ground structure	79
Figure 6.2	XDSM diagram of solution algorithm used for the MBB 3D problem	80
Figure 6.3	Isoview of a $t = 0.033$ thin MBB made with isotropic material.	81
Figure 6.4	Sideview of a $t = 0.033$ thin MBB made with isotropic material.	81

Figure 6.5	Extended optimality curve for a thick $t = 1$ MBB as a function of volume fraction. Contour plots of the σ_{33} component are shown on top of the deformed mesh for select points	83
Figure 6.6	Global coordinate system for the MBB 3D-beam ground structure	84
Figure 6.7	Isoview of a $t = 0.033$ thin MBB with curvilinear fiber reinforcement. . .	86
Figure 6.8	Sideview of a $t = 0.033$ thin MBB with curvilinear fiber reinforcement shown as an element-centered fiber orientation angle distribution	86
Figure 6.9	Isoview of a curvilinear fiber format thick MBB 3D-beam for $\eta = 0.25$. .	88
Figure 6.10	Isoview of a curvilinear fiber format thick MBB 3D wireframe, for $\eta = 0.25$, and fiber orientation segment distribution.	88
Figure 6.11	Sideview of a curvilinear fiber format thick MBB 3D wireframe, for $\eta = 0.25$, and fiber orientation segment distribution.	89
Figure 6.12	Rearview of a curvilinear fiber format thick MBB 3D wireframe, for $\eta = 0.25$, and fiber orientation segment distribution.	89
Figure 7.1	MBB 2D-beam boundary with 0 degree fiber path and watertight boundary finish	94

CHAPTER 1

INTRODUCTION

3D topology optimization of spatially reinforced composites is a niche engineering application. As such, its value depends on the context of the design and manufacturing processes where it will be applied. This chapter provides such a context. First, Sec. 1.1 motivates the need for this work by briefly describing the challenges of using topology optimization for additive manufacturing of composites. Then the principal elements of this work are outlined in Sec. 1.2.

1.1 MOTIVATION

Topology optimization is a numerical design tool used to generate structural concepts that present optimal load paths for a given set of functional requirements. This functional generative design capability has been used to lightweight high performance structures with 1D, 2D and 3D stress states. On the other hand, fiber-reinforced composites are the perfect candidate material to use in high performance structures due to the tailorability of their stiffness and strength properties. Although numerical tools that simultaneously tailor the composite material properties while optimizing the structural topology exist, these tools are inherently limited to 1D and 2D stress states.

Similarly, early 3D printing hardware implementations, although called 3D printers, were almost entirely based on 2D X-Y plotter type contraptions. Hence, the use of 2D topology optimization techniques were easily extended to design "3D printed" parts. As confidence in design and manufacturing of these quasi-3D printed parts increased, so did the complexity of the part geometry and dimensionality. This led to the development of 3D

topology optimization techniques. For metallic parts, use of 3D topology optimization yields end-use structural parts that meet the functional requirements. For nonmetallic materials, use of 3D printed plastics is not structurally capable enough to be end-use parts and has been limited to rapid prototyping applications. Hence the need for carbon fiber reinforced plastics, and particularly 3D topology optimization of spatially fiber reinforced composites.

However, addressing this need is not without challenges. One challenge in applying topology optimization techniques for design of 3D printed parts is to quantify the stiffness and strength improvements that stem from the use of carbon fibers in 3D parts. Fiber-reinforced composite materials are heterogeneous bi-phasic materials composed of a reinforcement phase embedded in a continuous phase. The fiber provides high-performance load-carrying properties. Reason for which this phase is called the reinforcement. The reason for using fibers, as substantiated by Jones (1975), is because in a fiber the crystals are aligned along the fiber axis and thus fewer internal defects, like dislocations, appear. Thus, a fiber has better mechanical properties than the material in bulk form. These fibers are embedded in a continuous phase whose purpose is to hold the fibers together. This phase is called the matrix, and it acts as a binder. The matrix distributes the loads as tension to the fibers and homogenizes deformations, however it has low-performance load-carrying properties. This requires 3D behavior models of both the composite material and the part.

Besides the challenge of developing behavior models, the anisotropy inherent in fiber-reinforced composite materials and the anisotropy that emerges from the build direction need to be designed for as well. From a design optimization perspective, the simultaneous design of shape and reinforcement orientation poses a challenge of computational tractability. Topology optimization itself is a large-scale problem with thousands of design variables. Adding just as many variables to design the reinforcement orientation further exacerbates the curse of dimensionality.

Computational tractability is a critical barrier to the adoption of 3D topology optimization for carbon-fiber additive manufacturing. Another, is the limitations of the manufacturing hardware itself. These limitations must either be accounted for in the design or removed by new additive manufacturing hardware. This work does not include limitations of state-of-the-art manufacturing hardware. Rather, this work aims to develop a scalable approach to rapid optimal design of 3D structures with both topology and reinforcement orientation as variables under design.

1.2 DISSERTATION OUTLINE

This work is organized as a linear research story. Chapter 2 presents a review of computational design processes reported in the literature. Unlike computer-aided design, the role the computer plays in these reviewed processes involves some degree of decision making. In particular, this survey focuses on using optimization algorithms to drive certain steps of the design process. The body of knowledge that uses optimization algorithms in structural design processes is called structural and multidisciplinary optimization. This body of knowledge is reviewed in Sec. 2.1 to situate topology optimization among other structural optimization techniques and also for engineering diagrams that allow to communicate an algorithm effectively and succinctly. Such as the extended design structure matrix. Although Chapter 2 is focused towards design optimization processes of fiber-reinforced composites, see Sec. 2.3 and Sec. 2.4, topology optimization techniques are reviewed regardless of the material's degree of anisotropy, see Sec. 2.2.

After the topology optimization and composites design literature review of Chapter 2, a new computational design framework is reported in Chapter 3. The novelty of this framework is in designing, with a 3D stress state in 3D Euclidian space, both the shape and fiber orientation angles. The formulation of the three key elements of the framework are presented therein. Sec. 3.1 formulates a macromechanical theory of the 3D stress-state behavior of fiber-reinforced composites. The macromechanical theory

serves to model the stiffness properties of a given fiber-matrix architecture. However, to achieve a curvilinear fiber format this fiber-matrix architecture must vary spatially from point to point. The coupling between this spatial variation of the stiffness properties and a finite element analysis code constitutes the second key element of the framework and is reported in Sec. 3.2. The last key element of the framework is its optimization algorithm which is presented as a design problem formulation and its associated solution algorithm. Sec. 3.3 formulates the design problem and Sec. 3.4 presents the solution algorithm. This framework will be later used for numerical studies discussed in Chapters 5 and 6. However, the test plan of all these studies is summarized in Sec. 3.5.

To carry out the numerical test plan of Sec. 3.5, the computational framework is implemented into a computer program. This computer program is not an application for solving optimal design problems. Rather it is an optimization toolkit used for developing application-specific optimization scripts. The specifications of this topology optimization toolkit are presented in Chapter 4. A design application can be described as having three modeling domains: (i) composites, (ii) structural analysis, (iii) optimal design. A library for each of these domains is presented in Sec. 4.1, Sec. 4.2 and Sec. 4.3 respectively.

The implementation is then used to solve the MBB beam application. This application is of interest because its a benchmark in the topology optimization literature and also because it can be validated with three point bending tests. Chapter 5 discusses the results of solving the MBB beam problem for 2D stress states and Chapter 6 does the same for an MBB 3D-beam problem. Both chapters present solutions ranging from isotropic material to a curvilinear fiber format.

Finally, the significant contributions, compromises and limitation, and recommendations for future research are summarized in Chapter 7. The contributions are presented based on their significance to two audiences. Sec. 7.1.1 presents the contributions to the structural and multidisciplinary optimization research area. While Sec. 7.1.2 presents the contributions of this work to the overall goal of the McNair Center

for Aerospace Innovation and Research (McNAIR).

CHAPTER 2

COMPUTATIONAL DESIGN OF FIBER-REINFORCED COMPOSITES

2.1 STRUCTURAL AND MULTIDISCIPLINARY OPTIMIZATION

The field of structural optimization studies (i) the mathematical formulation of structural design problems and (ii) aims to solve these formulated problems by applying appropriate numerical search techniques. Most practical design problems are ill-defined decision-making problems that aim to minimize the cost of engineering an (elastic) system from a set of functional requirements. Consequently, formulating in mathematical terms all of these design alternatives requires a quantification of the cost of each alternative and of the degree of compliance with the functional requirements. Quantifying the requirement compliance allows to systematically assess the feasibility of a design option and discard unfeasible design alternatives. Whereas quantifying the cost allows to decide between competing feasible designs. However, these two quantification steps are not straightforward. Cost quantification requires comprehensive cost models of the whole life-cycle of the product. Life-cycle cost modeling is an across-the-board multidisciplinary effort. That is why proxies such as weight are used in structural optimization. The expectation is that if the proxy metric is minimized, the cost will also be minimized to a certain extent. Note that this assumption assumes all the other cost factors remain the same. For example, a part geometry with purposeful complexity will reduce weight and consequently the direct operating cost, yet the development cost will increase. Besides structural economy, the structure must perform its function of carrying loads with

constraints on the deformation and damage behavior. The US aeronautical authorities via the Federal Aviation Regulations state in FAR 25.305 that

the structure must be able to support limit loads without detrimental permanent deformation. With regards to failure, the structure must be able to support ultimate loads without failure for at least 3 seconds.

The analysis of the ability of a structure to integrally perform its function without excessive deformation or damage is called an analysis of structural integrity or structural analysis, for short.

To describe all the possible design alternatives in terms of computable structural models, these mathematical models must be expressed in terms of parameters that modify the size, shape, or connectivity of the elastic members that make up the structure. The model parameters that change the structure from one design alternative to another are called design variables. The quantified cost and functional requirements which are a function of the design variables are defined in terms of a scalar objective function which will be minimized and a set of constraints that must be satisfied. Together, design variables, objective function, and constraints make up the elements of the problem formulation.

Structural optimization problems are normally classified in terms of the geometric parameterization strategy. Assuming the structure is discretized using the finite element method the following problem classes are defined:

- Sizing optimization problems where the material properties and mesh are fixed (i.e, the position of the nodes is fixed). The only geometric parameters under design are cross-section properties such as areas of 1D bodies or thicknesses of 2D bodies
- Shape optimization problems where the position of the nodes is variable (although these need not represent design variables) and thus the shape of the boundary of the structure is under design control. Shape optimization approaches change the

boundary shape based on boundary variation methods and are thus limited to curves of a given parametric family

- Topology optimization problems where although the position of the nodes is fixed, their presence is not. The on or off state of each node is encoded by high and low binary values of the material properties

Note that each class of problem does not focus on a different geometrical aspect. In fact each problem is more general than the previous. For instance, a shape optimization problem will also change the size of the structure.

Solution of the problem formulation using numerical search techniques requires an organized execution procedure of different computational elements. For instance, solving systems of differential equations, function approximations, and design update rules are computational elements that make up any solution algorithm. A visual illustration that efficiently communicates the solution algorithm is the so-called extended design structure matrix (XDSM), proposed by Lambe and Martins (2012). The syntax of XDSM diagrams is introduced in Sec. 2.1.1.

Finally, the fundamental concepts pertaining to the solution algorithm as introduced above and shown in Fig. 2.1 are of general application to any optimal design problem. Consequently, the numerical search technique can also be a general numerical optimization technique like those presented in the nonlinear programming literature (Nocedal and Wright 2006). Typically such approaches formulate the structural optimization problem in terms of a standard problem formulation to interface with general-purpose optimization codes. In addition, the field of structural optimization also has domain-specific solution algorithms. For instance, fully stressed design is a heuristic criteria that defines an optimal structure as the structure where all its members are stressed to the maximum material allowable.

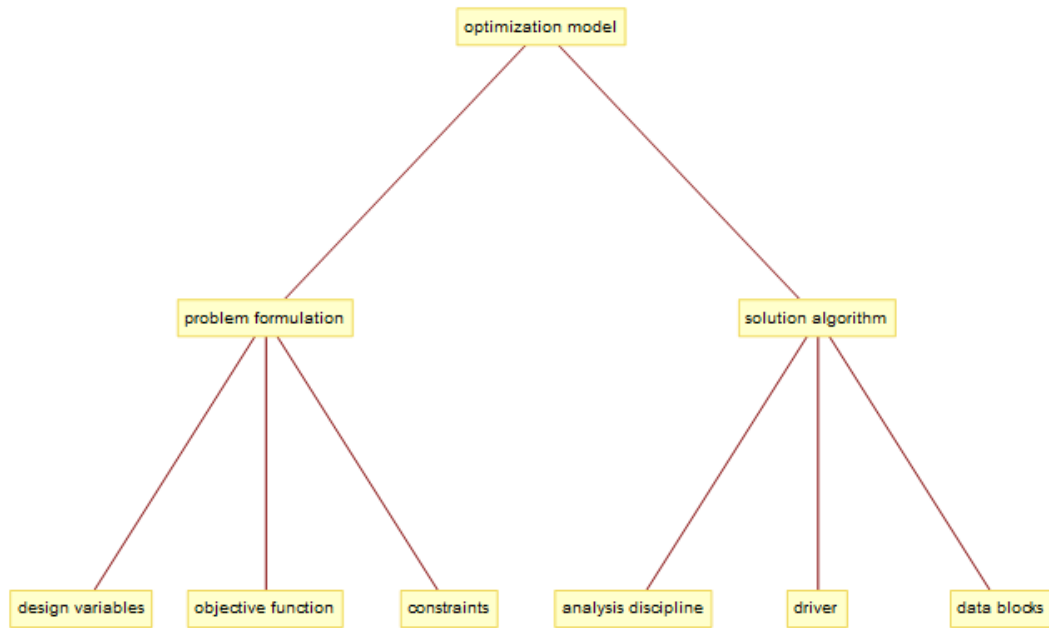


Figure 2.1: Elements of an optimization model

2.1.1 EXTENDED DESIGN STRUCTURE MATRIX

This section provides textual explanation for the diagram used in this work to visualize numerical algorithms. This graphical representation is called an Extended Design Structure Matrix (XDSM) and was developed by Lambe and Martins (2012). The aim of XDSM is to provide sufficient details of the problem formulation and solution algorithm in a single diagram.

The design optimization process used in this work can be described as a sequence of three steps. First, an initialization step that models the ground structure and external loading, material properties definition, and the design parameterization of the composite anisotropy and structural geometry. Second, an iterative step consisting of an optimization loop that updates the design variables based on simulations of predictive models. While the first step is comprised of non-recurrent computations, the second step has recurrent computational expenses. Finally, the third step interprets the optimal design. Interpretation

efforts range from performance comparison with the initial design, to interpretation of the boundaries of the structural topology. The interpretation step is also a non-recurrent cost of the process. This procedural paradigm is captured by the problem formulation and solution algorithm specifications. The problem formulation specifies the data dependency via the use of mathematical functional dependencies and the solution algorithm specifies the process flow of the sequential execution of each computational element. Both define the recurring or non-recurring costs of each design optimization step. For instance, the symbolic computation of a closed-form solution of the structural behavior results in a more expensive non-recurring initialization step than using a numerical update scheme during each iteration step, which results in a non-recurring cost.

The combination of the problem formulation and solution algorithm is called the architecture of the design optimization process. Specifying the architecture into computer codes is called an implementation. And making the implementation reach a runnable state on a given computing hardware is called a realization. This development model of the design optimization process is akin to the engineering of software systems presented by Brooks (1975). Note that there is not a one-to-one correspondence between architecture and implementation. Many implementations can implement a given architecture with, for example, different communication strategies. For instance, the communication between the composites code and the structural analysis code can use file input-output (I/O) or a direct memory access. The former requires more time to read and write files whereas the latter does not.

An XDSM diagram represents computational elements with boxes, I/O data with parallelepipeds, data dependency with thick grey connection lines, and process flow with thin black lines. If the computational element is a master process then the component is illustrated with a rounded rectangle, whereas if the computational element is a slave process the component is illustrated with a straight rectangle. With similar intent, if the I/O data is persisted (i.e., written to disk) the parallelepiped is white, while a greyed parallelepiped

represents volatile I/O data.

The action of drawing an XDSM diagram starts with laying out the computational elements along the diagonal of a matrix. The first computational element starts in the second diagonal position. Then the data dependency lines are drawn to connect any source computational element to a target computational element. The I/O data parallelepiped of the internal data passed from the source to the target is situated in the same row as the source and the same column of the target. If the source precedes the target then the relationship is a feed-forward and the I/O data is situated in the matrix upper triangle. A feed-back relationship where the target precedes the source situates the I/O data in the matrix lower triangle. The external I/O data is located in the first row and column of the matrix. The first row shows user-specified input data that is needed by the same-column computational element. And the first column shows the persisted results of the design optimization and is situated in the same row as the computational element that calculates such output. For example, Fig. 2.2 shows an XDSM diagram with an optimizer, solver, structural model, and objective function and constraint as computational elements. The optimizer feeds the design vector x to the structural model, yet passes control to the solver. The solver feeds a guess of the displacement field u to the structural model which, in conjunction with the x data, computes the residual error of this guess's compliance of the governing equations and feeds it back to the solver. Once this iteration loop is converged, the solver feeds the converged displacement to the objective function and constraint. The objective function and constraint are evaluated for u and x , and these metrics are feed back to the optimizer to update the design vector x . Once the optimization has converged, the persisted results are the optimal design x^* and its structural behavior u^* .

The problem formulation for Fig. 2.2 can be written as

$$\underset{x}{\text{minimize}} \quad f(x, u(x)) \quad (2.1)$$

where $u(x)$ is implicitly computed by the structural analysis inner loop. This is called

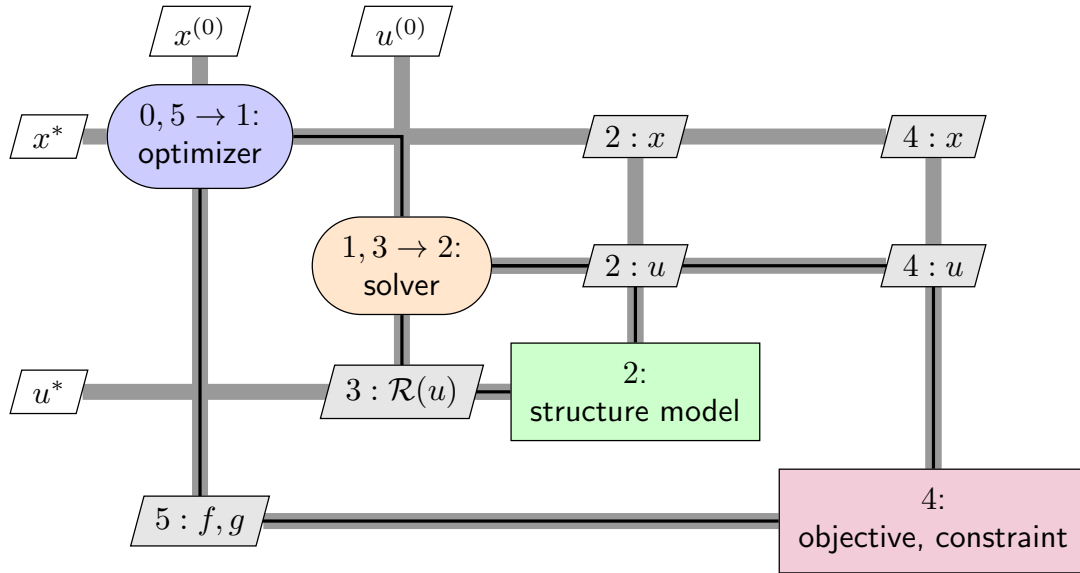


Figure 2.2: Nested analysis and design

a nested analysis and design (NAND) architecture. A major architectural decision for simulation-driven design optimization processes is the question of using a NAND architecture or allow the analysis converge concurrently with the optimization iterations. The later case is called a simultaneous analysis and design (SAND) architecture and has the following problem formulation

$$\begin{aligned} & \underset{x, u}{\text{minimize}} && f(x, u) \\ & \text{subject to} && \mathcal{R}(u) = 0 \end{aligned} \quad (2.2)$$

where now the structural analysis is formulated as an equality constraint. Note that in a NAND architecture the displacements are also treated as design variables under the control of the optimizer. Fig. 2.3 illustrates a NAND architecture.

The SAND architecture is the least computationally expensive of the two, because the heavy analysis is no longer a recurrent cost. However, unless the SAND design optimization process fully converges the intermediate designs are physically meaningless. For the NAND architecture, if the optimization process is cut short one may still obtain

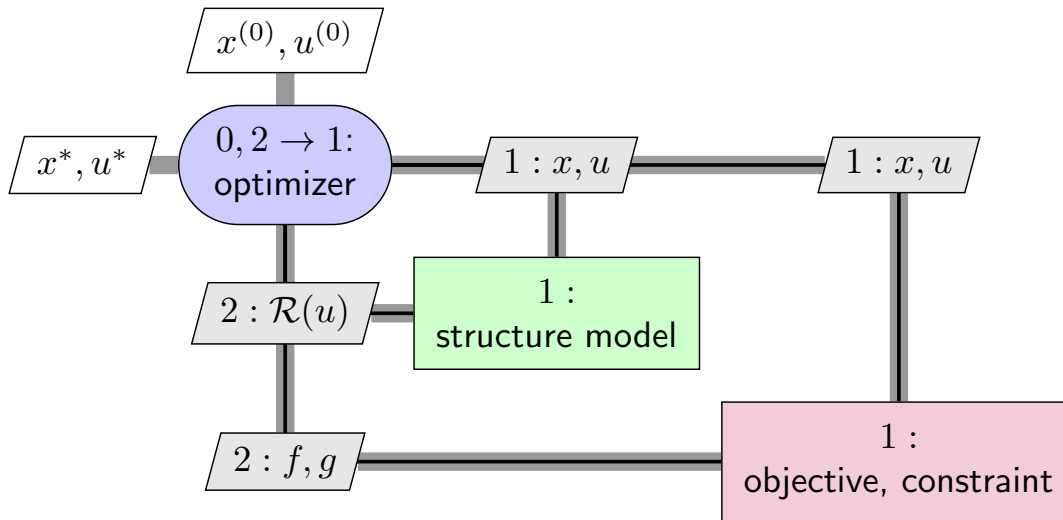


Figure 2.3: Simultaneous analysis and design

optimized (although suboptimal) results. Moreover, a NAND architecture requires access to the mathematical system of the model. Most commercial analysis codes are black-box codes and hence do not provide access to such an interface.

2.2 TOPOLOGY OPTIMIZATION

The origins of topology optimization can be traced back to the weight minimization problem of frames, as studied by Michell (1904). The study of the optimal layout of discrete 1D structures were among the first problems to be studied in this field. The reason lies in the fact that for 1D structures the cross-section area serves as a continuous variable that when it reaches zero (or any small numeric threshold) it can be interpreted as the suppression of that bar. Thus, fully stressed design approaches which size the cross-section area based on the ratio of the internal stress and the material allowable are applicable to do topology optimization of 1D structures. Moreover, such optimization problem can be formulated as a linear programming problem which scales up to handle many bars very efficiently. The maturity of these algorithms is revealed by Sokół (2011) in a paper that presents the implementation of the algorithm in less than 100 lines of code and designs

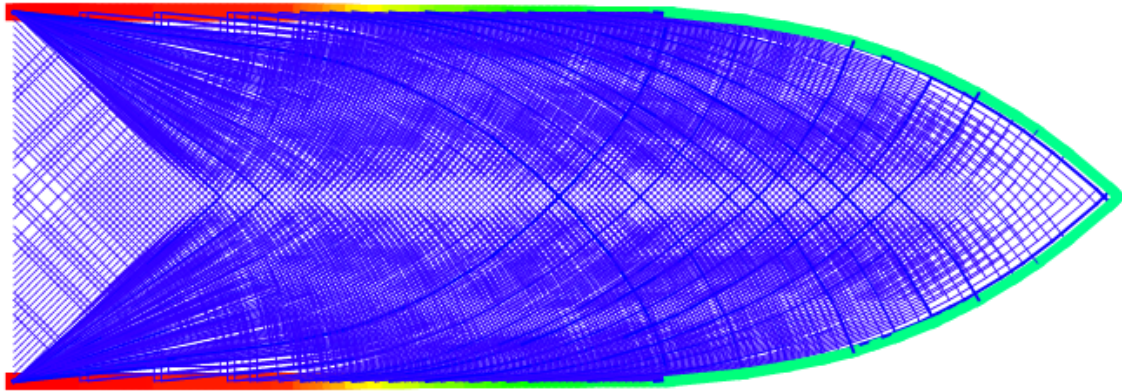


Figure 2.4: Optimal truss layout using Sokol's algorithm for Michell type structures

thousands of bars in a manner of minutes (using a typical personal computer). Fig. 2.4 shows the optimal topology generated by Sokol's algorithm for a cantilever truss under a tip load.

The following challenge on the topology optimization of 2D structures can be solved by density-based methods and was introduced by Bendsøe and Kikuchi (1988). This density based method pre-multiplies the stiffness tensor by a penalized density field. The density field is discretized at the elements of the finite element (FE) mesh. Thus, any implementation of this topology optimization algorithm necessitates an FE analysis code that allows the specification of variable stiffness properties. The reason for choosing an element-wise discretization as given by Bendsøe and Sigmund (2011) is due to the minimum implementation effort that is needed, since most FE analysis codes assume an elementwise constant stiffness material.

Contrary to 1D structures, 2D continuum structures designed with the density-based method of Bendsøe and Kikuchi (1988) showed numerical instabilities. One of them was the presence of checkerboard regions. Checkerboards are defined, by Sigmund and Petersson (1998), as regions with alternating void and solid elements ordered in a checkerboard like fashion. Figure shows these checkerboard regions for a 2D MBB beam problem. Far from representing optimal microstructures, checkerboards appear due to the poor modeling of the stiffness of a checkerboard by low-order finite elements. The FE

method admits stiffness discontinuities. Thus, a checkerboard-like structure is perfectly admissible for analysis. Moreover, a super-element constituted by a checkerboard region has a stiffness similar to a grayscale, with the same volume as a grayscale yet it is not a grayscale (which is penalized by the method). This weakness is exploited by the optimization algorithm to yield spurious solutions. As explained by Jog and Haber (1996) and Díaz and Sigmund (1995), the stiffness of a checkerboard is zero due to the stress singularities at the corners of the solid regions. Several checkerboard prevention schemes have been presented in the literature, to evolve the element-centered algorithm. Díaz and Sigmund (1995) and Jog and Haber (1996) suggest the use of higher-order elements. However, this approach substantially increases computational time and is less likely to be scalable to more design variables. Alternatively, Bendsøe et al. (1993) propose dividing the domain into patches of elements. However, the checkerboards are not entirely removed. Some checkerboards are observed between patches because two neighboring patches do not overlap and thus these checkerboards patches are not detected by the prevention scheme. By far, the most popular checkerboard prevention scheme are filters based on a neighborhood size. These filters average the density (or its sensitivity) of the current element with that of the adjacent neighborhood. This converts checkerboard regions into elements with grayscales which are inherently penalized by the density-based method. Sigmund (1994) presents a filter based on sensitivities, and Bourdin (2001) presents a generalization of the filtering approaches to topology optimization.

Yet another way to prevent checkerboards is by discretizing the density field at the nodes. Rahmatalla and Swan (2004) propose a node-centered approach for topology optimization, and show checkerboard-free topologies. However the topologies shown for the MBB problem only match the benchmark when using perimeter constraints. Otherwise, topologies with islands of points appear. Yi et al. (2014) also propose a node-centered approach where the elementwise densities are approximated using a Shepard interpolation function with a diameter playing the same role of the above mentioned filters.

Another issue of density-based methods is mesh-dependency where the topology is qualitatively different for different mesh sizes. Solving this issue involves a separation of concerns where the density discretization is not driven by the analysis accuracy. For a generic anisotropic material whose microstructure is contained in a reference volume of length-scale l_3 , the FE mesh intended for analysis must have elements of size l_a such that

$$l_a \ll l_3, \quad (2.3)$$

where a larger separation yields more computationally efficient analyses. Note that l_3 serves to quantify the size of a *point* in the continuum structure. On the other side the FE mesh must be small enough with respect to a typical dimension of size L

$$l_a \ll L \quad (2.4)$$

so as to have an accurate approximation. With respect to the density discretization in terms of a mesh with elements of size l_d , the resolution of the design must be large enough to reduce the curse of dimensionality, so

$$l_d \ll l_3. \quad (2.5)$$

Note that density-based methods are inherently large-scale problems. The computational cost increases with the number of design variables, which inherently are many if an accurate boundary description is needed.

Mesh dependency becomes an issue when the FE mesh intended for analysis is shared by the density discretization,

$$l_d = l_a. \quad (2.6)$$

In such cases, some structural members will have a length-scale l_d dictated by the need of having an accurate analysis. Even when the design intent is otherwise. Moreover,

experience with the FE method shows that modeling structural members with few finite elements affects the accuracy of the deformation analysis of the structural member,

$$l_d \ll l_a. \quad (2.7)$$

Currently, density-based methods separate these concerns by using fixed-neighborhood filters. The same filters proposed by Sigmund (1994) to eliminate checkerboards serve to address mesh dependency. The filter radius is fixed and serves as the length-scale parameter. Thus, not only does the filter average densities (or its sensitivities) of the adjacent neighborhood to eliminate alternative solid and void elements, but it is expanded to other neighboring elements to provide features of larger scale. The separation of concerns is achieved by allowing the stress analyst size the FE mesh, and leaving the filter radius parameter to be a decision of the designer. Other length-scale control approaches are surveyed by Sigmund and Petersson (1998) yet are seldom found in the topology optimization literature. A reason for the popularity of filter-based element-centered density-methods might be due to their ease of implementation. Andreassen et al. (2011) demonstrate how easily such algorithm can be implemented in less than 100 lines of code. This implementation solves a 2D MBB problem which can help to explain why the MBB problem has also achieved the status of a benchmark problem.

However, a fixed-neighborhood filter does not fully separate concerns. Although the structural features no longer depend on the FE mesh, the number of design variables is still dictated by the number of elements (or nodes). A potential solution to this problem is by a dual-mesh approach similar to the patching technique proposed by Bendsøe et al. (1993) for checkerboard prevention. By having design superelements and analysis elements the member length-scale is dictated by the design mesh and the accuracy of the analysis is dictated by the analysis mesh. Moreover, the number of design variables is dictated by the design mesh which is already coarser than the analysis mesh. No reference to this dual-mesh approach has been found in the literature. This dual-mesh approach still needs

to provide a sufficiently cheap and accurate mechanism to transfer information from one mesh to the other, to be useful for topology optimization.

Besides checkerboarding and mesh-dependency, the issue of the optimal penalization parameter has been a concern raised in the literature. The optimal topologies furnished by the density-based method are different depending on the value of the penalization parameter. To eliminate this algorithmic dependency and obtain a global optima, Allaire and Francfort (1993) and Allaire and Kohn (1993) suggested the use of a continuation scheme. A continuation scheme is a heuristic that has been used in the topology optimization literature to deal with the non-convexity that arises with a density penalization. According to Sigmund and Petersson (1998), a continuation scheme gradually changes the optimization problem from an artificial convex problem to the original non-convex design problem in a number of steps. Each step gradually increases the penalization value. The use of a continuation scheme in topology optimization can be traced as far back as 1993, where Allaire and Kohn (1993) presented a relaxed formulation for topology optimization of composite materials. Composites were defined as a microscopically perforated isotropic material where the density is the volume fraction. Thus providing a physical interpretation to gray scales. Using such composite materials was called a relaxed formulation. Allaire and Kohn (1993) argued that because a relaxed formulation poses the topology optimization problem as a quasi-convex problem, as opposed to a penalized one which is non-convex, the starting point for the penalized problem must be the solution of the relaxed formulation. Moreover, Allaire and Kohn (1993) showed for three numerical examples that the sub-sequent penalized solution had little effect on the compliance when compared to the unpenalized solution from the first step, yet significantly reduced the use of composites. Ever since, several authors (Buhl et al. 2000; Petersson and Sigmund 1998; Watada et al. 2011) have provided further empirical evidence of the global convergence benefits a continuation scheme may provide. Others, such as Stolpe and Svanberg (2001) have shown that

these schemes are not of general-purpose applicability and may fail for certain problems. Moreover, research on reducing the computational cost of continuation schemes, their major drawback, has also been undertaken. Similar to Allaire and Kohn (1993), Peeters et al. (2015) optimize the topology without a density penalization. Then as a second step, minimize the grayscales with an objective that explicitly measures the amount of gray area. Unlike Allaire and Kohn (1993), the penalized problem includes a bound on the compliance to specify the tolerated trade-off between performance and gray scale. The optimization steps have also been reduced to a single optimization problem. Rojas-Labanda and Stolpe (2015) formulate the penalization parameter as a design variable that changes within the optimization and report this automatic penalty continuation to show favorable speedups when compared with classical continuation schemes. However, as shown by this brief overview, the application of continuation schemes has been limited to the penalization parameter and in some cases, as reported by Rojas-Labanda and Stolpe (2015), to the stopping condition tolerance. By using non-linear interpolation functions for densities that are centered at the nodes, the sources of non-convexity multiply. Hence, if a continuation scheme is to be used, a more holistic scheme is required. The intent of this work is to change not only the penalization, but also the interpolation function used in each step. Thus gradually trading, in each step, the convexity benefits for speed of convergence. To this end, the scope of this work is narrowed to a minimum compliance problem formulation based on optimality criteria, with a solution algorithm incapable of length-scale control. Hence providing different topologies with finer meshes. Introducing a filter for the sake of mesh independence endows additional numerical properties, to the solution algorithm, foreign to the merits of the interpolation functions.

The element-centered density-based method presented so far is concerned with the minimum compliance problem. Essentially, it finds the structure with the maximum stiffness that has a fraction of the initial volume. However, with the use of a general purpose mathematical programming algorithm such formulation has expanded to strength-based

designs and to include other physical problems, like thermal design. Bendsøe and Sigmund (2011) present a review of these applications and use the method of moving asymptotes (MMA), proposed by Svanberg (1987), as the general purpose optimizer.

Both compliance-based heuristics and MMA-driven algorithms have been applied by several authors to 3D topology optimization. A very interesting result of the 3D topology optimization research is found in Sigmund et al. (2016). Such paper shows that the optimal 3D topologies are not Michell-like structures, as seen in 2D. Rather when the volume fraction target is not low enough variable-thickness shells are far more stiff than their Michell-like counterparts. It seems a rather fitting ending to finalize this section with the non-optimality of Michell structures for 3D problems. However, not without a reference to Sigmund and Maute (2013) which constitutes the latest literature survey of topology optimization.

2.3 VARIABLE STIFFNESS DESIGN

The variable stiffness concept was formally introduced by Gürdal and Olmedo (1993). Their work presented an analysis of panels with variable stiffness properties due to an in-plane curvilinear fiber format. The elastic behavior of these variable stiffness panels resulted in non-uniform stress distributions even under a uniformly applied load. Moreover, these panels generated shear stresses even when no material shear-extension coupling was present. This prompted the notion of using the variable-stiffness panel analysis code with the intent of designing the local fiber orientation for a tailored stress distribution. A tailored stress distribution affects the load-carrying efficiency of a structure. However, the effect a stiffness variation has on the elastic response of the panel can be seldomly described with closed-form solutions and requires the assistance of numerical codes.

As recounted by Tatting (1998), the analysis of structures with spatially-varying stiffness properties dates back to variable thickness solutions of shell theory in 1918. Moreover, the use of a curvilinear fiber format for the design of laminated plates was

already presented as early as 1991 by Hyer and Charette (1991). Nevertheless, the notion of using smooth and continuous variations of the stiffness properties for analysis and design was first communicated by Gürdal and Olmedo (1993). Initially, the only mechanism for producing variable stiffness panels considered was that of a curvilinear fiber format. The reason was that fiber placement technology had the potential of implementing such fiber paths by steering the fibers or fiber steering. Moreover, the only considered fiber paths were a family of curves described by

$$\theta(x, y) = \frac{2}{a}(T_1 - T_0)x + T_0, \quad (2.8)$$

where θ is the fiber orientation angle at the point (x, y) , a is the side of the panel under the compressive load, T_0 is the fiber orientation angle at the panel center where $x = 0$, and T_1 is the fiber orientation angle at the panel ends where $x = \pm a/2$. The works of Tattng (1998), Blom et al. (2009), Blom et al. (2010), and Gomes et al. (2014) use this linear variation of the fiber orientation angle. These authors claim this parameterization to provide manufacturable fiber paths.

With the aim of expanding the design space to other curvilinear fiber formats, a discretization of the fiber orientation angle is needed. However this approach is inherently large-scale, because it has as many design variables as discrete points used to mesh the panel times the number of plies. Setoodeh et al. (2005) and Hammer et al. (1997) suggest the use of lamination parameters to minimize the number of design variables of the variable stiffness minimum-compliance problem. Moreover since lamination parameters are aggregates of the stacking sequence direction cosines and the thickness at each point, the design space is expanded to include variable thickness designs. Thus, a lamination parameter approach allows to design the laminate in two steps. First, the stiffness properties variations are designed via the use of lamination parameters. Then, the stacking sequence at each point is obtained by minimizing the residual between the obtained stiffness properties and the optimal stiffness properties. The design of composite laminates for required

stiffness properties is presented by Miki and Sugiyamat (1993), using a graphical approach. The use of numerical optimization procedures to solve this second step is presented in Setoodeh et al. (2006).

The solution of the variable stiffness design problem was extended from minimum compliance to fundamental frequency optimization by Abdalla et al. (2007) by using a generalized reciprocal approximation. A reciprocal approximation is an approximation concept that replaces the objective function by the Taylor expansion of the reciprocal of the design variables. This approximate problem is a convex optimization problem and is used to update the design variables to a new design point, where the reciprocal approximation is used again. The generalized reciprocal approximation, as proposed by Abdalla et al. (2007), follows the same evolution as in topology optimization where a general purpose optimizer is used to extend the problem to handle additional performance metrics. In particular, this same approximation is used by Ijsselmuiden et al. (2008) to design variable stiffness composites with strength constraints using an omni-strain approach.

Variable stiffness composites as a technical keyword has evolved to mean any optimal composite with spatially-varying stiffness properties. Regardless of the mechanism that provides this variation. Even if as hinted in this review and surveyed by Sabido et al. (2017) the most popular mechanism is a curvilinear fiber format. However, the use in the literature of this term has been tribal. Gürdal's research group uses the term extensively, even if the majority of the research focuses on a curvilinear fiber format. Perhaps to underline all the potential mechanisms captured by the lamination parameter design approach. Although such term is used even when lamination parameters are not used. Raju et al. (2015) use continuous tow shearing to design variable stiffness composites, and call their approach variable-angle tows. Perhaps to highlight the different fabrication method. Finally, Stanford et al. (2014) and Wu et al. (2013) use the term tow steering. Perhaps with the aim of underlining the focus of their research to AFP manufactured designs. This work defines variable stiffness composites as a fibrous composite with spatially-varying stiffness

properties due to any mechanism yet with gradually-varying continuous variations. Not only is such definition aligned with the genesis of the term, but it is also anchored in the mathematical theory of partial differential equations with gradually-varying coefficients and thus provides a layer of abstraction for the development of analysis and design codes. This contrived definition is also broad enough to allow stiffness variations due to a fictitious density field. Thus, analysis codes developed for variable stiffness composites can serve both the purpose of composite tailoring and topology optimization.

2.4 TOPOLOGY OPTIMIZATION OF COMPOSITES

The problem of the combined 2D topology and fiber path optimization was posed at the beginning of this millenia and is found in the work of Setoodeh et al. (2005) and Peeters et al. (2015). The work of Setoodeh et al. (2005) solves a minimum compliance problem for the design of the topology and fiber orientation of a composite sheet. It follows from the work of Abdalla and Gürdal (2002) which use a node-centered density-based approach to design the density and fiber orientation angle fields. Calculus of variations is used in such formulation to formulate the compliance-based problem as many local design problems. Moreover, they use cellular automata as the analysis framework instead of an FE analysis. Peeters et al. (2015) advanced this approach by using lamination parameters to optimize the laminate, and a two-step optimization approach to optimize the topology. The two-step topology optimization algorithm first solves the un-penalized variable thickness sheet problem and in a second step a measure of the grayscale area is used as the objective function to be minimized while targeting the previous optimal compliance. This second topology optimization problem is solved using reciprocal approximations of the gray area. Note the same intent of capturing a global optima by solving the variable thickness sheet problem. This is similar to the continuation method presented in Sec. 3.4.

Both of these node-centered approaches update the design by first updating the composite design variables and then updating the density. The work of Setoodeh et

al. (2005) uses design rules while the work of Peeters et al. (2015) solves reciprocal approximation problems at every design update. However, while Setoodeh et al. (2005) approximate the density from the nodes to the Gauss point by averaging the reciprocal of the penalized density, Peeters et al. (2015) use a reciprocal average of the in-plane stiffness matrix.

Although not entirely focused on fibrous composites, the approach of Bendsøe et al. (1993) deserves to be mentioned. Bendsøe et al. (1993) suggest a free parameterization of the stiffness tensor. With a similar philosophy to that of lamination parameters, by designing the stiffnesses themselves in a first step, a truly 3D optimal structure is achieved. Designing the material, be it a fibrous composite or other, is relegated to a second step. Such an approach is called free material optimization(FMO). A review of FMO is presented by Kočvara et al. (2008).

As a concluding remark, note the conceptual integrity and similarities of both topology optimization and variable stiffness composites research fields. Both approaches use the same distributed approach to optimizing their respective design fields. Both approaches use convexifying approximations to solve the large-scale optimization problems. This is no coincidence. The authors of one field are the same as in the other. The 1991 proceedings of the NATO Advanced Study Institute on Optimization of Large Structural Systems (Rozvany 1991) founded these research fields into a common international society of structural and multidisciplinary optimization. Whose attendees (Haftka, Gürdal, Bendsøe, and Sigmund among others) are the usual suspects of these fields of research.

CHAPTER 3

A 3D FRAMEWORK FOR DESIGN OF FIBER-REINFORCED COMPOSITES

Because the current frameworks for the analysis and design of composite laminates are inherently limited to plane-stress laminated shells that approximately deform according to the Kirchoff-Love hypothesis, the design of structures in 3D space requires a new framework. Like the 2D frameworks of last section, any candidate 3D framework must stand on at least 3 legs: (i) a macro-mechanical theory about the composite material behavior, (ii) a stable coupling between macro-mechanics and structural analysis codes, and (iii) a scalable optimization algorithm.

This chapter presents such a 3D design framework. Section 3.1 presents multi-thread theory as an approach to modeling the macro-mechanics of spatially reinforced composites. Next in Section 3.2, the variable stiffness concept serves to couple a spatially-varying node-centered description of the stiffness properties with a displacement-based finite element formulation. The last component of the framework, a scalable optimization algorithm, spans both Section 3.3 and Section 3.4. The former formulates the optimal stiffness design problem, while the latter proposes a potentially scalable algorithm to numerically solve the previous problem statement. Finally, Section 3.5 outlines the numerical test plan that will be used to study this 3D design framework in chapters 5 and 6.

3.1 MULTI-THREAD THEORY

The fiber-matrix architecture of a spatially reinforced composite is, in general, a collection of 3D curvilinear fiber paths embedded in a continuous matrix. If the reference volume element (RVE) is chosen to be small enough, the fiber-matrix architecture can be modeled by a very large, yet finite, distributed set of volumetric elements containing a uni-directional filament of pre-impregnated fibers aligned into a generic 3D orientation. For the purposes of multi-thread theory, an RVE with only uni-directional fibers is called a single thread. However as the RVE becomes larger, more and larger segments of fiber paths will be included in it. Although the curvature of these fiber path segments will be non-zero, as a first-order approximation, multi-thread theory assumes this larger RVE to be composed of multiple threads where each thread, α , has its own 3D orientation given by the unit vector u_m^α .

The purpose of multi-thread theory is to approximate the local macro-mechanical behavior of a spatially reinforced composite in terms of transversely isotropic threads, C_{ijkl}^α , as

$$\langle C_{ijkl} \rangle = \langle C_{ijkl} \rangle \left(C_{ijkl}^1(u_m^1), \dots, C_{ijkl}^\alpha(u_m^\alpha), \dots, C_{ijkl}^N(u_m^N) \right), \quad (3.1)$$

where $\langle C_{ijkl} \rangle$ is the stiffness tensor of a homogenous anisotropic material that is equivalent to the spatially reinforced composite under study. Moreover, as a first-order approximation, the relation between $\langle C_{ijkl} \rangle$ and C_{ijkl}^α will be linearized.

The effective stiffnesses, $\langle C_{ijkl} \rangle$, can be expressed as a linear combination of thread stiffnesses, C_{ijkl}^α , if one assumes an iso-strain deformation of each thread and their assembly. This derivation starts at the stress volume-average equation

$$\langle \sigma_{ij} \rangle = \frac{1}{V} \int \sigma_{ij} dV = \frac{1}{V} \sum_{\alpha=1}^N C_{ijkl}^\alpha \epsilon_{kl}^\alpha, \quad (3.2)$$

where V is the volume of the RVE and it is assumed that each thread presents a

linear homogeneous elastic behavior. Since the homogenized composite also follows the generalized Hooke's law and under the iso-strain assumption presents the same strain for each thread, α , the effective stiffness yields a thread volume-average

$$\langle C_{ijkl} \rangle = \sum_{\alpha=1}^N \frac{V^{\alpha}}{V} C_{ijkl}^{\alpha} \quad (3.3)$$

where N is the total number of threads in that RVE, and V^{α} is called the thread volume and serves as a weight of the linear combination. The ratio of the thread volume, V^{α} , relative to V is called a thread volume fraction, is denoted by:

$$\mu^{\alpha} = \frac{V^{\alpha}}{V}, \quad (3.4)$$

and serves as a normalized weight of the linear combination. Hence, the effective stiffness is written as

$$\langle C_{ijkl} \rangle = \sum_{\alpha=1}^N \mu^{\alpha} C_{ijkl}^{\alpha} \quad (3.5)$$

Although Eq. (3.5) appears to be a linear relation between C_{ijkl}^{α} and $\langle C_{ijkl} \rangle$, there still remains an implicit dependence between C_{ijkl}^{α} and μ^{α} through the fiber volume fraction of each thread. A change in the fiber volume fraction,

$$v_f^{\alpha} = \frac{V_f^{\alpha}}{V_m^{\alpha}} \quad (3.6)$$

impacts the thread stiffness, C_{ijkl}^{α} , through the engineering constants. While the same change in v_f^{α} may also affect μ^{α} through V^{α} , given by

$$V^{\alpha} = V_f^{\alpha} + V_m^{\alpha} \quad (3.7)$$

A further assumption is needed to formulate the problem in terms of an independent μ^{α} . Under the assumption that each thread matrix volume is proportional to the fiber volume of that same thread,

Table 3.1: Thread model assumptions, idealizations, and deviations from idealization.

Assumption	Idealization	Reality
iso-strain	uniform deformation	nonlinear deformation
transversely isotropic threads	ideal fiber packing	process dependent
homogenous threads	homogenized behavior	captured thru testing
$V_m^\alpha/V_f^\alpha = k$	linear matrix distribution	nonlinear at high V_f

$$V_m^\alpha = kV_f^\alpha, \quad (3.8)$$

the fiber volume fraction of each thread can be proven to be constant for all threads, and equal to the RVE's fiber volume fraction. The physical interpretation of this proportionality assumption is based on the fact that the function of a matrix material is to hold fibers in a given orientation. When more fibers are aligned in a particular orientation, the matrix will have to support more load to keep them in place than if it would have less embedded fibers. A numerical study that corroborates this assumption can be found in Kregers and Melbardis (1978).

In summary, multi-thready theory formulates the macro-mechanical behavior of a spatially reinforced composite as an independently-weighted linear combination of transversely isotropic threads. In turn, each C_{ijkl}^α is a function of 5 independent engineering constants and a unit direction vector u_m^α . The formulation of the stiffnesses as function of engineering constants for different types of material symmetry can be found in Nemeth (2011). A tabulated summary of multi-thread theory assumptions is given in Table 3.1. Next, the parameterization of the direction vector u_m^α in terms of a smaller set of orientation angles for different degrees of anisotropy will be formulated based on Eq. (3.5).

The direction vector u_m^α of a single thread can be parameterized with the two angles θ and ϕ of its spherical coordinates. Where θ is the in-plane rotation angle, similar to

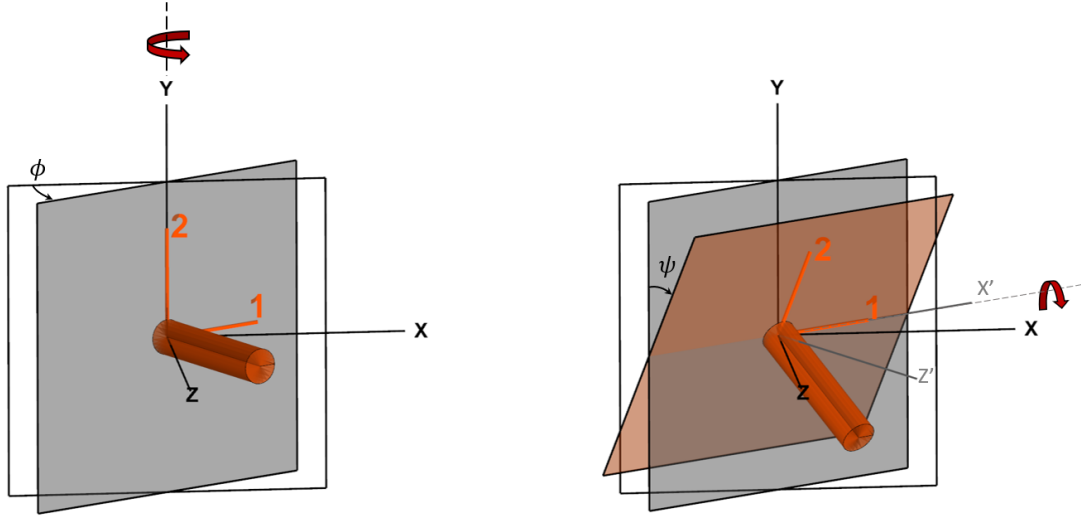


Figure 3.1: ϕ and ψ rotation angles from XYZ global axes to 123 material axes of a perpendicular reinforced thread plane

the one used in classical lamination theory (CLT), while ϕ is the out-of-plane rotation angle. Using a pair of angles for each single thread results in $2N$ orientations. However, depending on the degree of anisotropy of the multi-thread configuration, a smaller set of orientation angles can be defined. For example, when the orientations of multiple threads are coplanar, a so-called thread plane can be defined in terms of the plane orientation and in-plane rotations. Figure 3.1 illustrates a generic thread plane orientation obtained by a sequence of rotations defined by the 321 Tait-Bryan convention. Note that the first rotation around the material principal axis 3 does not change the thread plane orientation, rather it changes the degree of planar orthotropy. While the subsequent rotations ϕ around the Y axis and ψ around the X' axis define the 3D orientation of the thread plane.

The in-plane rotations, θ^α , of the coplanar threads can be aggregated into a smaller set of in-plane stiffness parameters that control the degree of anisotropy of the thread plane. In matrix form, multi-thready theory approximates an XY plane of coplanar threads as

$$[< C >] = \sum_{\alpha=1}^N \mu^\alpha [Q_\theta] [C^\alpha] [Q_\theta]^T \quad (3.9)$$

where $[Q_\theta]$ is the in-plane transformation matrix. After some algebraic manipulation,

the right hand side of Eq. (3.9) can be written as

$$[\langle C \rangle] = \sum_{\alpha=1}^N \mu^{\alpha} \left([\Gamma_0] + [\Gamma_1] \cos 2\theta^{\alpha} + [\Gamma_2] \sin 2\theta^{\alpha} + [\Gamma_3] \cos 4\theta^{\alpha} + [\Gamma_4] \sin 4\theta^{\alpha} \right), \quad (3.10)$$

where $[\Gamma_p]$ with $p = 0, \dots, 4$, are material invariant matrices given in appendix D.

Adding a generic 3D orientation of the thread plane yields

$$[\langle C \rangle] = [Q(\phi, \psi)] \left([\Gamma_0] + \sum_{p=1}^4 v_p [\Gamma_p] \right) [Q(\phi, \psi)]^T, \quad (3.11)$$

where the v_p parameters follow the same trigonometric structure of the so-called lamination parameters IJsselmuiden (2011)

$$\mathbf{v} = \left(\sum_{\alpha=1}^M \mu^{\alpha} \cos 2\theta^{\alpha}, \sum_{\alpha=1}^M \mu^{\alpha} \sin 2\theta^{\alpha}, \sum_{\alpha=1}^M \mu^{\alpha} \cos 4\theta^{\alpha}, \sum_{\alpha=1}^M \mu^{\alpha} \sin 4\theta^{\alpha} \right), \quad (3.12)$$

If these in-plane stiffness parameters, v_p , are formulated as independent design variables then a feasible region, as defined by Hammer et al. (1997):

$$2v_1^2(1 - v_3) + 2v_2^2(1 + 2v_2) + v_3^2 + v_4^2 - 4v_1v_2v_4 \leq 1, \quad (3.13)$$

$$v_1^2 + v_2^2 \leq 1, \quad (3.14)$$

$$-1 \leq v_p \leq 1, \quad (3.15)$$

is required to constrain the optimization.

The thread plane finds application in describing the inherent anisotropy of deposition manufacturing techniques that build parts on a layer-by-layer basis. In deposition manufacturing, the deposited layers may be considered isotropic yet the inter-layer binding provides very little stiffness. Although many degrees of anisotropy can be modeled with

multi-thread theory, this work will only consider the multi-thread configurations of a single thread and a thread plane. Both of these configurations can be unified into a perpendicular reinforced thread plane given by

$$[\langle C \rangle] = [Q(\phi, \psi)] \left((1 - \mu^\perp) \left([\Gamma_0] + \sum_p v_p [\Gamma_p] \right) + \mu^\perp [C^\perp] \right) [Q(\phi, \psi)]^T, \quad (3.16)$$

where μ^\perp is the volume fraction of the perpendicular thread with respect to all the coplanar threads, and $[C^\perp]$ is the stiffness matrix of a transversely isotropic material with the 3 material axis as the symmetry axis. Note that if $\mu^\perp = 1$ then Eq. (3.16) yields a single thread oriented along the normal to the plane. On the other hand, if $\mu^\perp = 0$ Eq. (3.16) reduces to Eq. (3.11).

To verify multi-thread theory, both single thread and thread plane models will be compared against CLT for a cantilever beam under plane bending. The cantilever beam, as shown in Figure 3.2, has a rectangular cross-section of width, b , and height, h , and is uniformly loaded on the mid-plane of the free end. The beam model uses 3D continuum brick elements C3D8R, while the load intake is modeled by applying a concentrated force, P , at the centroidal node and distributed along the rest of the mid-plane nodes with rigid body constraints.

The beam length-over-width, a/b is fixed to

$$\frac{a}{b} = 10, \quad (3.17)$$

$$b = 4, \quad (3.18)$$

while the beam slenderness, a/h , is parametrically varied from 10 until 200 with 21 values. Thus, starting with a thick beam and continuing into a thin plate where a plane-stress assumption is accurate. Such parametric sweep involves re-meshing the rectangular beam in a way that top and bottom layers of C3D8R cubes are removed on every step.

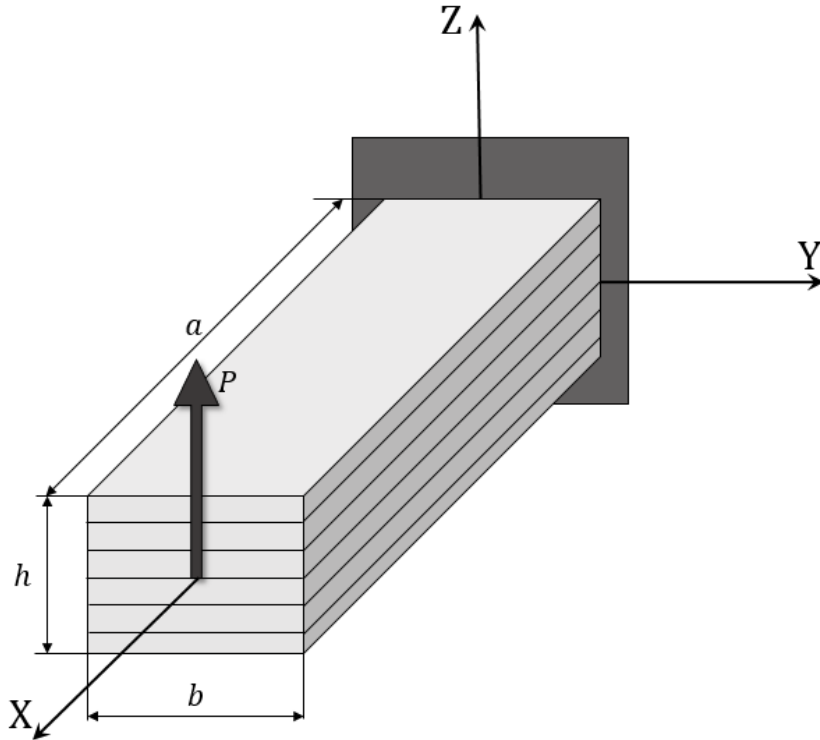


Figure 3.2: Geometry and loading of a cantilever beam

The laminate under study is a quasi-isotropic laminate stacked in the Z direction. Using Figure 3.2 as a reference, the XY plane represents the plane of isotropy. The single thread model accomplishes this laminate by using a $[\pm 60^\circ/0^\circ]_s$ stacking sequence through the height, starting from the top face. Each layer of cubic elements along the height is assigned a single thread with an XY in-plane rotation angle. Note that only height values where the cubic elements add to a multiple of 6 are possible for the single thread. On the other hand, the thread plane model approximates a quasi-isotropic laminate with

$$v_p = 0 \quad p = 1, 2, 3, 4. \quad (3.19)$$

And assigns these stiffness properties to all the cubic elements, regardless of the number of cubic elements along the height.

Figure 3.3 quantifies the variation of a normalized bending stiffness, P/Δ , given by

$$\frac{\hat{P}}{\Delta} = \frac{4}{E_x b (h/a)^3} \frac{P}{\Delta}, \quad (3.20)$$

with respect to the slenderness a/h . The normalized bending stiffness compares a measure of 3D bending stiffness against a CLT-based bending stiffness. 3D bending stiffness is measured as the numerical ratio of P/Δ , where Δ is the displacement of the node where the concentrated force P is applied. While the CLT bending stiffness is approximated using the Euler-Bernoulli bending equation for a cantilever beam

$$\frac{P}{\Delta} = \frac{3E_x I}{a^3}, \quad (3.21)$$

where the second moment of area I for a rectangular cross-section is

$$I = \frac{bh^3}{12}, \quad (3.22)$$

and the Young modulus is given by the effective Young modulus along the beam length of a quasi-isotropic CLT laminate

$$E_x = \frac{1}{h} A_{11} \left[1 - \left(\frac{A_{12}}{A_{11}} \right)^2 \right], \quad (3.23)$$

where A_{ij} are the components of the extensional stiffness matrix. The material properties used in this verification exercise correspond to material NUND2 and can be found in appendix A.

By using the normalized bending stiffness of Eq. (3.20), the cubic variation with respect to the height is blocked and only deviations due to a non-planar stress state appear. In Fig. 3.3, both the single thread and thread plane show trends of converging to the CLT solution when the number of cubes along the height reduces. Moreover, for very few elements along the height numerical inaccuracies appear due to the low order of the C3D8R finite element. On the other end, both multi-thread models converge to the same value as the number of elements increase. Thus, showing the smearing effect that appears for a large number of single thread layers.

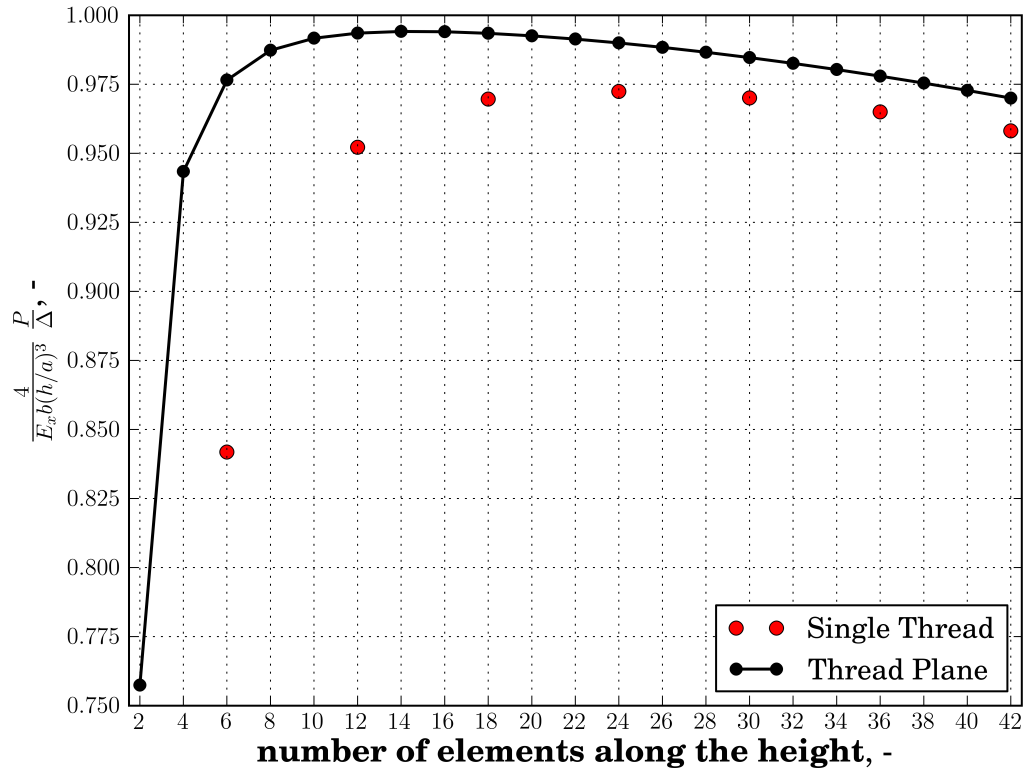


Figure 3.3: Non-dimensional bending stiffness as a function of the number of elements along the height for a quasi-isotropic material using single thread and thread plane models

The degree of anisotropy of a generally oriented single thread or thread plane constitutes one of several experimental factors considered in the test plan of Section 3.5. Among other experimental design factors, the spatial variation of the orientation of a given degree of anisotropy is also considered in the test plan. Thus, two points of the structural domain may have a different stiffness tensor. The approximations used to describe the spatial variation of the stiffness tensor is presented in the next section.

3.2 VARIABLE STIFFNESS ANALYSIS COUPLING

Density-based topology optimization formulates structural design as a material distribution problem. Because this fictitious density is a spatially distributed scalar field, the stiffness tensor becomes spatially distributed throughout the ground structure as well. On the

other hand, structural analysis codes that use finite element approximations, to estimate deformations, also assume mechanical quantities such as displacement, strain, stress and stiffness to be spatially distributed throughout the structural domain. These two spatial discretizations appear in any computational procedure of a finite-element-based topology optimization, where the stiffness tensor is first computed from the density field and then approximated into the spatial discretization of the structural analysis code. They also appear in finite-element-based composites optimization where the degree of anisotropy of the composite can change from point to point.

A variable stiffness analysis coupling is defined here as the numerical procedure that approximates the stiffness field from an original spatial discretization into another spatial discretization. Rather than a mapping, it is a coupling of two disciplines because the stiffness tensor itself is a coupling function between multiple length scales. Either through a parameterized constitutive law or through micro-scale finite element analyses. Consequently, the decision of whether to spatially approximate the stiffness or its parameters and how to approximate these spatial variations constitutes a corner stone of any computational design framework.

Variable stiffness analysis couplings can be measured in terms of computational effort, programming effort, scalability and numerical vulnerability. For example, the SIMP method proposed by Bendsøe and Sigmund (2011) centers the densities at each finite element of the analysis discretization. This reduces the programming effort to a minimum, since no spatial approximation of the stiffness field is needed. However, this coupling suffers from checkerboarding instabilities and has as many design variables as dictated by the analysis discretization. To address checkerboarding as well as length-scale control of the resulting topologies, Sigmund (1994) proposed the use of filters. Another example is found in Kang and Wang (2012), where the density mesh is fully decoupled from the analysis mesh. In this coupling approach, the density field is approximated from its original discretization to the analysis mesh via Sheppard interpolation functions. The claimed

benefit of using Shepperd interpolation is that the meshes no longer need to match. Of course, programming Shepperd interpolants requires more effort. These two examples highlight some of the considerations involved in a variable stiffness analysis coupling. Without being comprehensive, a list of coupling considerations can be:

1. What quantity should be spatially approximated? the design parameters or the stiffness tensor?
2. How should these quantities of interest be spatially discretized? by centering them at the elements or the nodes
3. What interpolation function should be used to spatially approximate the quantities of interest?
4. Should the parameter discretization be the same or at least match with the structural analysis discretization?

These coupling considerations require trade-offs between the different metrics outlined above. For instance, if the stiffness tensor is spatially approximated then 21 components need to be interpolated instead of a smaller set of parameters. Which requires more computational effort. On the other hand, interpolating a tensor rather than scalar parameters may provide robustness to the optimization algorithm against numerical vulnerabilities. Moreover, if the design parameters use a spatial discretization different to the analysis discretization then more programming effort is needed.

To explain the variable stiffness analysis coupling used in this work, the stiffness tensor will be formulated as the product of two separate variables

$$C_{ijkl} = E_L \hat{C}_{ijkl} \quad (3.24)$$

where E_L is a scalar quantity and \hat{C}_{ijkl} is a normalized rank-4 tensor. Appendix B achieves this separation of variables for a transversely isotropic material via

non-dimensionalization with the longitudinal Young modulus E_L . Furthermore, assuming the anisotropic material behaves according to linearized multi-thread theory, the effective stiffness can be expressed as an E_L that multiplies a \hat{C}_{ijkl} itself given by multi-thread theory

$$\langle C_{ijkl} \rangle = E_L(x) \hat{C}_{ijkl}(u_m^1, \dots, u_m^\alpha, \dots, u_m^N) \quad (3.25)$$

where E_L is parameterized with density variables, x , and \hat{C}_{ijkl} is parameterized with orientation variables, u_m^α . Thus describing the spatial variation of the stiffness tensor as a spatial variation of magnitude E_L and a spatial variation of anisotropy \hat{C}_{ijkl} .

Density-based topology optimization only varies E_L and thus interpolating E_L is equivalent to interpolating $\langle C_{ijkl} \rangle$. On the other hand, composites optimization involves the variation of \hat{C}_{ijkl} only.

This work's 3D framework assumes that all spatial quantities are based on a single finite element mesh. The only spatial approximations considered are nodal interpolation and inter-element averaging of quantities from the integration points to the nodes. Linear and reciprocal functions are considered for interpolation or averaging. The design variables can be centered at the elements or nodes. The analysis coupling algorithm can then be illustrated by using the dependency tree diagram described herein. For example, a topology optimization with a constant degree of anisotropy is shown in Figure 3.4 where a node-centered $E_L[n]$ distribution is computed from a nodal density distribution, $x[n]$, which is then interpolated using a reciprocal interpolation function into an element-centered $E_L[e]$. Finally, $E_L[e]$ is multiplied with a constant \hat{C}_{ijkl} to yield an element-centered spatially distributed $C_{ijkl}[e]$ that is amenable to structural analysis.

By centering the densities at the nodes, a numerical vulnerability when coupling with displacement-based finite element methods is closed. The finite element method represents the weak formulation of the anisotropic linear elastic equilibrium problem. The problem can be formulated in the strong form as:

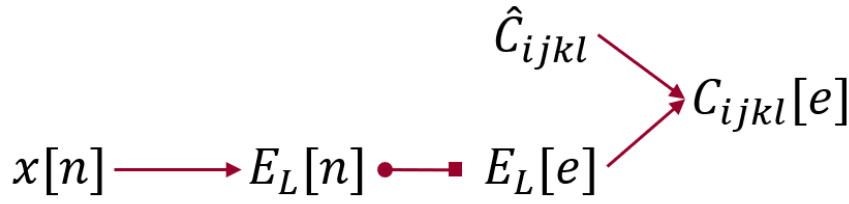


Figure 3.4: Dependency tree of a node-centered spatially varying material with constant anisotropy as it is approximated to an element-centered discretization

$$\frac{\partial}{\partial r_j} (C_{ijkl} \epsilon_{kl}) + b_i = 0. \quad (3.26)$$

This equation must be satisfied at every point of the structural domain. And can be expressed in terms of the displacement field (assuming small deformations) as,

$$\frac{1}{2} \frac{\partial}{\partial r_j} \left(C_{ijkl} \left(\frac{\partial u_k}{\partial r_l} + \frac{\partial u_l}{\partial r_k} \right) \right) + b_i = 0. \quad (3.27)$$

This partial differential equation requires a high order of continuity on the displacement and stiffness fields, $u_i(r)$ and $C_{ijkl}(r)$ respectively. Since Eq. (3.27) is valid at every point of the domain, we can multiply the left-hand side by an arbitrary non-trivial vector function and integrate over the domain,

$$\int_{\Omega} \xi_i \left[\frac{\partial}{\partial r_j} \left(C_{ijkl} \frac{\partial u_k}{\partial r_l} \right) + \frac{\partial}{\partial r_j} \left(C_{ijkl} \frac{\partial u_l}{\partial r_k} \right) + 2b_i \right] d\Omega. \quad (3.28)$$

Using Green's theorem (which is nothing more than a particular case of the Gauss-Ostrogradsky divergence theorem) we can integrate by parts this expression

$$- \int_{\Omega} \left[\frac{\partial \xi_i}{\partial r_j} C_{ijkl} \frac{\partial u_k}{\partial r_l} + \frac{\partial \xi_i}{\partial r_j} C_{ijkl} \frac{\partial u_l}{\partial r_k} + 2\xi_i b_i \right] d\Omega + \int_{\Gamma} \xi_i C_{ijkl} \left(\frac{\partial u_k}{\partial r_l} + \frac{\partial u_l}{\partial r_k} \right) n_j d\Gamma. \quad (3.29)$$

If ξ_i in Eq. (3.29) represents an arbitrary function which satisfies the kinematic compatibility equations. A so-called virtual displacement. Then Eq. (3.29) represents the internal work of a virtual displacement. The principle of virtual work requires that

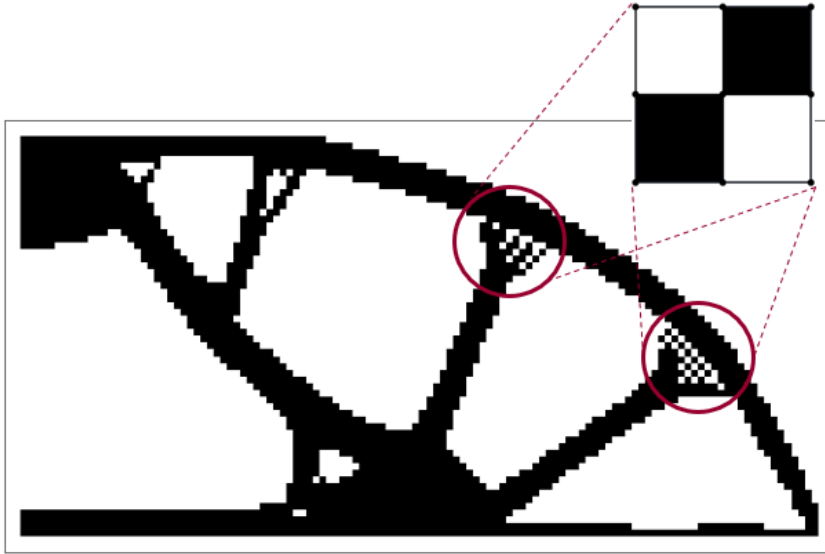


Figure 3.5: 2D cantilever obtained from an element-centered topology optimization without filters to show checkerboarding instabilities.

this internal work is the same as the external work of the same virtual displacement. The principle of virtual work is the weak form of the governing equations of linear anisotropic elasticity. A more comprehensive derivation that includes the external work of virtual displacements, is presented in Zienkiewicz and Taylor (2002). However, this brief derivation of the internal work shows the continuity requirements on the displacement and stiffness properties fields when using a displacement-based finite element method. Note that Eq. (3.29) admits a discontinuous C_{ijkl} and a u_i which show discontinuous first derivatives, because integrals are defined even for a finite set of discontinuous points of the integrand. This is in stark contrast to the strong form which requires C_{ijkl} to be C^1 , and u_i to be C^2 throughout the structural domain. Because the weak form admits discontinuous stiffness properties, if C_{ijkl} is centered at the elements (like most off-the-shelf finite element analysis codes do) then the solution is vulnerable to the phenomena of checkerboarding where structures that resemble the black cells of a checkerboard table are predicted to be stiffer than what they are in real life. This vulnerability becomes a numerical instability in element-centered density-based topology optimization as shown in Fig. 3.5.

3.3 OPTIMAL DESIGN PROBLEM

The structural design problem is simplified to minimize structural compliance subject to a volume constraint. The compliance of a structure is defined as the complementary of the work done by the external loads, W^{ext} . Equivalently, the negative of the elastic strain energy can also be minimized. The trivial solution of a holeless structure is avoided by constraining the structural volume, V , to be a fraction, η , of the initial volume, V_0 . The fictitious density, x , a spatially-varying scalar field, is the design variable of this functional optimization problem,

$$\begin{aligned} \underset{x}{\text{minimize}} \quad & -U(x) = - \int_{V_0} \rho(x) d\Omega = - \int_{V_0} C_{ijkl}(x) \epsilon_{ij} \epsilon_{kl} d\Omega, \\ \text{subject to} \quad & \frac{V(x)}{V_0} - \eta \leq 0, \\ & 0 \leq x \leq 1 \end{aligned} \quad (3.30)$$

where ϵ_{ij} , ϵ_{kl} are the equilibrium strains of linear anisotropic elasticity theory.

For a transversely isotropic material the stiffness tensor, C_{ijkl} , can be formulated as the product of the longitudinal Young modulus, E_L , and a normalized stiffness tensor, \hat{C}_{ijkl} , that remains unaltered by the density field

$$C_{ijkl} = E_L(x) \hat{C}_{ijkl}. \quad (3.31)$$

Appendix B shows such non-dimensionalization, using a transversely isotropic stiffness matrix expressed in terms of the engineering constants. The material interpolation technique presented by Andreassen et al. (2011), is used to parameterize E_L

$$E_L(x) = E_{L,\min} + x^p (E_{L,\text{nom}} - E_{L,\min}), \quad (3.32)$$

where p is a penalization on the density to force black and white topologies, $E_{L,\text{nom}}$ is the nominal longitudinal Young modulus of the material that makes up the structure,

and $E_{L,\min}$ is a lower limit on the modulus to avoid an ill-conditioned stiffness matrix for excedently small density values.

Eq. (3.30) is a constrained formulation of the minimum compliance problem. Since the volume constraint cannot be solved explicitly, the method of Lagrange multipliers is used. Which results in the unconstrained minimization of the Lagrangian functional, \mathcal{L} , given by

$$\mathcal{L} = \int_{V_0} \left[-\rho(x) + \mu(x - \eta) + \mu^+(x - 1) - \mu^- x \right] d\Omega, \quad (3.33)$$

where μ , μ^+ , and μ^- are the Lagrange multipliers of the constraints, and must satisfy the non-negativity conditions,

$$\mu^- \geq 0, \quad \mu^+ \geq 0, \quad (3.34)$$

switching conditions

$$\mu^- x = 0, \quad \mu^+(x - 1) = 0 \quad (3.35)$$

and inequality constraint

$$\frac{V(x)}{V_0} \leq \eta. \quad (3.36)$$

Following the derivation of Bendsøe and Sigmund (2011) for the necessary conditions of optimality, a numerical scheme that updates the design variable locally, at each material point, can be formulated. This design update rule is a piece-wise function that given the state and design variables of iteration n , returns the design variables of the next iteration, $n + 1$, via the mathematical form

$$x^{n+1} = \begin{cases} \max\{(1 - \zeta)x^n, 0\} & \text{if } x^n B^n \leq \max\{(1 - \zeta)x^n, 0\} \\ \min\{(1 + \zeta)x^n, 1\} & \text{if } \min\{(1 + \zeta)x^n, 1\} \leq x^n B^n \\ x^n B^n & \text{otherwise} \end{cases} \quad (3.37)$$

where B^n is given by the expression

$$B^n = \left(\frac{\rho^n}{\mu^n/p}\right)^\beta, \quad (3.38)$$

ζ is a move limit, and β is a tuning parameter. Bendsøe and Sigmund (2011) propose to set ζ and β to 0.2 and 0.5, respectively. While Setoodeh et al. (2005) propose to express β as a function of p ,

$$\beta = \frac{1}{1+p}, \quad (3.39)$$

and do not mention use of move limits.

Eq. (3.30), (3.31), (3.32), (3.37) and the linear elastic equilibrium problem constitute the continuous formulation of the minimum compliance problem for a constant stiffness material. However, the degree of anisotropy of the material can also be designed from point to point using an orientation design rule. Because the stiffness C_{ijkl} has been formulated, in Eq. (3.31), as the product of two independent variables, the topology can be simultaneously updated along with the reinforcement orientation. Consider, u_m , a spatially-varying vector field that defines the point-wise orientation of a multi-thread material. A design rule that locally updates the orientation of a multi-thread material can be formulated based on the heuristic of stress trajectories. By aligning the reinforcement of a given topology with the direction of the maximum principal stress, the compliance of the structure is minimized. This minimum may not be a global minimum. Moreover, as demonstrated by Brandmaier (1970) for plane-stress strength maximization and by Pedersen (1989) for plane-stress stiffness maximization, depending on the relative shear stiffness of the material the optimal orientation may not be aligned with the principal stress direction. However, as empirically shown in chapters 5 and 6, the use of this orientation criteria minimizes structural compliance, as compared with constant stiffness topologies, without the need for gradient computation. Thus allowing for an initial assessment of this new 3D design framework in large-scale problems. Furthermore, when transitioning the framework to

gradient-based methods, it may serve as a reference to measure the benefits of using gradients in the optimization. Replacing these optimality criteria with gradient-based methods is outlined in Section 7.3 as future work. Also, note the lack of manufacturing constraint formulation on the topology and the orientation distribution.

3.4 NUMERICAL SOLUTION ALGORITHM

The numerical solution, to Eqs. (3.3), involves two discretization schemes. On the one hand, the displacements are discretized at the nodes to solve the linear elastic problem, using a traditional finite element approximation. On the other, the spatial variations of C_{ijkl} are approximated using the same finite element mesh yet independent interpolation functions. The interpolation functions that operate on C_{ijkl} serve the purpose of approximating C_{ijkl} at the integration points required by the displacement-based finite element analysis procedure. By virtue of Eq. (3.32), the density field becomes discretized to nodal density values, $x[n]$, that parameterize the nodal Young modulus, $E_L[n]$, as

$$E_L[n] = E_{L,\min} + x[n]^p(E_{L,\text{nom}} - E_{L,\min}), \quad (3.40)$$

where n denotes the node label.

It is assumed the finite element analysis procedure uses a single-point reduced quadrature to evaluate the element stiffness matrix. To approximate C_{ijkl} at these element-wise integration points, two interpolation functions are considered: linear and reciprocal. Thus the stiffness tensor, for element e , can be approximated as

$$C_{ijkl}[e] \approx (1 - \lambda)C_{ijkl}^{(0)}[e] + \lambda C_{ijkl}^{(1)}[e] \quad (3.41)$$

where $C_{ijkl}^{(0)}[e]$ is the linear interpolation function which, for a regular mesh, is given by

$$C_{ijkl}^{(0)}[e] = \sum_{n \in N_e} E_L[n] \hat{C}_{ijkl}[n], \quad (3.42)$$

where the summation is performed over the set N_e that contains all the n nodes that belong to element e ;

$C_{ijkl}^{(1)}$ is the reciprocal interpolation function, expressed for a regular mesh, using a matrix form as

$$[C_{ijkl}^{(1)}]^{-1} = \sum_{n \in N_e} \frac{1}{E_L[n]} [\hat{C}_{ijkl}[n]]^{-1}, \quad (3.43)$$

and λ is an algorithmic parameter, bounded to vary between $[0, 1]$, that weights one interpolation function against the other.

Since density variables are centered at the nodes, the structural volume is approximated using the composite trapezoidal rule which for a rectangular 2D domain can be written as

$$V(x) = \int x d\Omega = \sum_e \int \int x d\sigma d\tau \approx \sum_e \frac{1}{4} \sum_{q \in N_e} x[n]. \quad (3.44)$$

Generalization to a 3D parallelepiped domain, using iterative integrals, is trivial.

Eqs. (3.42) and (3.43) formulate the non-dimensional tensor \hat{C}_{ijkl} at the nodes. However, since Section 3.30 formulated the reinforcement orientation update rule using stress trajectories, the design variables $\phi[e]$ and $\psi[e]$ (which denote the orientation of a perpendicularly reinforced thread plane) will be centered at the elements. By centering the orientations at the elements, the eigenvalue computation of an element stress is more accurate than if the stress were to be averaged to the nodes. The spatial approximation of $\hat{C}_{ijkl}[e]$ from the elements to the nodes is done via inter-element nodal averaging

$$\hat{C}_{ijkl}[n] = \frac{1}{\rho[n]} \sum_{e \in N_n} \rho[e] \hat{C}_{ijkl}[e], \quad (3.45)$$

where $\hat{C}_{ijkl}[e]$ is computed using Eq. 3.16 as a function of $\phi[e]$ and $\psi[e]$, $\rho[e]$ is the element strain energy density and $\rho[n]$ is given by

$$\rho[n] = \frac{1}{n} \sum_{n \in N_n} \rho[e]. \quad (3.46)$$

Note that averaging the element \hat{C}_{ijkl} , with $\rho[e]$ as a weight, returns a non-dimensional anisotropy \hat{C}_{ijkl} that is only influenced by the anisotropy of solid points.

Analysis coupling: Eq. (3.42) and Eq. (3.43), design update rules: Eq. (3.37) and stress trajectories, and a displacement-based finite element analysis procedure are the computational elements of the solution algorithm. This solution algorithm can be described in terms of two nested iteration loops. The inner-most iteration loop is an optimization cycle. The optimization cycle starts with a current design given by $x[n]^k$, $\theta[e]^k$ and $\phi[e]^k$; analyzes the structural performance of design iteration k and, based on these responses and design rules, updates the design to $x[n]^{k+1}$, $\phi[e]^{k+1}$ and $\psi[e]^{k+1}$ using fixed-point iteration. The outer-most iteration loop is a continuation scheme that changes different algorithmic parameters such as the interpolation function. In a continuation scheme, the optimization problem is solved multiple times with different initial designs $x[n]^0$, $\phi[e]^0$ and $\psi[e]^0$. A continuation scheme is a multi-step sequential procedure, where the initial design of the l optimization step is the optimized design result of the $l - 1$ optimization step. Each time an optimization is run several algorithmic parameters are changed. These changing algorithmic parameters can be combined into a tuple that configure the optimization solver. In this work the configuration tuple is given by

$$(p, \lambda, \epsilon_x) \quad (3.47)$$

where ϵ_x is the threshold value used in the stopping condition of the optimization cycle, defined as

$$\epsilon_x = \max\{|x[1]^{k+1} - x[1]^k|, \dots, |x[n]^{k+1} - x[n]^k|, \dots\}. \quad (3.48)$$

For example, the tuple $(3, 0, 0.01)$ configures the optimization to use linear interpolation. Conversely, the tuple $(3, 1, 0.01)$ configures the optimization to use reciprocal interpolation. Using a tuple notation, the continuation scheme can be mathematically described as a vector of tuples. For example,

$$[(1, 0, 0.01), (2, 0, 0.01), (3, 0, 0.01)] \quad (3.49)$$

represents the node-centered equivalent of the traditional continuation scheme, solely focused on the p parameter. This work proposes, in addition, to switch the interpolation functions between steps. Moreover, because numerical experience has shown that the first optimization step, which uses linear interpolation, becomes unstable when approaching the optimal point, the solution algorithm is defined by the following vector of tuples:

$$[(1, 0, 0.1), (1, 1, 0.01), (2, 1, 0.01), (3, 1, 0.01)] \quad (3.50)$$

By relaxing the tolerance of the first optimization step, the number of iterations is significantly reduced. The gray scales that may result from such relaxed optimal topology are subsequently treated by increasing the penalization and using reciprocal interpolation (which itself is an implicit form of penalization).

The solution algorithm, defined by the configuration vector (3.50), is a heuristic because there is no mathematical guarantee that the converged topology is a global optimum. By solving a fictional convex problem and subsequently finding black-and-white topologies within the neighborhood of that fictional optimum, it is hoped to achieve better performing topologies. This expectation can only be confirmed numerically on a case-by-case basis. The following section proposes a plan of test cases to assess this solution algorithm.

In summary, these nested iteration loops (that define the solution algorithm) are illustrated in Figure 3.6 with the aid of an extended design structure matrix (XDSM). The reader is referred to Sec. 2.1.1 for a review of the XDSM construction process, developed by Lambe and Martins (2012). The Lagrange multiplier solver, shown in Fig. 3.6, is described in more detail in Appendix C.

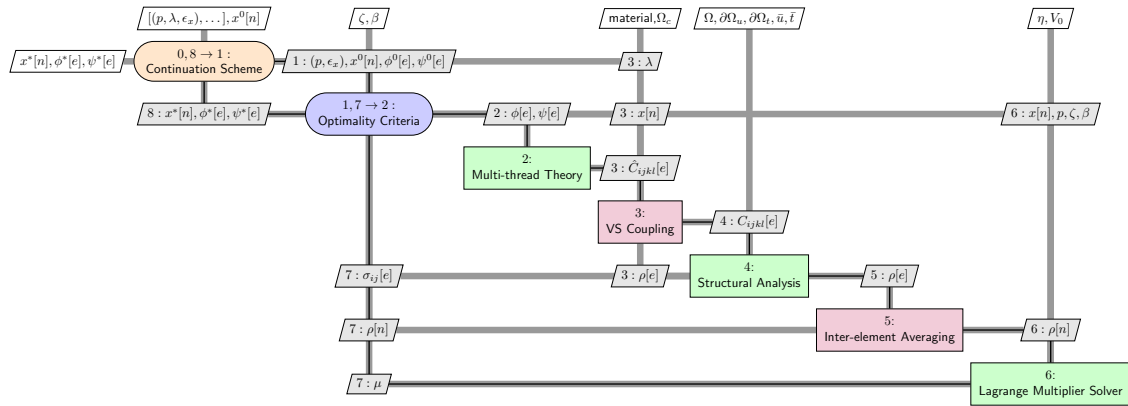


Figure 3.6: XDSM diagram of the numerical solution algorithm

3.5 TEST PLAN

Section 3.1 and Section 3.2 presented a methodology for 3D design of fiber-reinforced composites. To complete the framework of study, Section 3.30 and Section 3.4 formulated a simplified design problem along with an algorithm to numerically solve it. This section presents an experimental design that aims to investigate the feasibility of this 3D design framework. In particular, it assesses the benefits of using a 3D design framework as compared to current 2D design frameworks. The factors that will be changed in these experiments include the number of spatial dimensions, the type of spatial variation and the degree of anisotropy.

Chapter 5 presents and discusses the results of tests with 2 spatial dimensions or 2D. While chapter 6 presents and discusses the results of 3D tests. The types of spatial variation considered are a material variation or a material and anisotropy variation. A material variation involves a topology optimization, whereas a variation of material and anisotropy refers to a simultaneous topology and reinforcement orientation optimization.

Materials with three different degrees of anisotropy are considered: isotropic, transversely isotropic and orthotropic. The isotropic and transversely isotropic materials used in these tests are defined by the engineering constants of appendix A. Whereas an orthotropic material is obtained by lamination (for 2D tests) or using a plane of transversely

Table 3.2: Plan of numerical experiments to study the proposed 3D framework.

test case	dims.	spatial variation of	degree of anisotropy	purpose
1	2D	material	isotropic	verification
2	2D	material	transversely isotropic	exploration
3	2D	material, anisotropy	transversely isotropic	exploration
4	3D	material	isotropic	verification, exploration
5	3D	material	orthotropic	verification, exploration
6	3D	material, anisotropy	transversely isotropic	exploration

isotropic threads. Note that simultaneous optimization tests are only available for a transversely isotropic thread with a 2D or 3D orientation.

Table 3.2 summarizes 6 test cases based on the changing experimental factors. Moreover, Table 3.2 labels the purpose of each test case as a verification or exploration or both. A verification test case aims to demonstrate consistency of results, either against results of the literature or against previous test cases. On the other hand, an exploration test case aims to evaluate a benefit or limitation of the framework without a priori knowledge.

CHAPTER 4

SPECIFICATIONS FOR A TOPOLOGY OPTIMIZATION TOOLKIT

To implement the 3D framework proposed in Chapter 3, software design specifications are presented herein. These specifications outline a set of tools useful for topology design optimization research, not an application program. An application program provides a solution to a design problem. While this toolkit provides the necessary tools to build such a solution.

The strategy used to bring conceptual integrity to this collection of tools is named: the MARIA computation strategy. A MARIA computation is a computation invoked with succinct language. It stands for the McNAIR Interface for Abbreviated (MARIA) computation. Rooted in the philosophy that programming effort is more expensive than computational effort, a MARIA computation is a computation invoked by using a programmatic interface expressed in a high-level vocabulary specific to the domain of study. Also called a domain specific language.

Applying the MARIA computation strategy to topology optimization results in three domains. Each with its associated library. First, Sec. 4.1 defines software specifications for a library that supports modeling the macro-mechanical behavior of fiber-reinforced composites. Second, Sec. 4.2 defines software specifications for a library that supports modeling a parameterized variable stiffness field for coupling with structural analysis. Finally, Sec. 4.3 defines software specifications for a library that supports modeling design cycles and aids in coupling them to iterative solvers. These software specifications use

Python syntax to define classes, methods and function specifications.

4.1 MARIA COMPOSITES

The MARIA composites library should provide macromechanics models based on classical laminate theory and multi-thread theory. Sec. 4.1.1 reviews the interface specifications for multi-thread theory, while Sec. 4.1.2 presents the specifications for classical laminate theory.

4.1.1 MULTI-THREAD THEORY

Multi-thread theory should be supported by the `Thread` class and its container the `MultiThread` class. A `Thread` is defined by a transversely isotropic material and a `VectorOrientationIn3DSpace` or a `VectorOrientationIn2DSpace` orientation.

```
myOrientation = VectorOrientationIn3DSpace(theta=0.0,  
                                           phi=np.pi/4)  
myThread = Thread(material='NUND1',  
                  orientation=myOrientation)
```

where the vector orientation is parameterized in terms of the Tait-Bryan rotation angles `theta` and `phi`. The reason for having different classes for the orientation and the fiber-matrix architecture is to future-proof the library against different orientation parameterizations. By charging `VectorOrientationIn3DSpace` with computing the direction cosine matrices, the concern of using rotation angles or quaternions is separated from the transformation of the stiffness tensor. Which is responsibility of `Thread`. The material is defined by a string that specifies its name in a given materials database. This assumes the engineering constants of the material remain fixed throughout the design process.

The Thread class must provide a managed attribute called `stiffness` that computes the stiffness, using multi-thread theory, upon request. Thus, to update the stiffness of the thread due to a change in orientation the following code must be written

```
myThread.orientation.theta = np.pi/4
newStiffness = myThread.stiffness
```

The `MultiThread` class is of little use for design optimization, but its children are. The `ThreadPlane` class allows to define a plane of isotropy with a generic orientation. The orientation of the plane can be specified by the orientation of the plane normal with `PlaneOrientationIn3DSpace` or as two axes of a `CartesianCoordinateSystemIn3DSpace`. The degree of anisotropy of the plane is defined with in-plane stiffness parameters. For a plane of isotropy the code should read as

```
myOrientation = PlaneOrientationIn3DSpace(phi=0.0, psi=0.0)
myPlane = ThreadPlane(material='NUND1',
                       inPlaneStiffnessParameters=[0,0,0,0],
                       orientation=myOrientation)
```

The `PerpendicularReinforcedThreadPlane` is similar to the `ThreadPlane` with an additional `muPerpendicular` argument.

To facilitate a succinct update of the stiffness for many different orientations, the `ReferenceVolumeElement` class is defined. The `ReferenceVolumeElement` class is a wrapper on top of the multi-thread system of choice that allows specifying which orientation variable will change from point to point. The instantiation of a `ReferenceVolumeElement` requires all the arguments needed to define a multi-thread system and its orientation

```
arrangement = {'type': 'ThreadPlane',
               'inPlaneStiffnessParameters': [0,0,0,0]}
```

```
orientation = {'phi': 0.0, 'psi': 0.0}
myRve = ReferenceVolumeElement(arrangement = arrangement,
                               orientation = orientation)
```

where the orientation object should be automatically selected based on the keywords specified.

Moreover, the `ReferenceVolumeElement` class must provide a `stiffness` attribute that updates automatically once the design variables are updated. For example, a potential optimization problem may only vary the `psi` orientation of a thread plane. The code that updates the stiffness of the thread plane based on the `psi` orientation must read as

```
myRve.psi = np.pi/3
newStiffness = myRve.stiffness
```

4.1.2 CLASSICAL LAMINATE THEORY

Classical laminate theory should also be supported with the same behavior. The orientation must be defined via a `VectorOrientationIn2D` class, the material should be defined by name to a given materials database and the parameterized laminate must be wrapped in a `ReferenceSurfaceElement`.

However, certain utilities particular to laminates should also be provided. To aid with a more human-friendly definition of a stacking sequence, a parser called `stackingSequenceParser()` that understand shorthand notation must be provided.

```
stackingSequenceParser('[(+-45/0)_s/90_2]_2')
>>> [+45, -45, 0, 0, -45, +45, 90, 90, ...
      +45, -45, 0, 0, -45, +45, 90, 90]
```

where the input is a string with symbolic notation, yet the output is a list of floating point numbers amenable to define a `Lamina`. The `Lamina` class is used to define a `Laminate` class as a list of `Lamina`. For example, a laminate made of one ply should be defined as

```
ply = Lamina(material='NUND1', theta=0.0)
myStack = Laminate([ply])
```

which is also a list with the attribute `stiffness` that should compute the A , B and D matrices.

By using a mutable list of `Lamina` instances to define a laminate, several operations are facilitated. For example, dropping the second ply from a three-ply laminate should read as

```
myStack = Laminate([thisPly, thatPly, anotherPly])
myStack.pop(1) #pop out thatPly
```

whereas adding that ply back should read as

```
myStack.insert(1, thatPly)
```

Combining two sub-laminates should read as

```
myStack = thisStack + thatStack
```

4.2 MARIA ANALYSIS

The MARIA analysis library should support a finite element based structural analysis with a variable stiffness field. Two top-level classes that support this analysis procedure are called `VariableStiffnessField` and `StructuralAnalysis`.

A finite element analysis is modeled as a three-step process that starts with the preparation of an input file. Then solves the system of equations, defined by such input file, for the nodal displacements. Finally, it recovers quantities of interest like stress

or strain energy density. The MARIA analysis library must assist in the preparation of the stiffness properties for the input file and in managing the calls to a third-party finite element solver via an analysis pipeline. The former functionality should be provided by the `StiffnessField` class specified in Sec. 4.2.1. The latter should be provided by the `StructuralAnalysis` class specified in Sec. 4.2.2.

4.2.1 VARIABLE STIFFNESS FIELD

The stiffness tensor C_{ijkl} is a rank-4 tensor that can vary from point to point within the structural domain. Other quantities of interest, like the elastic strain energy, are also spatially distributed. Moreover, the distribution may be discretized to be centered at the elements or nodes. To store and spatially approximate any tensorial quantity, the `Distribution` class is defined. The `Distribution` class must have an attribute called `values` which is of a 2D array type. A row in the array represents the tensorial components of the quantity at the node or element whose label is given by the index of the row.

The `Distribution` class must provide a method that spatially approximates the values of the quantity from the nodes to the elements, `toElems()`, or if the quantity was initially defined at the elements to the nodes, `toNodes()`. To enable this spatial approximation the class instance must be initialized with the following arguments

```
myDistro = Distribution(location='atNodes', mesh=mesh,  
                        approxAs='reciprocal', tensorRank=4)
```

where `location` denotes where the quantity is centered. Either `'atNodes'` or `'atElems'`. The `mesh` class instance contains the XYZ coordinates of each node and the connectivity of the elements. The `approxAs` argument specifies the type of approximation function used. In this case, `'reciprocal'` interpolation. And the `tensorRank` denotes the rank of the tensorial quantity for approximation. For example, a

quantity of `tensorRank=4` with a `'reciprocal'` approximation requires computing the inverse of the matrix form of the tensorial quantity.

The `Distribution` class is used to define a spatially varying stiffness tensor and its distributed design variables. The `VariableStiffnessField` class specifies an interface for defining such a stiffness tensor with spatially distributed variables. Like a distribution, the `VariableStiffnessField` must be initialized with a `location`, `mesh` and `approxAs` arguments

```
varspecs = {'density': {'location': 'atNodes',  
                        'approxAs': 'linear',  
                        'tensorRank': 0}}  
myField = VariableStiffnessField(location='atNodes',  
                                 mesh=mesh,  
                                 approxAs='reciprocal',  
                                 varspecs=varspecs)
```

However, unlike a distribution the stiffness field has additional specifications for its design variables. Assuming all quantities share the same mesh, the design variable specifications should not include a `mesh` argument. The `varspecs` argument serves to initialize the `variables` attribute of the stiffness field as a dictionary of distributions. Thus allowing a design variable update to be specified as

```
myField.variables['density'].values = [[1], [1], [0], [0]]
```

Also unlike a distribution, the field is assumed to be defined by a computational law, `law()`, that uses the values of its design variables to compute the values of the stiffness tensor. This `law()` method must be programmed by the user in the optimization script, and is expected to be defined with classes from the MARIA composites library of Sec. 4.1. Thus, the `VariableStiffnessField` class is a base class that must be inherited into a custom stiffness field in the optimization script.

Overall, when a new value, `xnew`, of the design vector is provided the `VariableStiffnessField` class should be updated as follows

```
myField.variables['density'].values = xnew
myField.law() # update stiffness values
cijklNew = myField.toElems()
```

where `cijklNew` is the updated element-centered stiffness properties that can be written into an input deck for structural analysis.

4.2.2 STRUCTURAL ANALYSIS

A finite element analysis is modeled as a three-step process that starts with the preparation of an input file. Then solves the system of equations, defined by such input file, for the nodal displacements. Finally, it recovers quantities of interest like stress or strain energy density.

The input file preparation assumes a deck of cards metaphor. A main input file that can include links to other files that also define certain aspects of the finite element model can be described as a deck of cards. One card of the input deck is the spatially distributed element-centered stiffness properties. The `VariableStiffnessField` class is in charge of generating such information. The `GroundStructure` class generates the remaining cards of the input deck.

The `GroundStructure` class generates the input file by calling a feature-based modeling script. Several off-the-shelf finite element solvers, like Abaqus, provide a scripting interface to model the problem using features. These features, for example, allow to apply a boundary condition on a geometrical edge, rather than at discrete nodes. The `GroundStructure` class must provide a method called `generate()` that calls this modeling script and generates the input deck, save for the stiffness properties.

Moreover, the `GroundStructure` shall be able to read the mesh information from this input deck. The mesh information is needed to initialize any `Distribution` based

class instance, such as `VariableStiffnessField`. It is also the responsibility of `GroundStructure` to compute its volume given a nodal density vector `x`

```
vol = myGroundStructure.volume(x)
```

The second step involves calling an off-the-shelf finite element solver. Implementing this call is particular of the solver of choice and will not be discussed in this work. However, to integrate the finite element solver with this library the `StructuralAnalysis` class is specified. It is composed of the `GroundStructure` and the `solve()` method, which must implement the call to the finite element solver and return the responses of interest. The initialization of `StructuralAnalysis` must call the `generate()` method of the `GroundStructure` to have a complete setup of the finite element analysis pipeline with the following lines of code

```
myAnalysis = StructuralAnalysis(args)
mesh = myAnalysis.groundStructure.mesh
myField = VariableStiffnessField(mesh=mesh, otherArgs)
```

whereas a design evaluation should be implemented as

```
myField.variables['density'].values = xnew
myField.law() # update stiffness values
cijklNew = myField.toElems()
# write cijklNew to input file
myAnalysis.solve()
myAnalysis.cleanUp()
```

where the `cleanUp()` method is needed when using an I/O communication style between the finite element solver and this library.

4.3 MARIA DESIGN

The MARIA design library is comprised of utility modules and discipline sub-packages. For example, this work has as disciplines the `topology` and `curvilinear_fibers` sub-packages. Each design discipline contains a list of callable design rules with all its algorithmic parameters. A design rule is a mathematical function whose output is an updated design. Its input arguments are fully explicit and are of two types. Algorithmic parameters tune the search behavior and are normally fixed throughout iterations, while design variables and responses change on every iteration. For example, the topology design rule proposed by Bendsoe and Sigmund (2011) may have an interface as

```
ruleOfBendsoe(x, phi, mu, penal, xeps=None,  
              move=0.2, eta=0.5)
```

where `x`, `phi` and `mu` are problem variables, while `penal`, `xeps`, `move` and `eta` are algorithmic parameters which may have default value definitions.

Because most optimization scripts define the algorithmic parameters once, yet call these design rules many times during iteration, a callable `DesignRule` class must be available. This class must be initialized with the fixed values of algorithmic parameters. Using the `ruleOfBendsoe()` function as an example, the initialization of the wrapper class must be

```
myRule = DesignRule(name='Bendsoe',  
                    algParams={'move' : 0.3, 'eta' : 0.25})
```

where `myRule` is an instance of the class which has the attribute of being callable just like the `ruleOfBendsoe()` function

```
myRule(x, phi, mu)
```

The algorithmic parameters of the `DesignRule` class must be mutable via an attribute

```
myRule.algParams['eta'] = 0.5
```

when needed by the continuation scheme or for post-optimality analysis.

To combine multiple design rules and implement additional logic, like a Lagrange multiplier computation, the `UpdateScheme` class is specified. An `UpdateScheme` is composed of several design rules and of logic that calls the rules with the needed arguments. An instance of the `UpdateScheme` class must be callable and return the updated design variables. For example, an update call is given by

```
xnew = myUpdateScheme(x, f)
```

where x is the design vector comprised of both densities and fiber orientations, and f is the responses of x . The `UpdateScheme` class is responsible for breaking x and f down before passing them to each design rule. It is also in charge of recording x and f over time to obtain a `ConvergenceHistory`. The `ConvergenceHistory` class stores values of several history variables of interest. In particular, the design vector x and the responses f . Like the `Distribution` class of Sec. 4.2.1, each history variable is a 3D array where the rows and columns store the values of distributed tensorial quantities. However, in this case the depth shows the history of the tensorial quantity as the design process progresses.

The design optimization process is modeled as having three main steps: (i) initialization, (ii) iteration, and (iii) interpretation. Such process involves two actors. A solver and a manager. The solver is an iterative algorithm that updates the design based on a prescribed update scheme and has the decision-making logic to know when to stop based on stopping conditions. It is a loop of analyze and update until the stopping conditions are met. The manager is charged with the setup and teardown of the design optimization process. It initializes the objects that are needed for the design optimization and persists the data based on the convergence status. By persisting the data the interpretation step can begin. The purpose of ‘`ConvergenceHistory`’ is to provide functionality that exports optimization data for interpretation and allows the definition of initial design variable distributions of any kind. If a continuation scheme is to be used, the optimization script must be able to accept a non-uniform initial design.

Finally, the highest level class is the `DesignCycle`. A `DesignCycle` class is a base class with three non-implemented methods. The initialization method of the class must instantiate all the above mentioned classes within `DesignCycle`. Figure 4.1 illustrates this class hierarchy. The `evaluateDesign()` method must implement a finite element analysis of the design as exemplified above. While the `run()` method uses `UpdateScheme` and the iteration algorithm of choice to cycle through the process until an optimized solution is found.

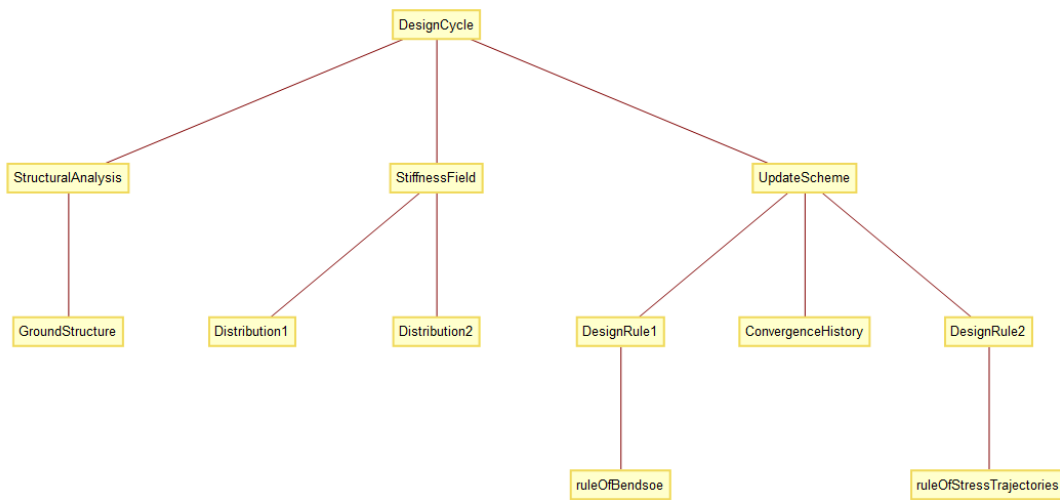


Figure 4.1: Class hierarchy of a `DesignCycle`

CHAPTER 5

2D TOPOLOGY OPTIMIZATION OF FIBER-REINFORCED COMPOSITES

The 3D framework of chapter 3 can be simplified to perform 2D topology optimization studies. This chapter presents a set of such results for the 2D MBB beam case study. Based on the test plan, shown in Table 3.2 of chapter 3, this chapter is organized as follows. Section 5.1 formulates the 2D MBB design problem and the simplified algorithm used to solve it. Section 5.2 presents results for an isotropic MBB, while Section 5.3 studies transversely isotropic materials. The isotropic MBB study objective is two-fold. First, to compare the optimized topologies that result from linear interpolation, reciprocal interpolation, and the continuation scheme techniques as the mesh is refined. Second, to evaluate the speed of convergence of these techniques and how this speed varies as the mesh gets refined. The transversely isotropic MBB study aims to vary the orientation angle of a uni-directional material and observe the resulting optimal topologies. The intent of such experiment is not to investigate the advantages of purposeful anisotropy. Rather, the focus is on the interaction of this directionality with the behavior of the solution algorithm. In particular, the local behavior it may cause to the reciprocal interpolation technique. The full-factorial design of these two materials totals 102 topology optimization runs, with more than 8000 finite element simulations. The design history of these optimization runs (defined as the history of the nodal densities and nodal strain energy densities) was compiled into a database, available in https://github.com/USCMcNAIR/mbb_2d_constant_stiffness as a collection of raw data files or as an HDF5 Group (1997) standalone binary file. What

follows is an analysis of the data stored in such database.

The previous studies assume a material with a constant degree of anisotropy throughout the domain. If the degree of anisotropy can vary from point to point due to a change of fiber orientation, then the topologies will also change. Results for a curvilinear fiber format MBB are presented in Section 5.4. Finally, to 3D print these 2D topologies a post-processing algorithm that uses image-processing techniques is formulated in Section 5.5.

5.1 MBB 2D PROBLEM

The MBB 2D-beam problem is a simply supported beam with a concentrated load applied mid-length. The beam is modeled using a regular mesh of quadrilateral 4-node elements. Figure 5.1 illustrates the symmetric part of this structural analysis problem, which has been modeled using the Abaqus finite element analysis code (Dassault Systemes 2017), with S4 elements.

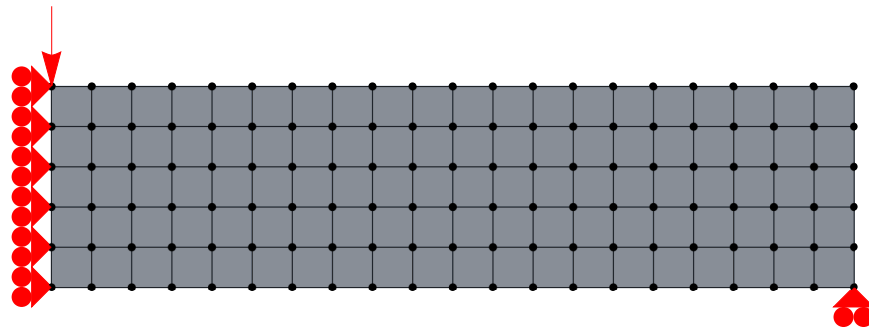


Figure 5.1: Symmetric part of a 2D MBB meshed with rectangular S4 finite elements

The geometry of the MBB beam and algorithm parameters are taken from Andreassen et al. (2011). Consequently the aspect ratio of the symmetric part is 3, the penalization is $p = 3$, and the optimality criteria parameters are defined as

$$\zeta = 0.2, \quad \beta = 0.5$$

Aside from the continuation scheme, the stopping condition is set to $\epsilon_x = 0.01$. The continuation scheme is defined by Eq. (3.50).

The volume constraint is set to 50%. Accordingly, the initial density field is a uniformly distributed field of value 1/2. This ensures a feasible initial design, and represents the worst case scenario for topology optimization. Any converged MBB topology that is more deformable than this initial design renders the solution algorithm useless, because a uniform reduction of the plate thickness would deform less and still achieve the same weight savings.

The simplified algorithm uses classical laminate theory (which assumes plane stress) instead of multi-thread theory. Everything else remain the same. Figure 5.2 shows, via an XDSM diagram, the simplified optimization algorithm used in this chapter.

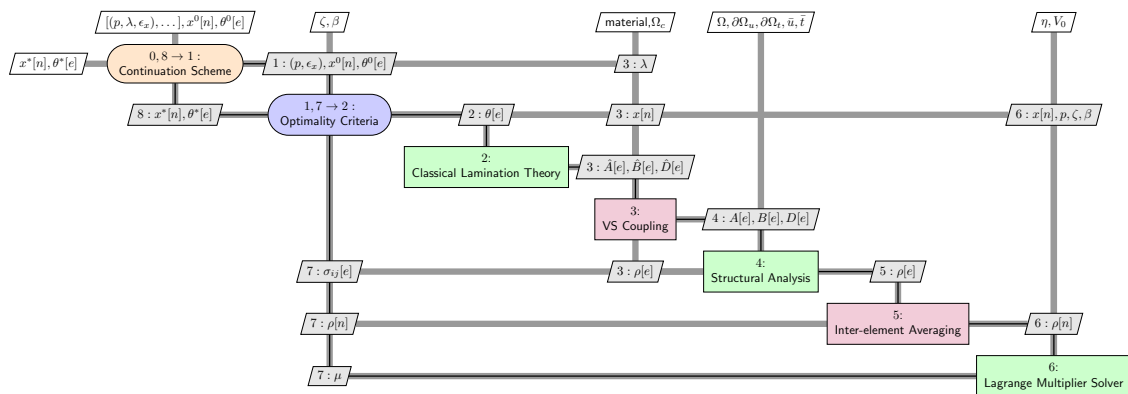
































Figure 5.2: XDSM diagram of solution algorithm used for the MBB 2D problem

5.2 ISOTROPIC MBB

This study refined the finite element mesh of an isotropic MBB beam, using material NISO1 from appendix A, from a 10-by-30 mesh to a 100-by-300 mesh by refining the width dimension with 10 additional elements every time. The length dimension has been refined to maintain square finite elements. For each mesh size, the linear interpolation, reciprocal interpolation, and continuation scheme techniques were used to find the

Table 5.1: Optimized MBB topologies for varying mesh sizes obtained by linear interpolation, reciprocal interpolation and continuation scheme techniques for an isotropic material

elem. width	linear	reciprocal	continuation
10			
20			
30			
40			
50			
60			
70			
80			
90			
100			

optimized topology of the MBB beam. A sample of these topologies is shown in Table 5.1, where each column indicates a different optimization technique whereas each row indicates a finer mesh.

Since the techniques did not incorporate a length-scale control mechanism, it is

unsurprising to find structural members of a smaller scale present in all techniques. The last three rows of Table 5.1 serve as example of these smaller scale members. However, larger scale members, for all techniques, do not suddenly disappear as the mesh is refined. Neither do they suddenly change orientation or thickness. It is rather gradual.

Table 5.1 also reveals that the optimized topologies of the three studied techniques are markedly different, they are a different local optimum. To compare these local optima in terms of compliance, the optimized topologies were refined to a common 100-by-300 mesh and a post-optimality analysis, with no density penalization and using linear interpolation, was performed. Figure 5.3 shows the compliance, measured as the total strain energy and normalized with respect to twice the strain energy of the ground structure, as a function of the number of elements along the beam width.

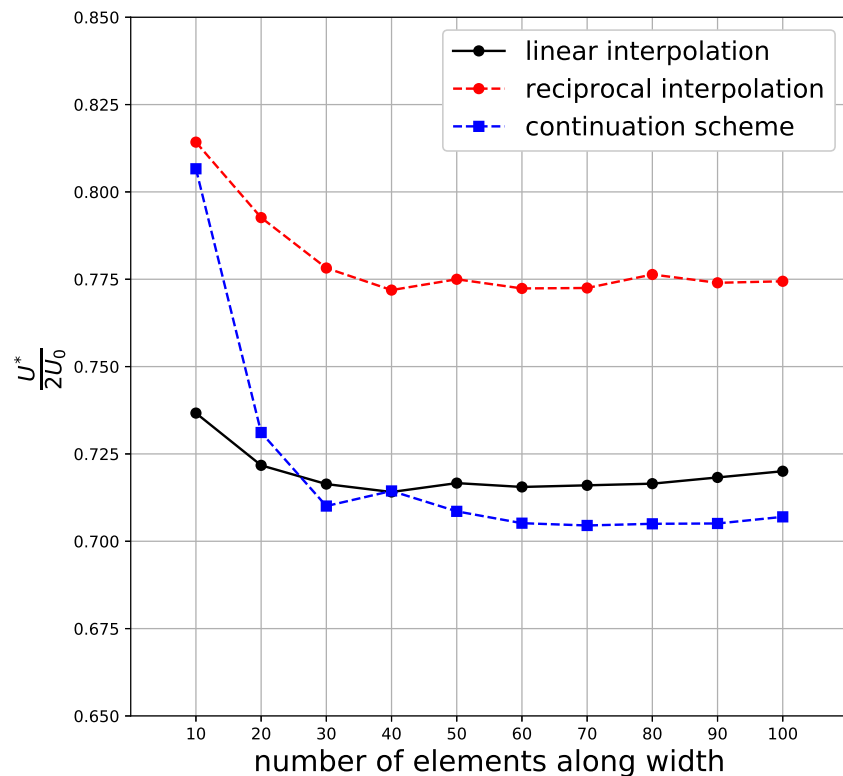


Figure 5.3: Normalized compliance for varying mesh sizes obtained by linear interpolation, reciprocal interpolation and continuation scheme techniques for an isotropic material

The trends in Fig. 5.3 show a stiffening of the optimal topologies as the mesh is

initially refined. This can be explained by the appearance of smaller scale members. However, towards the end of the mesh refinement the compliance seems to plateau or even slightly increase. A comparison of the trends between the linear and reciprocal interpolation techniques, shows that the reciprocal interpolation technique converges to a more compliant local optimum than the linear interpolation technique. Surprisingly, the continuation scheme technique converges, for meshes with more than 30 elements along the width, to a stiffer local optimum than both. An in-between stiffness was a priori expected. Although Fig. 5.3 shows the linear interpolation technique to have stiffer topologies for meshes with less than 30 elements along the width, Table 5.1 suggests this advantage is due to the gray scales present in these topologies. Note that these results were generated with a penalized linear interpolation of $p = 3$.

Apart from black-and-white convergence and structural performance, the speed of convergence measured as the number of iterations is used to assess the computational cost of each technique. Figure 5.4 plots the number of iterations as a function of the number of elements along the width. The number of iterations of the continuation scheme technique are calculated by accumulating the iterations of all steps involved.

The trend of the reciprocal interpolation technique is rather constant for all mesh sizes. Fig. 5.4 indicates a cost of about 50 iterations, regardless of the number of nodal design variables. Conversely, the trend of the linear interpolation technique sharply rises with the number of nodal densities, increasing the number of iterations by an order of magnitude when the number of design variables increases by two orders of magnitude. Clearly, the linear interpolation technique is not well suited for large-scale problems. The trend of the continuation scheme technique shows a stable cost of about 200 iterations until 70 elements along the width, upon when it starts to linearly rise.

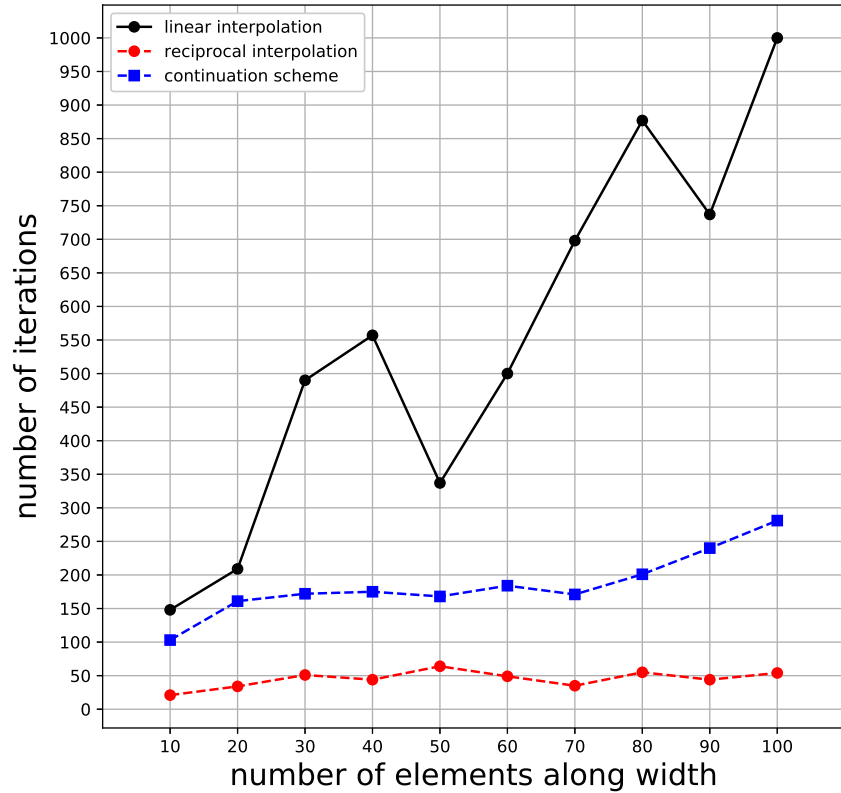


Figure 5.4: Number of iterations required to optimize MBB topologies for varying mesh sizes obtained by linear interpolation, reciprocal interpolation and continuation scheme techniques for an isotropic material






















5.3 TRANSVERSELY ISOTROPIC MBB

This study varies the fiber orientation angle of a uni-directional material, using material NUND1 from appendix A, from a 0 degree orientation (along the length of the MBB beam) to a 90 degree orientation by jumps of 15 degrees. Based on the compared results of Sec 5.2, the mesh is fixed to a 30-by-90 size. Because the continuation scheme technique showed better compliance than the penalized linear interpolation technique, an unpenalized linear interpolation technique is used instead.

Table 5.2 shows the complete combinatorial layout of the optimal topologies of this study, where each column indicates a different optimization technique whereas each row indicates an increasing degree of fiber orientation.

The optimized topologies of the unpenalized linear interpolation and continuation

Table 5.2: Optimized MBB topologies for varying fiber orientation angles obtained by unpenalized linear interpolation, reciprocal interpolation and continuation scheme techniques for a transversely isotropic material

θ	unpenalized linear	reciprocal	continuation
0°			
15°			
30°			
45°			
60°			
75°			
90°			

scheme techniques are similar, save for small holes, until 60 degrees upon when they start to considerably differ. In particular, the unpenalized linear interpolation technique shows the islanding phenomenon, as described by Rahmatalla and Swan (2004), for the 90 degree fiber orientation. The optimized topologies of the reciprocal interpolation technique are markedly different than the other two techniques.

To compare the structural performance of the topologies shown by the reciprocal interpolation technique against the ones from the continuation scheme technique, Fig. 5.5 plots the total strain energy, normalized with respect to twice the strain energy of the 90 degree ground structure, as a function of the fiber orientation angle. Again, these results are post-processed topologies with a 100-by-300 mesh that were analyzed using linear unpenalized interpolation.

With the aim of clarifying this comparison, the sinusoidal behavior exhibited by the strain energy when the fiber orientation angle is varied, is also removed by replacing the fiber orientation angle, θ , as a ratio of two stiffnesses,

$$\frac{A_{11}(\theta)}{\text{tr}(A)}$$

Note that this non-dimensional axis may result unsuccessful in predicting the normalized compliance of optimal laminate topologies whose stiffness falls between these values. Rather it provides a common chart to compare both types of material. The reader who prefers to visualize the fiber orientation angles is referred to the top horizontal axis of Fig. 5.5.

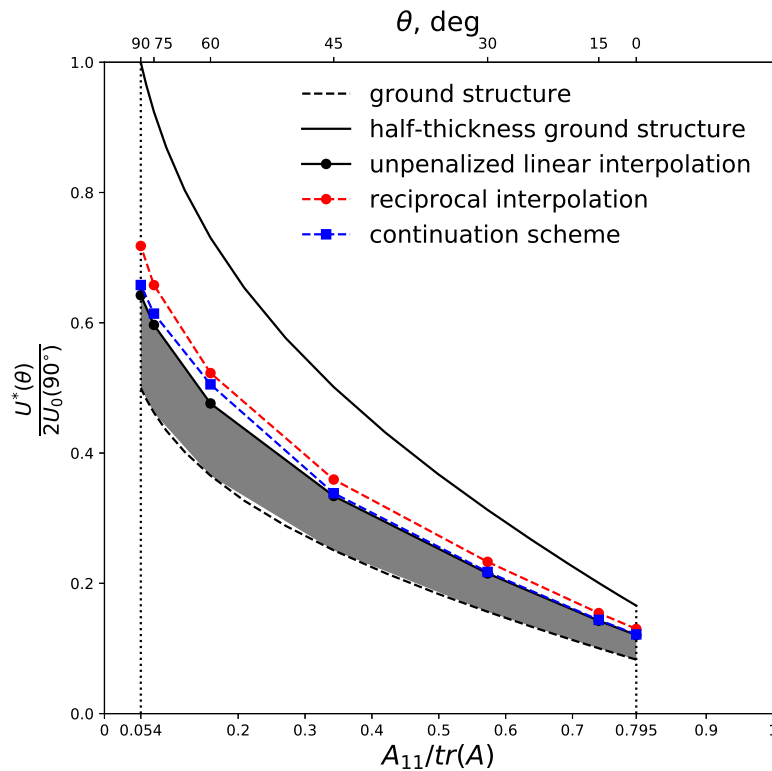


Figure 5.5: Normalized compliance for varying fiber orientation angles obtained by unpenalized linear interpolation, reciprocal interpolation and continuation scheme techniques for a transversely isotropic material. These compliance curves are bounded by a ground structure compliance curve, and twice the ground structure compliance

As heralded by the similar layouts of Table 5.2, the continuation scheme topologies are quite as stiff as the unpenalized linear interpolation ones until 60 degrees. The continuation

scheme topologies with a larger than 60 degree material are more compliant than the unpenalized linear interpolation ones. This gap indicates the cost of having well connected black-and-white topologies. On the other hand, the reciprocal interpolation technique is again shown to have converged to a worse-performing local optimum.

Figure 5.5 also plots the compliance of a ground structure with half its original thickness, to remark the fact that the performance benefits of topology optimization varies with the fiber orientation angle. Moreover, the ground structure compliance is also plotted, in Fig. 5.5, to indicate the stiffness loss due to the lightweighting operation, and the gap between the ground structure compliance and the unpenalized linear interpolation curves is filled to highlight this design space is unattainable with the current solution algorithm.

The computational cost of this study is illustrated in Fig. 5.6. The trends of the reciprocal interpolation and continuation scheme techniques show an incurred cost with similar orders of magnitude than the ones shown in the isotropic MBB study.

The 90 degree uni-directional material proved to be a peculiar case. Not only does it produce islanding phenomenon with the unpenalized linear interpolation technique, it also produces a criss-cross topology pattern when using the reciprocal interpolation technique with $\beta = 0.25$, $\zeta = 10^9$, and a 300-by-100 mesh, as shown in Fig. 5.7.

5.4 CURVILINEAR FIBER FORMAT MBB

The curvilinear fiber format MBB study has the objective of assessing the performance benefits of simultaneously designing the fiber orientation with the topology. The initial fiber orientation distribution is centered at the elements with an orientation angle of 0° . Afterwards, the fiber orientation angles can vary between $(-\pi/2, \pi/2]$.

Because the fiber orientation update rule requires an eigenvalue computation of each elemental stress, the solution algorithm is further simplified to a single optimization step, given by the tuple

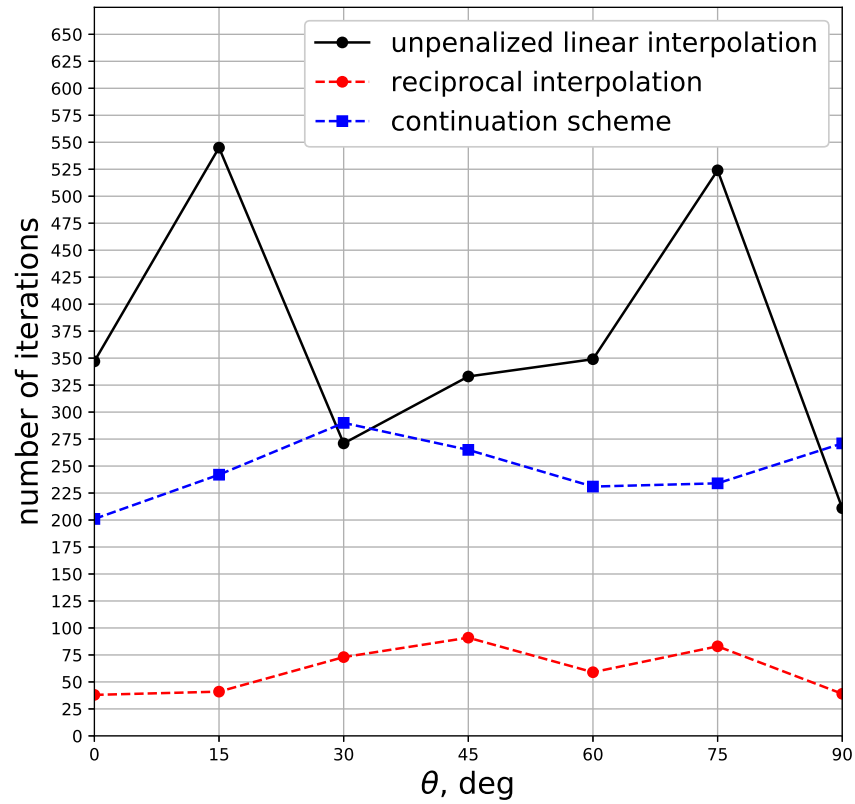


Figure 5.6: Number of iterations required to optimize MBB topologies for varying fiber orientation angles obtained by unpenalized linear interpolation, reciprocal interpolation and continuation scheme techniques for a transversely isotropic material



Figure 5.7: Criss-cross topology pattern shown by an optimized MBB topology obtained with the reciprocal interpolation technique, 300-by-100 mesh, $\beta = 0.25$, $\zeta = 10^9$ for a 90 degree transversely isotropic material

$$(3, 0, 0.01), \quad (5.1)$$

which uses reciprocal interpolation. Thus, reducing computational effort to a minimum.

Figure 5.8 shows the symmetric half of the optimized topology along with the fiber orientation distribution on top of a square mesh. The fiber orientation is illustrated with a segment centered at each element. The segment length is scaled proportionally to the element-centered $E_L[e]^*$. Solid elements have a full-sized segment, while voids have no segment assigned to them. Note in Fig. 5.8 how the fiber segments are aligned along the axis of each curvilinear bar.

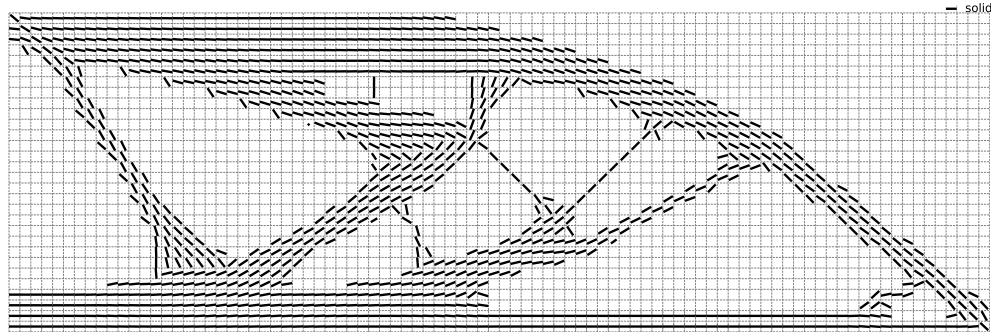


Figure 5.8: Fiber orientation distribution plot of the curvilinear fiber format MBB

The convergence history is comprised of 59 iterations and is shown in Fig. 5.9. The convergence history of Fig. 5.9 shows the variation of the objective function, f , normalized with respect to the initial value of the objective function, f_0 . The objective function is given by the total strain energy of the penalized and reciprocally interpolated topology. The convergence history curve is rather flat during the last 40 iterations.

The performance of the curvilinear fiber format MBB is compared, in Table 5.3, against the 0° straight fiber MBB and their initial ground structure.

Table 5.3 shows that the curvilinear fiber format MBB is 33.7% stiffer than its initial ground structure, even when it is 50% lighter. Compared to the straight fiber 0° MBB it is 54.8% stiffer.

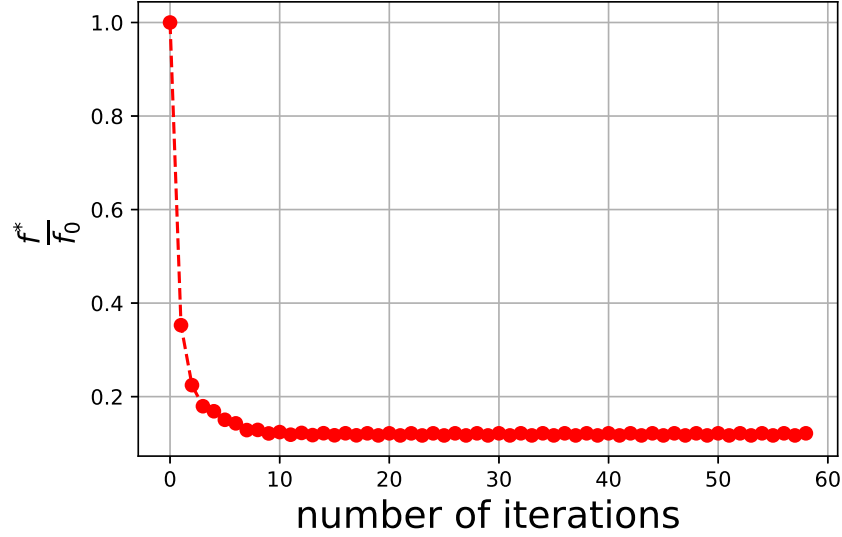


Figure 5.9: Convergence history of the curvilinear fiber format MBB

Table 5.3: Performance metrics of the curvilinear fiber format MBB, straight fiber format 0° and a 0° ground structure

topology	U	η
ground structure	67.99	1
straight fiber 0° optimum	99.72	0.5
curvilinear fiber format optimum	45.08	0.5

5.5 POST-PROCESSING OF 2D NODE-CENTERED TOPOLOGIES

An element-centered description of 2D topologies is a raster image representation of the structure. Where each finite element is a pixel of the image. Several algorithms and tools that recognize the pixelated boundary, smooth it, and export it to an STL file format already exist. For example, The GitHub repository https://github.com/lbahamonde/stl_tools provides Python tools to create an STL file from a raster-based image. However, a node-centered description of 2D topologies is more akin to a vector graphics representation where the boundary can be identified as the density field isoline of value x_b . The following proposes a new post-processing algorithm that leverages the benefits of a node-centered

description of the density field while still using image-processing tools for STL conversion.

It is assumed an optimized topology, such as shown in Fig. 5.10, is provided to the algorithm. Figure 5.10 plots the user-specified nodal density field using linear interpolation. The iso-line x_b slices through the elements linearly and thus provides jagged edges.

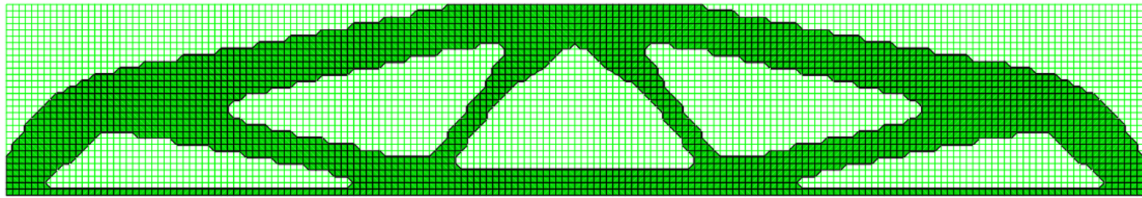


Figure 5.10: Node-centered 2D topology with jagged edges.

To smooth out the jagged edges, the density field is refined into a mesh with a zoom $z = 100$ using a third degree spline with a smoothing factor $s = 3$. Smoothing splines effectively remove the jagged edges of a variable section bar, but may suffer with high order variations around joints where different bars intersect.

This finer mesh of smooth nodal density values is used to identify the boundary as the isoline of value $x_b = 0.3$. This smooth boundary is shown in Fig. 5.11, where the internal structural domain is colored in black. It is not a colormap.

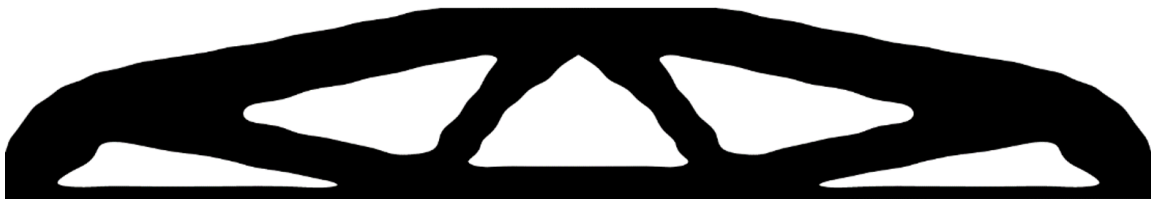


Figure 5.11: Smooth boundary obtained from a node-centered 2D topology with jagged edges.

Until now, the graphical representation of the topology is strictly vector-based. The final step of the algorithm consists in exporting this vector graphic into a raster format with the highest available resolution. Thus packing as many pixels as possible for STL conversion. Exporting Fig. 5.11 into a densely-packed raster format, that is then converted to STL, results in the 3D printed part of Fig. 5.12.



Figure 5.12: 3D printed beam from an STL file generated by processing a smooth boundary image.

Figure 5.12 shows a part built with a Markforged Mark 2 desktop 3D printer. This printer is capable of fiber-reinforced prints as well. The part was scaled to a size of $300.0mm$ by $50.1mm$ by $5.6mm$ and took approximately 6 hours with 21 minutes to print.

CHAPTER 6

3D TOPOLOGY OPTIMIZATION OF FIBER-REINFORCED COMPOSITES

This chapter presents results for 3D topology optimization of the MBB beam problem. A load model compatible with the 2D MBB problem, when the 3D MBB becomes thin, is described in Sec. 6.1. Such section also presents the simplified solution algorithm used in this chapter. The algorithm is then used to explore three different degrees of anisotropy. First, solutions for an isotropic MBB problem are discussed in Sec. 6.2 for different thickness and volume fraction values. Second, an orthotropic MBB model is used to explore the optimized 3D topologies that appear when considering the weak stiffness direction of a layer-by-layer manufacturing approach, such as fused deposition manufacturing. Section 6.3 studies two build directions by using this orthotropic MBB model. Third, a curvilinear fiber format MBB is discussed in Section 6.4 to demonstrate the capabilities of the 3D framework presented in Chapter 3. The curvilinear fiber format MBB uses a transversely isotropic single thread model whose orientation changes from point to point.

6.1 MBB 3D PROBLEM

The MBB 2D-beam problem, of chapter 5, was a simply supported beam with a concentrated load applied mid-length. However, including the third dimension requires remodeling the concentrated load into a through-the-thickness distributed load. This MBB 3D-beam problem formulation is required to have comparable responses to the

2D formulation when the thickness of the MBB 3D-beam is such that the stress state approximates a plane-stress condition. A plane-stress condition is expected to arise for a range of small thickness-to-width t/b values. Moreover, this work's intent behind the MBB beam problem is to design for three-point bend test validation. In three-point bending the application of load through the fixtures to the specimen is accomplished with a constant thickness rigid loading head. The thinner the specimen, the higher the applied stresses. These two considerations can be accounted for with a model that describes the through-the-thickness load distribution as being uniformly applied on the edge that results from intersecting the plane of symmetry of the problem with the top beam face, as shown with a red line in Fig. 6.1. This edge is a straight line, of length t , where a uniform load, of intensity q , is applied. Let's also assume that the line is discretized with $n_i + 2$ regularly spaced nodes. Where n_i denotes the number of internal nodes. The constant distance from node to node is denoted by d .

To discretize the load into concentrated forces acting on the nodes, a statically equivalent system is not enough for a consistent finite element analysis. A statically equivalent system is a collection of forces whose resulting force and moment (about a point) are equal to the original load resultants. For example, applying a constant $P = qt/(n_i + 2)$ force over all the nodes is a statically equivalent system. However, it introduces spurious internal moments near the edges of the line.

By applying the method of sections on all the internal nodes this spurious moment can be quantified. When sectioning the line through the interior nodes, two types of free body diagrams (FBD) are obtained. First, an FBD where both nodes used to be in the interior and the forces applied on these FBD nodes is $P/2$. Second, an FBD where one node was at the end and the other interior, and the force applied on the end node is P while the force on the interior node is $P/2$. Formulating a moment balance on the second FBD results in a spurious $Pd/4$ moment. Formulating a moment balance on the first FBD results in an identity with no extra information.

The simplest consistent load applies forces P_e on the nodes at the ends, and a force P_i on the interior nodes. With this new load discretization, the moment balance of the second FBD results in the equation:

$$P_e \frac{d}{2} = \frac{P_i d}{2} \quad (6.1)$$

which can be simplified to

$$P_e = \frac{P_i}{2}. \quad (6.2)$$

The extra piece of information can be found from the global balance of forces

$$2P_e + n_i P_i = qt \quad (6.3)$$

which completes the system of 2 equations where P_i and P_e are unknowns. Solving this systems yields the interior and end nodal forces

$$P_i = \frac{qt}{1 + n_i} \quad (6.4)$$

and

$$P_e = \frac{qt}{2(1 + n_i)}. \quad (6.5)$$

If the line is only discretized with 2 nodes at the ends, then $n_i = 0$ and the end nodal forces reduce to

$$P_e = \frac{qt}{2} \quad (6.6)$$

which still holds as a consistent equivalent load. Eqs. (6.4) and (6.5) are used to model the load intake of a MBB 3D-beam with a generic thickness, t . However, to enable feature-based finite element modeling the principle of superposition, applicable in linear static stress analysis, is used to implement an equivalent load system of a downward

uniform load of value P_i throughout the full edge (including the end nodes) and an upward load of value $-P_e$ on the vertices of the edge. These loads are illustrated in Fig. 6.1 with yellow arrows applied on the red edge. This avoids implementing node sets for load application, since the loads can be applied to geometrical regions such as edges and vertices.

Figure 6.1 shows the symmetric part of the MBB 3D-beam problem. Symmetry conditions and boundary conditions, similar to the MBB 2D-beam problem, are applied uniformly throughout its thickness. As mentioned before, the edge of load application is shown in red while yellow arrows denote the two applied loads.

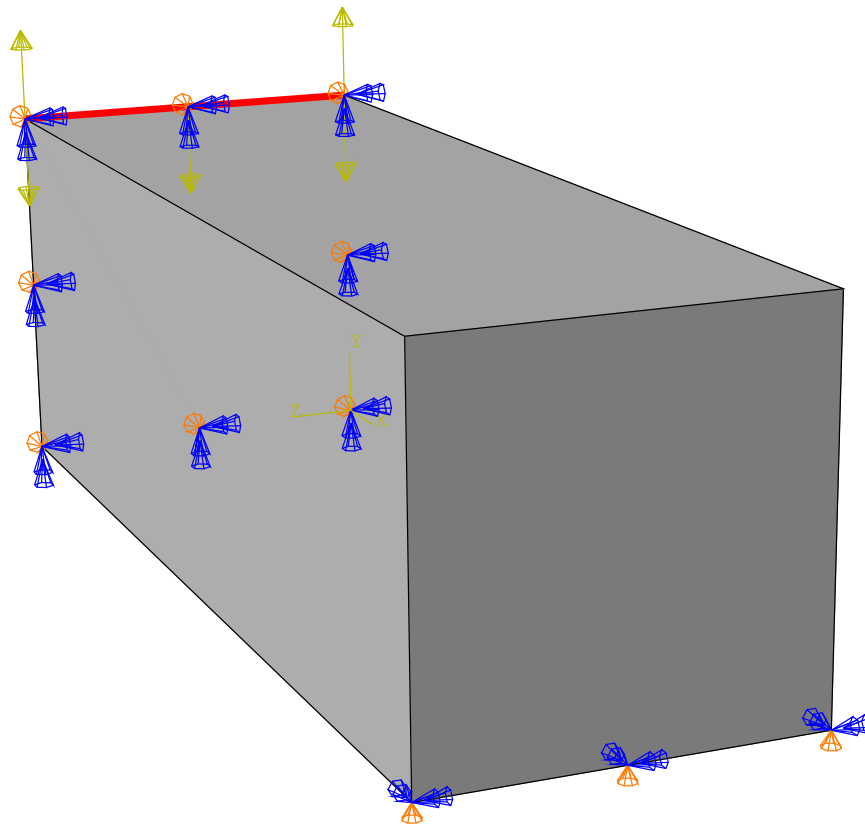


Figure 6.1: Global coordinate system for the MBB 3D ground structure

Moreover, the MBB 3D-beam is discretized with C3D8R cubic finite elements, with 30 elements along the width, b . The aspect ratio is set to

$$a/b = 6, \quad (6.7)$$

the penalization is $p = 3$ and the optimality criteria parameters are defined as

$$\zeta = 0.2, \beta = 0.5 \quad (6.8)$$

To reduce computational effort the continuation scheme is dropped in favor of a single step optimization using reciprocal interpolation. This simplified solution algorithm is illustrated in Fig. 6.2 with the aid of an XDSM diagram

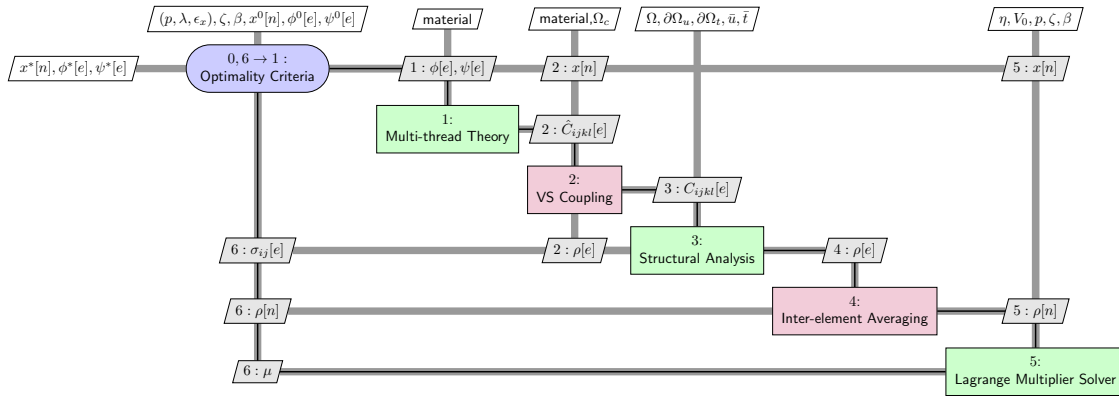


Figure 6.2: XDSM diagram of solution algorithm used for the MBB 3D problem

6.2 ISOTROPIC MBB

Using the isotropic material NISO1 of appendix A, a thin MBB 3D-beam is presented in Figures 6.3 and 6.4, using an isometric and sideview respectively. The thickness-to-width ratio of this beam is

$$t/b = 0.033, \quad (6.9)$$

so that the stress state approximates a plane-stress condition. When compared with the 2D isotropic topology of Chapter 4, the topology is an exact match. Moreover the

compliance of these beams differs in 3.95%. The 2D topology has a compliance of 25.85 as compared with the 3D compliance of 26.87.

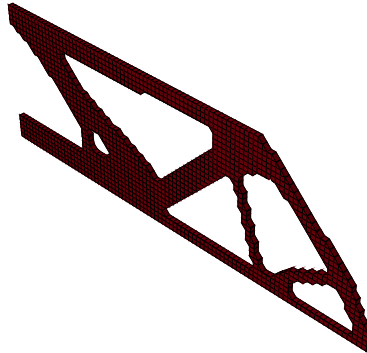


Figure 6.3: Isovlew of a $t = 0.033$ thin MBB made with isotropic material.

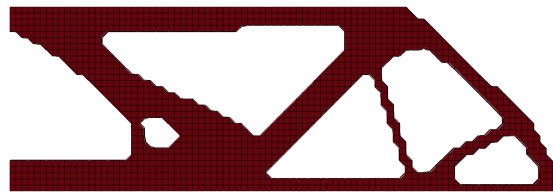


Figure 6.4: Sideview of a $t = 0.033$ thin MBB made with isotropic material.

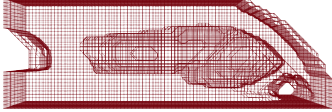
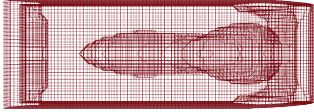
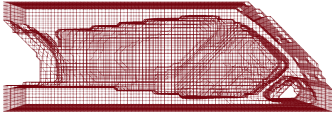
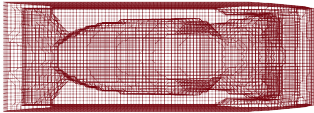
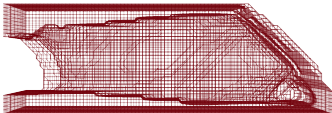
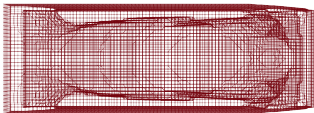
On the other end, a thick isotropic MBB with a thickness-to-width ratio,

$$t/b = 1, \tag{6.10}$$

is shown in Table 6.1 for different volume fractions. Starting with $\eta = 0.8$ until $\eta = 0.5$, the table shows the top and side view of the wireframes for the different optimal topologies. The intent of this table is to show the evolution of the internal cavity until the topology becomes a boxed beam with variable-thickness walls for $\eta = 0.5$.

Moreover, the volume fraction sweep has been extended until values of $\eta = 0.12$ to investigate the topologies that appear for stringently low volume fraction targets. Figure 6.5 shows the extended optimality curve for this volume fraction sweep from $\eta = 0.8$ until $\eta = 0.12$. The extended optimality is defined as U^*_η/U_0 and measures the benefit of using

Table 6.1: Volume fraction, η , evolution to understand convergence into a boxed beam in $\eta = 0.5$

η	side view	top view
0.8		
0.6		
0.5		

topology optimization, as compared to just reducing the thickness of the MBB 3D-beam. An extended optimality value of 1 means that the structure has become more flexible in the same proportion as the reduction of volume. For example, an $\eta = 0.5$ with a unit extended optimality results in an optimized topology twice as compliant. Extended optimality values smaller than 1 are expected.

Upon visual inspection of Figure 6.5, all topologies with $\eta > 0.15$ are below 1. To understand why topologies with $\eta < 0.15$ have a larger than 1 extended optimality, the deformed shapes of the topologies are also included in Fig. 6.5 along with a contour plot of the stress component along the thickness of the beam σ_{zz} . The deformed shape for $\eta = 0.12$ reveals that, because of the stringent volume reduction, the strut that prevents the side walls

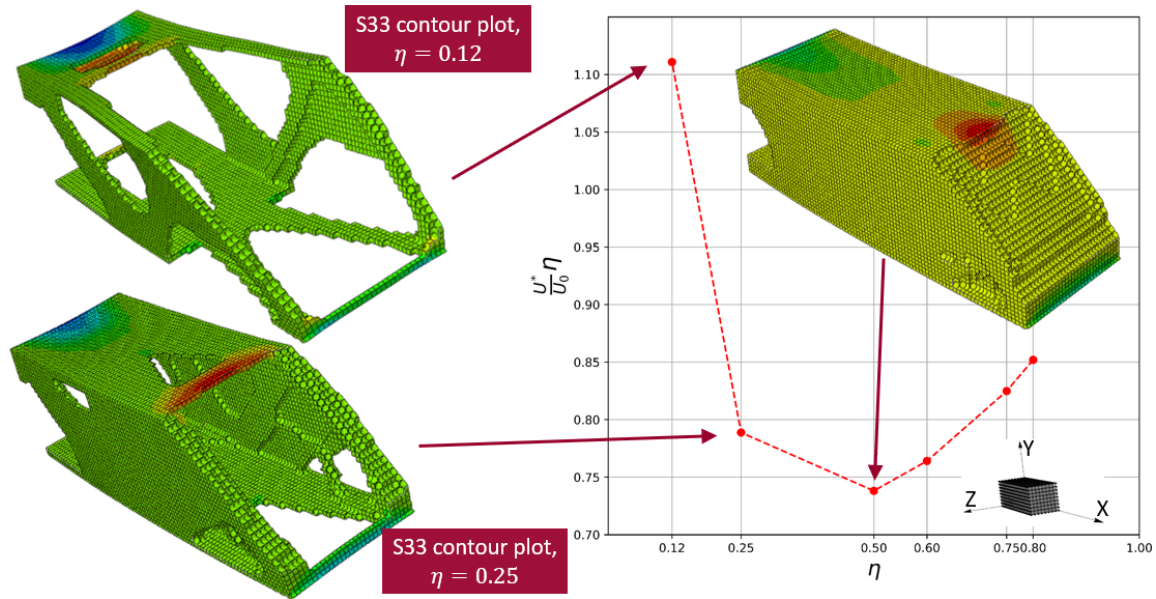


Figure 6.5: Extended optimality curve for a thick $t = 1$ MBB as a function of volume fraction. Contour plots of the σ_{33} component are shown on top of the deformed mesh for select points

from opening up has been removed and thus a large deflection of these appears. Moreover, the deformed shape for $\eta = 0.12$ shows that the top beam that connects the side walls and that absorbs the applied load has an I-shaped cross section. When uniformly loading a beam along its axis, an I cross section where the top and bottom flanges transfer most of the bending load is what is intuitively expected as an optimal bending shape. Finally, note in Fig. 6.5 that the boxed beam topology of $\eta = 0.5$ appears to be a global minimum of the extended optimality curve. A gradient-based optimization study, that uses the extended optimality metric as the objective function and includes η as a design variable may shed further light into this.

6.3 ORTHOTROPIC MBB

Using the thread plane model, with all in-plane stiffness parameters set to zero, thick MBB 3D-beams with a thickness-to-width ratio of

$$t/b = 1 \quad (6.11)$$

Table 6.2: material stiffness and optimized compliance for different degrees of orthotropy due to a layer-by-layer manufacturing process

stiffness	isotropic	QIZ ($\phi = 0, \psi = 0$)	QIY ($\phi = 0, \psi = \pi/2$)
C_{11}	0.4996	0.4422	0.4422
C_{22}	0.4996	0.4422	0.0761
C_{33}	0.4996	0.0761	0.4422
U^*	57.07	59.84	85.64

are compared when the thread plane is aligned perpendicular to the Z axis and the Y axis of Fig. 6.6. The aim of such an exercise is to explore the difference in the optimized topologies when accounting for the inherent anisotropy of a layer-by-layer manufacturing process, as compared to the isotropic idealization.

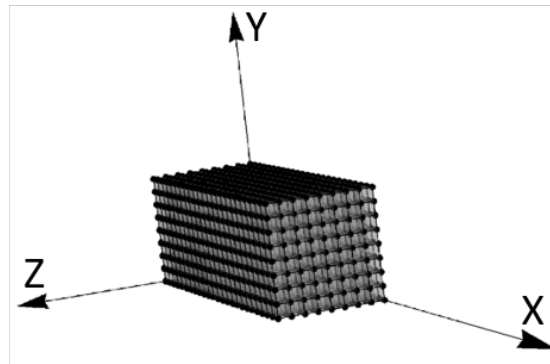
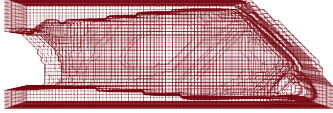
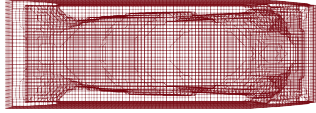
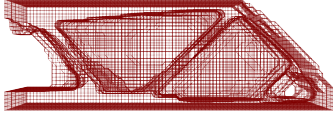
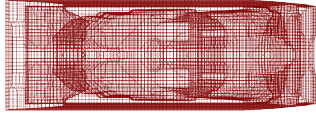
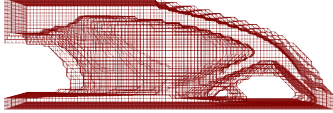
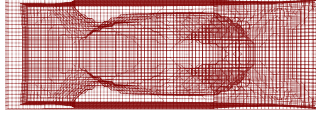


Figure 6.6: Global coordinate system for the MBB 3D-beam ground structure

Table 6.2 summarizes the assumed longitudinal stiffnesses for the idealized isotropic and the two build directions. When the build direction is oriented along the Z axis, it is assumed that the material is isotropic in the XY plane and has a smaller stiffness in the Z direction (about 1/5 weaker). Mutatis mutandis for the QIY build. The last row of Table 6.2 reports the optimized compliance, measured via the strain energy U , when performing a topology optimization using these materials for a volume fraction $\eta = 0.5$.

Moreover, Table 6.3 shows the side and top views of the wireframes of these topologies. Note that contrary to the isotropic results of Section 5.2, printing a thick MBB 3D-beam along the Z or Y axis results in the need for internal walls due to the layered nature of the

Table 6.3: Side and top views of the optimal topology wireframes showing different internal cavities for different degrees of orthotropy

degree of anisotropy	side view	top view
QI isotropic		
QIZ		
QIY		

part.

6.4 CURVILINEAR FIBER FORMAT MBB

A curvilinear fiber format MBB in 3D space will result in a spatially reinforced topology where the fiber orientation can change from point to point with either an in-plane or out-of-plane orientation, or a combination of both. However, to compare against the curvilinear fiber format MBB 2D-beam of Chapter 4, a thin beam of thickness-to-width ratio

$$t/b = 0.033 \quad (6.12)$$

is optimized. Both the in-plane and out-of-plane-rotation angles ϕ and ψ are selected as design variables, although due to the small thickness-to-width ratio the out-of-plane rotation is expected to be negligible. Figure 6.7 shows an isoview of the optimized solid topology, while Fig. 6.8 shows the sideview of the wireframe of the topology where the

fiber orientation angle distribution has been projected on top. The topology of the thin curvilinear fiber format MBB 3D-beam results in the same large-scale members as seen in the curvilinear fiber format MBB 2D-beam of Fig. 5.8. Although, the smaller members show a different layout. Moreover, the performance of the MBB 3D-beam of 35.04 non-negligibly differs from the performance of the MBB 2D-beam of 45.08.

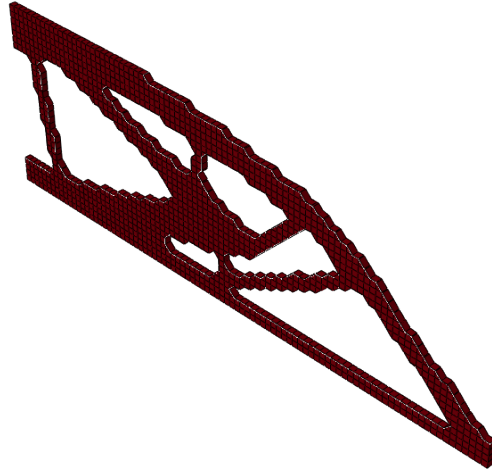


Figure 6.7: Isoview of a $t = 0.033$ thin MBB with curvilinear fiber reinforcement.

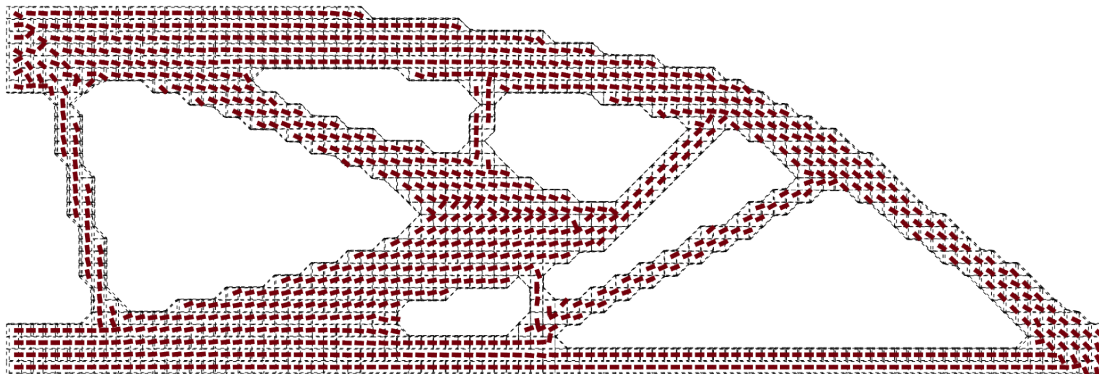
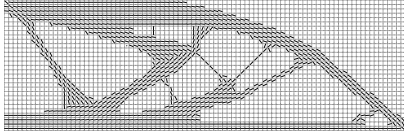
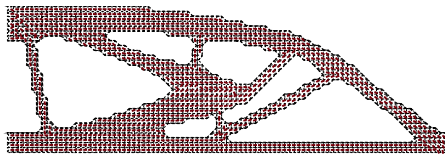
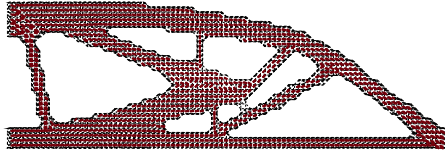


Figure 6.8: Sideview of a $t = 0.033$ thin MBB with curvilinear fiber reinforcement shown as an element-centered fiber orientation angle distribution

A summary of the comparison between the 2D and 3D curvilinear fiber format MBB results is shown in Table 6.4. Moreover, Table 6.4 shows an additional row of a

Table 6.4: Side and top views of the optimal topology wireframes showing different internal cavities for different degrees of orthotropy

dims.	t/b	U^*t/b	sideview
2D	1	45.08	
3D	0.033	35.04	
3D	0.1	34.97	

curvilinear fiber format MBB 3D-beam, with a thickness-to-width ratio $t/b = 0.1$, to study the sensitivity of the topology due to a small increase in thickness. To compare the performance of these topologies, the optimized strain energy U^* scaled with their respective thickness-to-width ratio, t/b , is also tabulated.

As a demonstration of capability of the 3D framework presented in Chapter 3, a curvilinear fiber format MBB 3D-beam with a thickness-to-width ratio of

$$t/b = 1 \quad (6.13)$$

is lightweighted for $\eta = 0.25$. Tallying both nodal densities and element-centered fiber orientation angles, this problem optimized 249,452 design variables. Figure 6.9 shows an isoview with a solid representation of the optimized topology. Figure 6.9 shows a structure that can be described as being composed of four types of structural members. First, a solid base where the other three members lay supports most of the compression due to bending. As seen in Fig. 6.10 and Fig. 6.12, this solid base has straight fibers aligned along

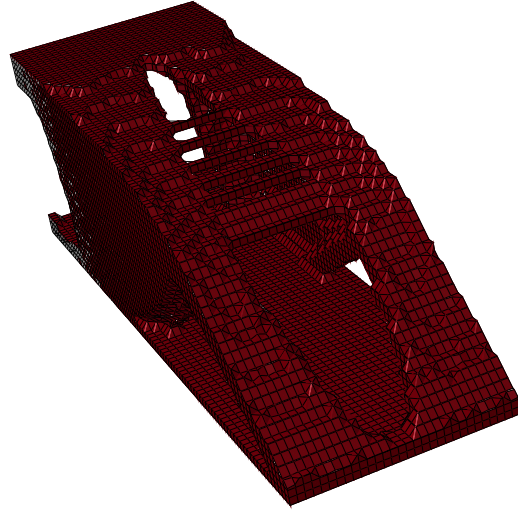


Figure 6.9: Isovview of a curvilinear fiber format thick MBB 3D-beam for $\eta = 0.25$

the length of the beam. Second, two variable-thickness sidewalls stand on the solid base. The wireframe isovview shown in Fig. 6.11 along with the wireframe sideview of Fig. 6.10 clarify that these sidewalls are reinforced with fibers oriented within the XY plane.

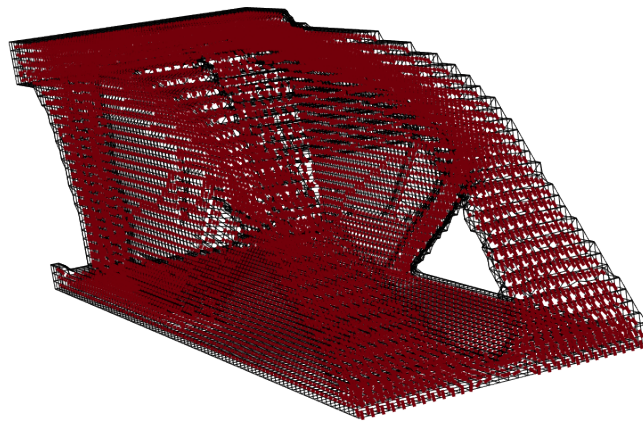


Figure 6.10: Isovview of a curvilinear fiber format thick MBB 3D wireframe, for $\eta = 0.25$, and fiber orientation segment distribution.

Third, curved arches rest on top of the side walls and connect with the solid plate towards the end. The wireframe rearview shown in Fig. 6.12 and wireframe isovview in Fig. 6.10 illustrate the curvilinear fibers aligned with these arches.

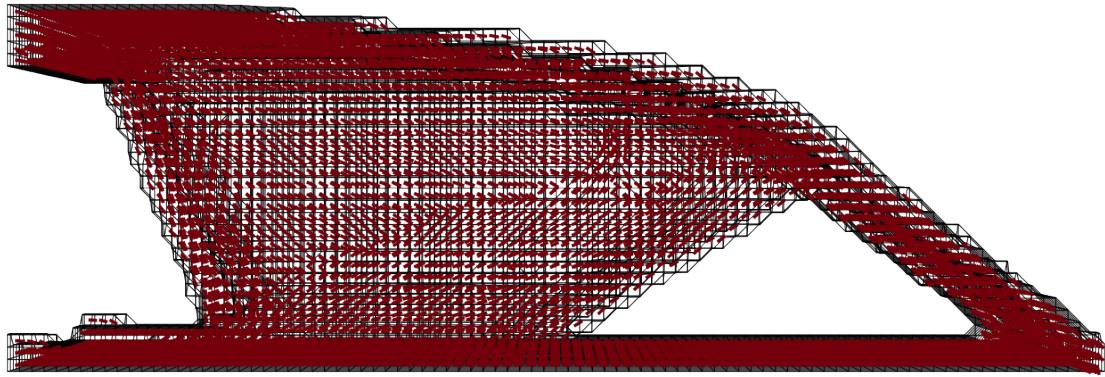


Figure 6.11: Sideview of a curvilinear fiber format thick MBB 3D wireframe, for $\eta = 0.25$, and fiber orientation segment distribution.

Finally, several thin struts connect the arches together to prevent the sidewalls from opening up. The wireframe rearview shown in Fig. 6.12 illustrates these struts with their horizontal reinforced fibers.

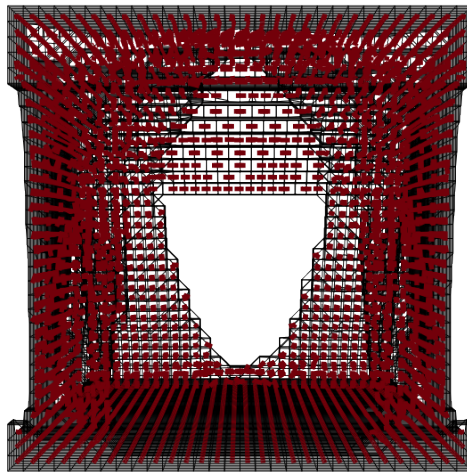


Figure 6.12: Rearview of a curvilinear fiber format thick MBB 3D wireframe, for $\eta = 0.25$, and fiber orientation segment distribution.

Overall, this curvilinear fiber format thick MBB 3D-beam demonstrates the breadth of structural members along with all the possible fiber orientation angles that can be generated using this framework. Although the topology is 75% lighter, the simultaneous design of topology and fiber orientation yielded a structure that is only 16.5% more flexible.

Resulting in an extended optimality of 0.29.

CHAPTER 7

CONCLUDING REMARKS

This work lies in the crossroads of two research areas. On the one hand, as reviewed in Chapter 2, the optimization algorithms proposed in this work contribute to the literature of structural and multidisciplinary optimization. As noted by Haftka et al. (2019), in an editorial to the structural and multidisciplinary optimization (SMO) journal, "almost all the papers in SMO are about computational algorithms". On the other, this work contributes to the mission of the McNair Center for Aerospace Innovation and Research to push the boundary of discovery for additive manufacturing in general and composites manufacturing in particular. Sec. 7.1 lists the contributions of this work based on its significance to each of these audiences. Because this work presents a new computational design framework with many research avenues, many compromises have been made to narrow its scope. These compromises, along with the limitations they present, are listed in Sec. 7.2. Finally, Sec. 7.3 provides a list of recommendations on how to carry on future work within this framework.

7.1 SIGNIFICANT CONTRIBUTIONS

This work lies in the crossroads of two research areas. On the one hand, it contributes new optimization algorithms to the literature of structural and multidisciplinary optimization. On the other, this work contributes to the mission of the McNair Center for Aerospace Innovation and Research (McNAIR). Section 7.1.1 lists the contributions of this work to the former, while Sec. 7.1.2 lists its contributions to the latter.

7.1.1 STRUCTURAL AND MULTIDISCIPLINARY OPTIMIZATION

A new computational framework for 3D design of fiber-reinforced composites has been presented. This framework has been shown to be consistent with plane-stress, or 2D, approximations for various degrees of anisotropy. The framework proposed a new topology optimization algorithm, which combines the benefits of linear and reciprocal interpolation via a continuation scheme. This continuation scheme was successfully applied to MBB 2D-beam problems.

Besides the computational design framework, a new post-processing algorithm that smooths node-centered 2D topologies into densely rasterized images for STL file conversion was successfully used to 3D print an optimized node-centered 2D topology. When combined with the computational design framework, this post-processing algorithm contributes in the development of a function-to-print capability. The ability of going from functional specifications to a printed part is needed for experimental validation of the optimization algorithms. Note that the MBB beam problems, numerically studied in this work, may be validated with three point bend tests.

By applying the computational design framework to MBB 3D-beam problems with varying degrees of anisotropy, this work has contributed in the exploration of the design latitude provided by topology optimization. Variable-thickness box beam and I-beam structures have been generated with this framework.

This work not only explores the design space unlocked by 3D topology optimization, but also contributes with further numerical evidence to the promise of unprecedented performance benefits when optimizing both the shape and material properties. In particular, a curvilinear fiber format MBB 3D-beam with 249,451 design variables describing both density and fiber orientation angles has been lightweighted to 25% its original weight, yet has only increased in flexibility by 16.5%.

7.1.2 McNAIR

The overall endeavor at the McNAIR Center is to push the boundary of discovery for additive manufacturing in general and for composites manufacturing, predominately Automated Fiber Placement (AFP), in particular. In the context of AFP, this work precedes path planning studies for AFP (Rousseau et al. 2018) where finding the optimal tool path for laying fibers along the prescribed fiber orientation angle distribution is sought. One of the principal conditions in path planning is the minimization of AFP defects (Harik et al. 2018) and the effect they can have on the integrity of the structure (Wehbe et al. 2019). Although this work is situated in the conceptual stage of the design process, the toolkit specifications presented in Chapter 4 provide a blueprint that can latter be integrated with more efficient 2D design processes (Albazzan et al. 2019) that incorporate AFP manufacturing considerations. Thus, laying the groundwork for future integration of manufacturing considerations early in the conceptual design stage. Moreover, the MARIA libraries provide programmatic interfaces that can complement research projects such as integrated design and manufacturing analysis for AFP (Noevere et al. 2019), automation of process planning (Halbritter et al. 2019), heat optimization (Xia et al. 2018), automated inspection (Sacco et al. 2019) and rapid assessment tools (Bahamonde et al. 2018) aimed at providing a better integral lay-up quality.

In sum, this work actively participates in the advancement of additive manufacturing and AFP by providing computational tools that can be reused in other design processes and harnessed to tailor both shape and material properties to the functionality required. Thus, it supports the overall McNAIR goal to thrust advanced manufacturing innovation and research.

7.2 COMPROMISES AND LIMITATIONS

Although this work demonstrated that centering densities at the nodes solves checkerboarding instabilities, the length-scale control problem has not been addressed.

As seen in Sec. 5.2, arbitrarily refining the density mesh results in structural members of arbitrarily small length scale. The length scale control problem also relates to fiber steering during manufacturing. There is no design control on the radius of curvature of curvilinear uni-axial members and fiber paths. In general, this work formulates no manufacturing considerations in the design problem. For example, Fig. 7.1 shows a smooth MBB 2D-beam with a zero degree fiber path using the Eiger printing software from Markforged.

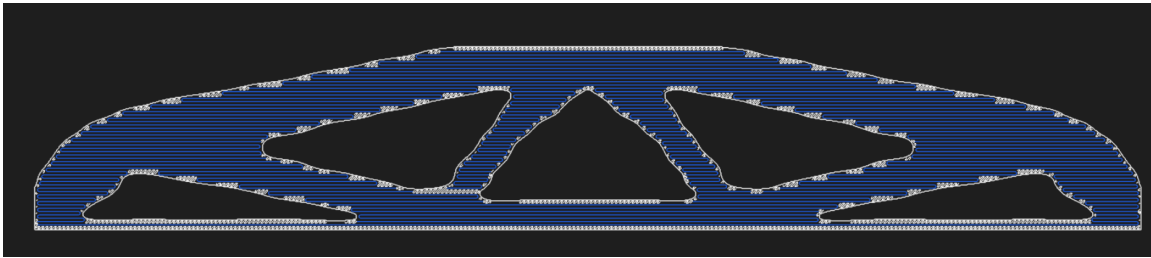


Figure 7.1: MBB 2D-beam boundary with 0 degree fiber path and watertight boundary finish

Upon inspection of Fig. 7.1, the path planning software predicts that a single filament can barely squeeze through the thin bottom horizontal bars. Because the part boundary is finished with nylon material shown in white in Fig. 7.1 to provide a watertight part, filaments deposited with this hardware may not be able to reinforce certain thin members. Such manufacturing considerations limit the realizability of certain solutions generated by this design framework.

Besides manufacturability, the functionality of this computational design framework is limited to stiffness optimization. To scale the framework up to 249,451 design variables, this work used non-gradient heuristic design rules. These rules optimize stiffness, and only for uni-axial members with a curvilinear fiber format strength improves as a by-product, but cannot be generalized to other design criteria such as strength or buckling. Moreover, the design rule based on stress trajectories appears to be biased with respect to the initial fiber orientation angle distribution. Thus, starting with different fiber orientation angle distributions leads to different optimized topologies. A continuation scheme or any other solution to the bias of stress trajectories has not been provided.

7.3 RECOMMENDATIONS

The general recommendation is to continue the study of this new framework with further numerical and experimental studies such as to increase confidence on the framework and generate benchmarks against which the framework capabilities can be improved. In particular, based on the previously outlined capabilities and limitations of the framework, the remainder of this section recommends the following projects for future research.

First, an experimental validation of the framework using MBB 2D-beam topologies is recommended. The function-to-print workflow is already available and the MBB problem almost directly translates into a three point bend test. However, caution in selecting topologies with the right deformation modes is recommended. For instance, the topologies optimized in Sec. 5.3 for a straight fiber format may prove difficult to validate. Because these topologies couple shear with extensional deformation, the displacement of the mid-section will not serve as a valid metric for compliance since the supports will dissipate most of this lateral deformation through friction.

Second, a project to replace stress trajectories with non-interactive failure criteria is recommended. The MBB problems subject the structure to in-plane bending where the top fibers are subject to compression and the bottom fibers to tension. Somewhere in between the stress changes from tension to compression, which is where the stress trajectories rule abruptly changes the fiber orientation angle. This results in sub-optimal solutions which can be addressed by using non-interactive failure criteria. Instead of orienting the fiber along the maximum principal stress, the non-interactive failure criterion can be used as a function to be minimized on every finite element where the orientation of the fibers is the design variable. Not only will this project provide insight into the shortcomings of using stress trajectories alongside topology optimization, but also serves as a stepping stone into strength-focused research projects which may require use of gradient-based optimization.

Third, further exploration of closed-section topologies is recommended. The variable-thickness box-type topologies of Sec. 6.2 have been shown to minimize the

extended optimality metric. Future research should explore if using variable orientation quasi-isotropic thread planes results into boxed beams as well. This project can add further credibility into using topology optimization as a tool for monocoque shell conceptual design.

Finally, a project to transition the computational design framework to use gradient-based optimization is recommended. In particular, the use of the adjoint sensitivity analysis procedure as formulated by (Cacuci 2003) is recommended to maintain the scalability of the framework when using a large number of design variables. Unlike the previously recommended research projects, which require a limited modification if any of the framework, this project involves substantial work. The finite element analysis code must be able to compute adjoint sensitivities of the responses with respect to element-centered stiffnesses. It is also recommended to use the chain rule along with the dependency trees introduced in Chapter 3 to compute the sensitivities of the objectives with respect to the design variables.

BIBLIOGRAPHY

- Abdalla, M. M., Setoodeh, S., & Gürdal, Z. (2007). Design of variable stiffness composite panels for maximum fundamental frequency using lamination parameters. *Composite Structures*, 81(2), 283–291. doi:10.1016/j.compstruct.2006.08.018
- Abdalla, M. & Gürdal, Z. (2002). Structural Design Using Optimality Based Cellular Automata. American Institute of Aeronautics and Astronautics. doi:10.2514/6.2002-1676
- Albazzan, M. A., Harik, R., Tatting, B. F., & Gürdal, Z. (2019). Efficient design optimization of nonconventional laminated composites using lamination parameters: A state of the art. *Composite Structures*, 209, 362–374. doi:10.1016/j.compstruct.2018.10.095
- Allaire, G. & Francfort, G. A. (1993). A Numerical Algorithm for Topology and Shape Optimization. In M. P. Bendsøe & C. A. M. Soares (Eds.), *Topology Design of Structures* (pp. 239–248). NATO ASI Series. Dordrecht: Springer Netherlands. doi:10.1007/978-94-011-1804-0_16
- Allaire, G. & Kohn, R. V. (1993). Topology Optimization and Optimal Shape Design Using Homogenization. In M. P. Bendsøe & C. A. M. Soares (Eds.), *Topology Design of Structures* (pp. 207–218). NATO ASI Series. Dordrecht: Springer Netherlands. doi:10.1007/978-94-011-1804-0_14
- Andreassen, E., Clausen, A., Schevenels, M., Lazarov, B. S., & Sigmund, O. (2011). Efficient topology optimization in MATLAB using 88 lines of code. *Structural and Multidisciplinary Optimization*, 43(1), 1–16. doi:10.1007/s00158-010-0594-7

- Bahamonde, L., Albazzan, M., Chevalier, P., Gürdal, Z., Tatting, B., Tatting, B., & Harik, R. (2018). Rapid Tools for an AFP Manufacturing Defects Assessment Framework. In *SAMPE 2018 Conference & Exhibition*. Long Beach, CA.
- Bendsøe, M. P. & Sigmund, O. (2011). *Topology optimization: Theory, methods, and applications* (Second edition, corrected printing). Engineering online library. OCLC: 711862335. Heidelberg, Berlin: Springer.
- Bendsøe, M. P., Díaz, A., & Kikuchi, N. (1993). Topology and Generalized Layout Optimization of Elastic Structures. In M. P. Bendsøe & C. A. M. Soares (Eds.), *Topology Design of Structures* (pp. 159–205). NATO ASI Series. Dordrecht: Springer Netherlands. doi:10.1007/978-94-011-1804-0_13
- Bendsøe, M. P. & Kikuchi, N. (1988). Generating optimal topologies in structural design using a homogenization method. *Computer Methods in Applied Mechanics and Engineering*, 71(2), 197–224. doi:10.1016/0045-7825(88)90086-2
- Blom, A. W., Stickler, P. B., & Gürdal, Z. (2010). Optimization of a composite cylinder under bending by tailoring stiffness properties in circumferential direction. *Composites Part B: Engineering*, 41(2), 157–165. doi:10.1016/j.compositesb.2009.10.004
- Blom, A. W., Tatting, B. F., Hol, J. M., & Gürdal, Z. (2009). Fiber path definitions for elastically tailored conical shells. *Composites Part B: Engineering*, 40(1), 77–84. doi:10.1016/j.compositesb.2008.03.011
- Bourdin, B. (2001). Filters in topology optimization. *International Journal for Numerical Methods in Engineering*, 50(9), 2143–2158. doi:10.1002/nme.116
- Brandmaier, H. E. (1970). Optimum Filament Orientation Criteria. *Journal of Composite Materials*, 4(3), 422–425. doi:10.1177/002199837000400314
- Brent, R. P. (2002). *Algorithms for minimization without derivatives*. Mineola, N.Y.: Dover Publications.

- Brooks, F. P. (1975). *The mythical man-month: Essays on software engineering*. Reading, Mass: Addison-Wesley Pub. Co.
- Buhl, T., Pedersen, C., & Sigmund, O. (2000). Stiffness design of geometrically nonlinear structures using topology optimization. *Structural and Multidisciplinary Optimization*, 19(2), 93–104. doi:10.1007/s001580050089
- Cacuci, D. G. (2003). *Sensitivity and uncertainty analysis*. Boca Raton: Chapman & Hall/CRC Press.
- Dassault Systemes. (2017). Abaqus/CAE. Providence, Rhode Island: Dassault Systemes. Retrieved February 21, 2019, from <https://www.3ds.com/fileadmin/PRODUCTS/SIMULIA/PDF/datasheets/simulia-abaqus-cae-datasheet.pdf>
- Díaz, A. & Sigmund, O. (1995). Checkerboard patterns in layout optimization. *Structural optimization*, 10(1), 40–45. doi:10.1007/BF01743693
- Gomes, V. S., Lopes, C. S., Pires, F. F. A., Gürdal, Z., & Camanho, P. P. (2014). Fibre steering for shear-loaded composite panels with cutouts. *Journal of Composite Materials*, 48(16), 1917–1926. doi:10.1177/0021998313492356
- Group, T. H. (1997). Hierarchical Data Format, version 5. Retrieved February 21, 2019, from <http://www.hdfgroup.org/HDF5/>
- Gürdal, Z. & Olmedo, R. (1993). In-plane response of laminates with spatially varying fiber orientations - Variable stiffness concept. *AIAA Journal*, 31(4), 751–758. doi:10.2514/3.11613
- Haftka, R. T., Zhou, M., & Queipo, N. V. (2019). Replication of results. *Structural and Multidisciplinary Optimization*, s00158–019–02298–4. doi:10.1007/s00158-019-02298-4
- Halbritter, J., Harik, R., Saïdy, C., Noevere, A., & Grimsley, B. (2019). Automation of AFP Process Planning Functions: Importance and Ranking. In *SAMPE 2019 Conference & Exhibition*. Charlotte, NC: SAMPE. doi:10.33599/nasampe/s.19.1592

- Hammer, V., Bendsøe, M., Lipton, R., & Pedersen, P. (1997). Parametrization in laminate design for optimal compliance. *International Journal of Solids and Structures*, 34(4), 415–434. doi:10.1016/S0020-7683(96)00023-6
- Harik, R., Saidy, C., Williams, S., Gürdal, Z., & Grimsley, B. (2018). Automated fiber placement defect identity cards: Cause, anticipation, existence, significance, and progression. In *SAMPE 2018 Conference & Exhibition*. Long Beach, CA.
- Hyer, M. W. & Charette, R. F. (1991). Use of curvilinear fiber format in composite structure design. *AIAA Journal*, 29(6), 1011–1015. doi:10.2514/3.10697
- Ijsselmuiden, S. T., Abdalla, M. M., & Gürdal, Z. (2008). Implementation of Strength-Based Failure Criteria in the Lamination Parameter Design Space. *AIAA Journal*, 46(7), 1826–1834. doi:10.2514/1.35565
- Ijsselmuiden, S. T. (2011). *Optimal Design of Variable Stiffness Composite Structures Using Lamination Parameters* (Doctoral dissertation, TU Delft).
- Jog, C. S. & Haber, R. B. (1996). Stability of finite element models for distributed-parameter optimization and topology design. *Computer Methods in Applied Mechanics and Engineering*, 130(3-4), 203–226. doi:10.1016/0045-7825(95)00928-0
- Jones, R. M. (1975). *Mechanics of composite materials*. OCLC: 220272769. Bristol: Taylor & Francis.
- Kang, Z. & Wang, Y. (2012). A nodal variable method of structural topology optimization based on Shepard interpolant: NODAL VARIABLE TOPOLOGY OPTIMIZATION BASED ON SHEPARD INTERPOLANT. *International Journal for Numerical Methods in Engineering*, 90(3), 329–342. doi:10.1002/nme.3321
- Kočvara, M., Stingl, M., & Zowe, J. (2008). Free material optimization: Recent progress†. *Optimization*, 57(1), 79–100. doi:10.1080/02331930701778908

- Kregers, A. F. & Melbardis, Y. G. (1978). Determination of the deformability of three-dimensionally reinforced composites by the stiffness averaging method. *Polymer Mechanics*, 14(1), 1–5. doi:10.1007/BF00859550
- Lambe, A. B. & Martins, J. R. R. A. (2012). Extensions to the design structure matrix for the description of multidisciplinary design, analysis, and optimization processes. *Structural and Multidisciplinary Optimization*, 46(2), 273–284. doi:10.1007/s00158-012-0763-y
- Michell, A. G. M. (1904). The limits of economy of material in frame-structures. *The London, Edinburgh, and Dublin Philosophical Magazine and Journal of Science*, 8(47), 589–597. doi:10.1080/14786440409463229
- Miki, M. & Sugiyamat, Y. (1993). Optimum Design of Laminated Composite Plates Using Lamination Parameters. *AIAA Journal*, 31(5), 921–922. doi:10.2514/3.49033
- Nemeth, M. P. (2011). *An In-Depth Tutorial on Constitutive Equations for Elastic Anisotropic Materials* (tech. rep. No. NASA/TM-2011-217314). NASA. Retrieved January 1, 2016, from <https://ntrs.nasa.gov/search.jsp?R=20110023650>
- Nocedal, J. & Wright, S. J. (2006). *Numerical Optimization* (2nd ed). Springer series in operations research. OCLC: ocm68629100. New York: Springer.
- Noevere, A., Collier, C., & Harik, R. (2019). Integrated Design and Manufacturing Analysis for Automated Fiber Placement Structures. In *SAMPE 2019 Conference & Exhibition*. Charlotte, NC: SAMPE. doi:10.33599/nasampe/s.19.1500
- Pedersen, P. (1989). On optimal orientation of orthotropic materials. *Structural Optimization*, 1(2), 101–106. doi:10.1007/BF01637666
- Peeters, D., van Baalen, D., & Abdallah, M. (2015). Combining topology and lamination parameter optimisation. *Structural and Multidisciplinary Optimization*, 52(1), 105–120. doi:10.1007/s00158-014-1223-7

- Petersson, J. & Sigmund, O. (1998). Slope constrained topology optimization. *International Journal for Numerical Methods in Engineering*, 41(8), 1417–1434. doi:10.1002/(SICI)1097-0207(19980430)41:8<1417::AID-NME344>3.0.CO;2-N
- Rahmatalla, S. & Swan, C. (2004). A Q4/Q4 continuum structural topology optimization implementation. *Structural and Multidisciplinary Optimization*, 27(1-2), 130–135. doi:10.1007/s00158-003-0365-9
- Raju, G., White, S., Wu, Z., & Weaver, P. (2015). Optimal Postbuckling Design of Variable Angle Tow Composites using Lamination Parameters. In *56th AIAA/ASCE/AHS/ASC Structures, Structural Dynamics, and Materials Conference*. Kissimmee, Florida: American Institute of Aeronautics and Astronautics. doi:10.2514/6.2015-0451
- Rojas-Labanda, S. & Stolpe, M. (2015). Automatic penalty continuation in structural topology optimization. *Structural and Multidisciplinary Optimization*, 52(6), 1205–1221. doi:10.1007/s00158-015-1277-1
- Rousseau, G., Wehbe, R., Halbritter, J., & Harik, R. (2018). Automated Fiber Placement Path Planning: A state-of-the-art review. *Computer-Aided Design and Applications*, 16(2), 172–203. doi:10.14733/cadaps.2019.172-203
- Rozvany, G. I. N. (Ed.). (1991). *Optimization of Large Structural Systems*. OCLC: 886503841. Springer Verlag.
- Sabido, A., Bahamonde, L., Harik, R., & van Tooren, M. J. (2017). Maturity assessment of the laminate variable stiffness design process. *Composite Structures*, 160, 804–812. doi:10.1016/j.compstruct.2016.10.081
- Sacco, C., Radwan, A. B., Beatty, T., & Harik, R. (2019). Machine Learning Based AFP Inspection: A Tool for Characterization and Integration. In *SAMPE 2019 Conference & Exhibition*. Charlotte, NC: SAMPE. doi:10.33599/nasampe/s.19.1594
- Setoodeh, S., Blom, A., Abdalla, M., & Gürdal, Z. (2006). Generating Curvilinear Fiber Paths from Lamination Parameters Distribution. In *47th AIAA/ASME/ASCE/AHS/ASC Structures, Structural Dynamics, and*

Materials Conference; 14th AIAA/ASME/AHS Adaptive Structures Conference; 7th. Newport, Rhode Island: American Institute of Aeronautics and Astronautics. doi:10.2514/6.2006-1875

Setoodeh, S., Abdalla, M., & Gürdal, Z. (2005). Combined topology and fiber path design of composite layers using cellular automata. *Structural and Multidisciplinary Optimization*, 30(6), 413–421. doi:10.1007/s00158-005-0528-y

Sigmund, O. & Petersson, J. (1998). Numerical instabilities in topology optimization: A survey on procedures dealing with checkerboards, mesh-dependencies and local minima. *Structural Optimization*, 16(1), 68–75. doi:10.1007/BF01214002

Sigmund, O. (1994). *Design of Material Structures using Topology Optimization* (Doctoral dissertation). Retrieved from https://www.researchgate.net/publication/261173987_Design_of_Material_Structures_Using_Topology_Optimization

Sigmund, O., Aage, N., & Andreassen, E. (2016). On the (non-)optimality of Michell structures. *Structural and Multidisciplinary Optimization*, 54(2), 361–373. doi:10.1007/s00158-016-1420-7

Sigmund, O. & Maute, K. (2013). Topology optimization approaches: A comparative review. *Structural and Multidisciplinary Optimization*, 48(6), 1031–1055. doi:10.1007/s00158-013-0978-6

Sokół, T. (2011). A 99 line code for discretized Michell truss optimization written in Mathematica. *Structural and Multidisciplinary Optimization*, 43(2), 181–190. doi:10.1007/s00158-010-0557-z

Stanford, B. K., Jutte, C. V., & Chauncey Wu, K. (2014). Aeroelastic benefits of tow steering for composite plates. *Composite Structures*, 118, 416–422. doi:10.1016/j.compstruct.2014.08.007

Stolpe, M. & Svanberg, K. (2001). On the trajectories of penalization methods for topology optimization. *Structural and Multidisciplinary Optimization*, 21(2), 128–139. doi:10.1007/s001580050177

- Svanberg, K. (1987). The method of moving asymptotes—a new method for structural optimization. *International Journal for Numerical Methods in Engineering*, 24(2), 359–373. doi:10.1002/nme.1620240207
- Tatting, B. F. (1998). *Analysis and Design of Variable Stiffness Composite Cylinders* (Doctoral dissertation).
- Ting, T. C. T. (1987). INVARIANTS OF ANISOTROPIC ELASTIC CONSTANTS. *The Quarterly Journal of Mechanics and Applied Mathematics*, 40(3), 431–448. doi:10.1093/qjmam/40.3.431
- Watada, R., Ohsaki, M., & Kanno, Y. (2011). Non-uniqueness and symmetry of optimal topology of a shell for minimum compliance. *Structural and Multidisciplinary Optimization*, 43(4), 459–471. doi:10.1007/s00158-010-0587-6
- Wehbe, R., Tatting, B., Gürdal, Z., & Harik, R. (2019). Fiber Tow Deformations During Layup of Steered Paths Using Automated Fiber Placement Process. In *SAMPE 2019 Conference & Exhibition*. SAMPE. doi:10.33599/nasampe/s.19.1591
- Wu, K. C., Stanford, B. K., Hrinda, G. A., Wang, Z., Martin, R. A., & Kim, H. A. (2013). Structural Assessment of Advanced Tow-Steered Shells. In *54th AIAA/ASME/ASCE/AHS/ASC Structures, Structural Dynamics, and Materials Conference*. Boston, Massachusetts: American Institute of Aeronautics and Astronautics. doi:10.2514/6.2013-1769
- Xia, K., Harik, R., Herrera, J., Patel, B., & Grimsley, B. (2018). Numerical simulation of AFP nip point temperature prediction for complex geometries. In *SAMPE 2018 Conference & Exhibition*. Long Beach, CA.
- Yi, J.-j., Zeng, T., Rong, J.-h., & Li, Y.-m. (2014). A topology optimization method based on element independent nodal density. *Journal of Central South University*, 21(2), 558–566. doi:10.1007/s11771-014-1974-8
- Zienkiewicz, O. C. & Taylor, R. L. (2002). *The Finite Element Method: The Basis* (5. ed., reprinted). OCLC: 249013082. Oxford: Butterworth-Heinemann.

APPENDIX A

MATERIAL PROPERTIES

The material properties used in this work are summarized in Table A.1. These properties are defined in terms of engineering constants and have been compiled from literature. The material NISO1 is used by Andreassen et al. (2011) to perform topology optimization of an isotropic MBB 2D-beam. Similarly, the material NUND1 is obtained by non-dimensionalizing the engineering constants presented by Setoodeh et al. (2005) for simultaneous optimization of topology and fiber path of 2D bending problems. Moreover, the material NISO2 is obtained by when computing the effective properties of a quasi-isotropic laminate whose material is NUND1. The effective properties are given by

$$E_x = \frac{1}{h} \left(\frac{A_{11}A_{22} - A_{12}^2}{A_{22}} \right), \quad (\text{A.1})$$

and

$$\nu_{xy} = \frac{A_{12}}{A_{22}}. \quad (\text{A.2})$$

Table A.1: Material properties using engineering constants

name	type	values
NISO1	isotropic	$E = 1, \nu = 0.3$
NISO2	isotropic	$E = 0.43, \nu = 0.23$
NUND1	transversely isotropic	$E_1 = 1.0, E_2 = 0.068, \nu_{12} = 0.318,$ $G_{12} = 0.0464, \nu_{23} = 0.3$
NUND2	transversely isotropic	$E_1 = 1.0, E_2 = 0.068, \nu_{12} = 0.3,$ $G_{12} = 0.0464, \nu_{23} = 0.0$

APPENDIX B

NON-DIMENSIONAL TRANSVERSELY ISOTROPIC STIFFNESSES

Based on Nemeth (2011), the linear elastic constitutive equations of a transversely isotropic material can be represented in matrix form as

$$[C_{ijkl}] = \begin{bmatrix} C_{11} & C_{12} & C_{13} & 0 & 0 & 0 \\ C_{12} & C_{11} & C_{13} & 0 & 0 & 0 \\ C_{13} & C_{13} & C_{33} & 0 & 0 & 0 \\ 0 & 0 & 0 & C_{44} & 0 & 0 \\ 0 & 0 & 0 & 0 & C_{55} & 0 \\ 0 & 0 & 0 & 0 & 0 & C_{66} \end{bmatrix}, \quad (\text{B.1})$$

which expressed in terms of engineering constants

$$C_{11} = \frac{E_T}{1 + \nu_{TT}} \frac{1 - \frac{E_T}{E_L} \nu_{LT}^2}{1 - \nu_{TT} - 2 \frac{E_T}{E_L} \nu_{LT}^2}, \quad (\text{B.2})$$

$$C_{12} = \frac{E_T}{1 + \nu_{TT}} \frac{\nu_{TT} + \frac{E_T}{E_L} \nu_{LT}^2}{1 - \nu_{TT} - 2 \frac{E_T}{E_L} \nu_{LT}^2}, \quad (\text{B.3})$$

$$C_{13} = \frac{\nu_{LT} E_T}{1 - \nu_{TT} - 2 \frac{E_T}{E_L} \nu_{LT}^2}, \quad (\text{B.4})$$

$$C_{33} = \frac{E_L (1 - \nu_{TT})}{1 - \nu_{TT} - 2 \frac{E_T}{E_L} \nu_{LT}^2}, \quad (\text{B.5})$$

$$C_{44} = C_{55} = G_{TL} \quad (\text{B.6})$$

$$C_{66} = \frac{E_T}{2(1 + \nu_{TT})}, \quad (\text{B.7})$$

where T denotes the transversal direction and L the longitudinal direction. Factoring E_L from Eqs. (B.2)-(B.7) yields

$$C_{11} = E_L \frac{\frac{E_T}{E_L}}{1 + \nu_{TT}} \frac{1 - \frac{E_T}{E_L} \nu_{LT}^2}{1 - \nu_{TT} - 2 \frac{E_T}{E_L} \nu_{LT}^2}, \quad (\text{B.8})$$

$$C_{12} = E_L \frac{\frac{E_T}{E_L}}{1 + \nu_{TT}} \frac{\nu_{TT} + \frac{E_T}{E_L} \nu_{LT}^2}{1 - \nu_{TT} - 2 \frac{E_T}{E_L} \nu_{LT}^2}, \quad (\text{B.9})$$

$$C_{13} = E_L \frac{\nu_{LT} \frac{E_T}{E_L}}{1 - \nu_{TT} - 2 \frac{E_T}{E_L} \nu_{LT}^2}, \quad (\text{B.10})$$

$$C_{33} = E_L \frac{1 - \nu_{TT}}{1 - \nu_{TT} - 2 \frac{E_T}{E_L} \nu_{LT}^2}, \quad (\text{B.11})$$

$$C_{66} = E_L \frac{\frac{E_T}{E_L}}{2(1 + \nu_{TT})}, \quad (\text{B.12})$$

including the shear stiffnesses

$$C_{44} = E_L \frac{G_{TL}}{E_L}, \quad (\text{B.13})$$

$$C_{55} = E_L \frac{G_{TL}}{E_L}, \quad (\text{B.14})$$

where the stiffnesses are now defined as functions of the non-dimensional set E_T/E_L , ν_{TT} , ν_{LT} , G_{TL}/E_L premultiplied by the dimensional E_L . Quod erat demonstrandum

$$C_{ijkl} = E_L \hat{C}_{ijkl} \quad (\text{B.15})$$

APPENDIX C

LAGRANGE MULTIPLIER COMPUTATION

The Lagrange multiplier is computed by solving the following non-linear system of algebraic equations

$$x^{n+1} = \begin{cases} \max\{(1 - \zeta)x^n, 0\} & \text{if } x^n B^n(\mu^n) \leq \max\{(1 - \zeta)x^n, 0\} \\ \min\{(1 + \zeta)x^n, 1\} & \text{if } \min\{(1 + \zeta)x^n, 1\} \leq x^n B^n(\mu^n) \\ x^n B^n(\mu^n) & \text{otherwise} \end{cases} \quad (\text{C.1})$$

$$\frac{V(x^{n+1})}{V_0} - \eta = 0 \quad (\text{C.2})$$

where the inequality constraint, Eq. (3.36), is assumed to be active, and $V(x^{n+1})$ is approximated with Eq. (3.44). By replacing Eq. (C.1) into Eq. (C.2), the resulting non-linear equation follows the functional implicit form

$$F(V(\mu^n; x^n, \rho^n, p, \beta, \zeta); V_0, \eta) = 0 \quad (\text{C.3})$$

with μ^n being unknown. Note that

$$\lim_{\mu \rightarrow 0} F(\mu) = 1 - \eta, \quad (\text{C.4})$$

while

$$\lim_{\mu \rightarrow \infty} F(\mu) = -\eta. \quad (\text{C.5})$$

This sign changing interval motivates the use of a bracketing method. However to benefit from the speed of open methods while maintaining the reliability of bracketing, Brent (2002) method is used to compute the Lagrange multiplier.

APPENDIX D

IN-PLANE INVARIANT MATRICES

The stiffness tensor transformation equations are given by

$$\bar{C}_{ijkl} = a_{iq}a_{jr}a_{ks}a_{lt}C_{qrst}, \quad (D.1)$$

where the a_{iq} rank-two tensors are orthogonal tensors composed of direction cosines. The rotation matrices are written below

$$[A_\theta] = \begin{bmatrix} \cos \theta & \sin \theta & 0 \\ -\sin \theta & \cos \theta & 0 \\ 0 & 0 & 1 \end{bmatrix}, \quad (D.2)$$

$$[A_\phi] = \begin{bmatrix} \cos \phi & 0 & -\sin \phi \\ 0 & 1 & 0 \\ \sin \phi & 0 & \cos \phi \end{bmatrix}. \quad (D.3)$$

Note the lack of the third Euler angle due to symmetry of the thread. Thus, the general rotation matrix is written as

$$[A] = [A_\phi][A_\theta] = \begin{bmatrix} \cos \theta \cos \phi & \sin \theta \sin \phi & -\sin \phi \\ -\sin \theta & \cos \theta & 0 \\ \cos \theta \sin \phi & \sin \theta \sin \phi & \cos \phi \end{bmatrix}. \quad (D.4)$$

Based on Ting (1987) the general stiffnesses can be transformed into a general axes system by the following transformation law

$$[\bar{C}] = [Q][C][Q]^T, \quad (D.5)$$

where the transformation matrix $[Q]$ is a quadratic transform which can be written in block matrix form as

$$[Q] = \begin{bmatrix} [K] & 2[M] \\ [N] & [L] \end{bmatrix}. \quad (\text{D.6})$$

Each block matrix is given by the following indexed expression:

$$k_{ij} = a_{ij}^2, \quad (\text{D.7})$$

$$m_{ij} = a_{ik}a_{ip} \quad j \neq k \neq p, \quad (\text{D.8})$$

$$n_{ij} = a_{rj}a_{sj} \quad i \neq r \neq s, \quad (\text{D.9})$$

$$l_{ij} = a_{rk}a_{sp} + a_{rp}a_{sk} \quad j \neq k \neq p \neq i \neq r \neq s, \quad (\text{D.10})$$

where the repeated index does not imply summation. If the rotation θ is only about the x_3 -axis (e.g, $\phi = \pi/2$), the transformation matrix simplifies to

$$[Q] = \begin{bmatrix} m^2 & n^2 & 0 & 0 & 0 & 2mn \\ n^2 & m^2 & 0 & 0 & 0 & -2mn \\ 0 & 0 & 1 & 0 & 0 & 0 \\ 0 & 0 & 0 & m & n & 0 \\ 0 & 0 & 0 & -n & m & 0 \\ mn & -mn & 0 & 0 & 0 & m^2 - n^2 \end{bmatrix} \quad (\text{D.11})$$

where

$$m = \cos \theta, \quad n = \sin \theta. \quad (\text{D.12})$$

Using the double angle trigonometric functions, the simplified transformation matrix can be expanded to

$$[Q] = [Q_0] + [Q_1] \cos \theta + [Q_2] \sin \theta + [Q_3] \cos 2\theta + [Q_4] \sin 2\theta, \quad (\text{D.13})$$

where

$$[Q_0] = \begin{bmatrix} 1/2 & 1/2 & 0 & 0 & 0 & 0 \\ 1/2 & 1/2 & 0 & 0 & 0 & 0 \\ 0 & 0 & 1 & 0 & 0 & 0 \\ 0 & 0 & 0 & 0 & 0 & 0 \\ 0 & 0 & 0 & 0 & 0 & 0 \\ 0 & 0 & 0 & 0 & 0 & 0 \end{bmatrix}, \quad (D.14)$$

$$[Q_1] = \begin{bmatrix} 0 & 0 & 0 & 0 & 0 & 0 \\ 0 & 0 & 0 & 0 & 0 & 0 \\ 0 & 0 & 0 & 0 & 0 & 0 \\ 0 & 0 & 0 & 1 & 0 & 0 \\ 0 & 0 & 0 & 0 & 1 & 0 \\ 0 & 0 & 0 & 0 & 0 & 0 \end{bmatrix}, \quad (D.15)$$

$$[Q_2] = \begin{bmatrix} 0 & 0 & 0 & 0 & 0 & 0 \\ 0 & 0 & 0 & 0 & 0 & 0 \\ 0 & 0 & 0 & 0 & 0 & 0 \\ 0 & 0 & 0 & 0 & 1 & 0 \\ 0 & 0 & 0 & -1 & 0 & 0 \\ 0 & 0 & 0 & 0 & 0 & 0 \end{bmatrix}, \quad (D.16)$$

$$[Q_3] = \begin{bmatrix} 1/2 & -1/2 & 0 & 0 & 0 & 0 \\ -1/2 & 1/2 & 0 & 0 & 0 & 0 \\ 0 & 0 & 0 & 0 & 0 & 0 \\ 0 & 0 & 0 & 0 & 0 & 0 \\ 0 & 0 & 0 & 0 & 0 & 0 \\ 0 & 0 & 0 & 0 & 0 & 1 \end{bmatrix}, \quad (\text{D.17})$$

$$[Q_4] = \begin{bmatrix} 0 & 0 & 0 & 0 & 0 & 1 \\ 0 & 0 & 0 & 0 & 0 & -1 \\ 0 & 0 & 0 & 0 & 0 & 0 \\ 0 & 0 & 0 & 0 & 0 & 0 \\ 0 & 0 & 0 & 0 & 0 & 0 \\ 1/2 & -1/2 & 0 & 0 & 0 & 0 \end{bmatrix}. \quad (\text{D.18})$$

Thus, a stiffness tensor transformation around $x_1 = 0$ can also be expanded to

$$[Q][C][Q]^T = \left([Q_0] + \sum_{i=1}^4 [Q_i]v_i \right) [C] \left([Q_0]^T + \sum_{i=1}^4 [Q_i]^T v_i \right), \quad (\text{D.19})$$

which under the special case of $C_{46} = C_{56} = C_{14} = C_{24} = C_{15} = C_{25} = C_{35} = 0$, the transformation simplifies to

$$[Q][C][Q]^T = [\Gamma_0] + [\Gamma_1] \cos 2\theta + [\Gamma_2] \sin 2\theta + [\Gamma_3] \cos 4\theta + [\Gamma_4] \sin 4\theta, \quad (\text{D.20})$$

where $[\Gamma_i]$ are called *material invariant matrices*.

$$[\Gamma_0] = \begin{bmatrix} U_1 & U_4 & \frac{C_{13} + C_{23}}{2} & 0 & 0 & \frac{C_{16} - C_{26}}{2} \\ U_4 & U_1 & \frac{C_{13} + C_{23}}{2} & 0 & 0 & -\frac{C_{16} - C_{26}}{2} \\ \frac{C_{13} + C_{23}}{2} & \frac{C_{13} + C_{23}}{2} & C_{33} & 0 & 0 & 0 \\ 0 & 0 & 0 & \frac{C_{44} + C_{55}}{2} & 0 & 0 \\ 0 & 0 & 0 & 0 & \frac{C_{44} + C_{55}}{2} & 0 \\ \frac{C_{16} - C_{26}}{2} & -\frac{C_{16} - C_{26}}{2} & 0 & 0 & 0 & U_5 \end{bmatrix}, \quad (D.21)$$

$$[\Gamma_1] = \begin{bmatrix} U_2 & U_2 & \frac{C_{13} - C_{23}}{2} & 0 & 0 & 0 \\ -U_2 & -U_2 & -\frac{C_{13} - C_{23}}{2} & 0 & 0 & 0 \\ 0 & 0 & 0 & 0 & 0 & 0 \\ 0 & 0 & 0 & \frac{C_{44} - C_{55}}{2} & C_{45} & 0 \\ 0 & 0 & 0 & C_{45} & -\frac{C_{44} - C_{55}}{2} & 0 \\ \frac{C_{16} + C_{26}}{2} & \frac{C_{16} + C_{26}}{2} & C_{36} & 0 & 0 & 0 \end{bmatrix}, \quad (D.22)$$

$$[\Gamma_2] = \begin{bmatrix} \frac{C_{16} + C_{26}}{2} & \frac{C_{16} + C_{26}}{2} & C_{36} & 0 & 0 & 0 \\ -\frac{C_{16} + C_{26}}{2} & -\frac{C_{16} + C_{26}}{2} & -C_{36} & 0 & 0 & 0 \\ 0 & 0 & 0 & 0 & 0 & 0 \\ 0 & 0 & 0 & C_{45} & -\frac{C_{44} - C_{55}}{2} & 0 \\ 0 & 0 & 0 & 0 & -\frac{C_{44} - C_{55}}{2} & -C_{45} \\ U_2/2 & U_2/2 & \frac{C_{13} - C_{23}}{2} & 0 & 0 & 0 \end{bmatrix}, \quad (D.23)$$

$$[\Gamma_3] = \begin{bmatrix} U_3 & -U_3 & 0 & 0 & 0 & 0 \\ -U_3 & U_3 & 0 & 0 & 0 & 0 \\ 0 & 0 & 0 & 0 & 0 & 0 \\ 0 & 0 & 0 & 0 & 0 & 0 \\ 0 & 0 & 0 & 0 & 0 & 0 \\ 0 & 0 & 0 & 0 & 0 & -U_3 \end{bmatrix}, \quad (\text{D.24})$$

$$[\Gamma_4] = \begin{bmatrix} \frac{C_{16} - C_{26}}{2} & -\frac{C_{16} - C_{26}}{2} & 0 & 0 & 0 & U_3 \\ -\frac{C_{16} - C_{26}}{2} & \frac{C_{16} - C_{26}}{2} & 0 & 0 & 0 & -U_3 \\ 0 & 0 & 0 & 0 & 0 & 0 \\ 0 & 0 & 0 & 0 & 0 & 0 \\ 0 & 0 & 0 & 0 & 0 & 0 \\ U_3 & -U_3 & 0 & 0 & 0 & \frac{C_{16} - C_{26}}{2} \end{bmatrix}, \quad (\text{D.25})$$

where

$$U_1 = (3C_{11} + 3C_{22} + 2C_{12} + 4C_{16})/8, \quad (\text{D.26})$$

$$U_2 = (C_{11} - C_{22})/2, \quad (\text{D.27})$$

$$U_3 = (C_{11} + C_{22} - 2C_{12} - 4C_{66})/8, \quad (\text{D.28})$$

$$U_4 = (C_{11} + C_{22} + 6C_{12} - 4C_{66})/8, \quad (\text{D.29})$$

$$U_5 = (C_{11} + C_{22} - 2C_{12} + 4C_{66})/8. \quad (\text{D.30})$$